THESIS FOR THE DEGREE OF DOCTOR OF PHILOSOPHY

Understanding Cellulose Across Length Scales: A Multiscale Perspective on Chemistry, Structure, and Surface Chemistry

Nivedhitha Venkatraman

Department of Chemistry and Chemical Engineering
CHALMERS UNIVERSITY OF TECHNOLOGY

Gothenburg, Sweden 2026

Understanding Cellulose Across Length Scales: A Multiscale Perspective on Chemistry, Structure, and Surface Chemistry

NIVEDHITHA VENKATRAMAN

ISBN: 978-91-8103-509-4

Acknowledgments, dedications and similar personal statements in this thesis reflect the author's own views.

© NIVEDHITHA VENKATRAMAN, 2026

Doktorsavhandlingar vid Chalmers tekniska högskola
Ny serie nr 5966
ISSN 0346-718X
DOI: https://doi.org/10.63959/chalmers.dt/5966

Department of Chemistry and Chemical Engineering
Chalmers University of Technology
SE-412 96 Gothenburg
Sweden
Phone: +46(0)31 772 1000

Cover page showing the multiscale analytical framework of the thesis, designed by Nivedhitha Venkatraman, linking fiber morphology and swelling behavior, nanoscale organization, and surface chemical fingerprints through light microscopy, SAXS/WAXS, ToF-SIMS, and chemometric analysis.

Printed by Chalmers Digitaltryck
Gothenburg, Sweden 2026

Understanding Cellulose Across Length Scales:
A Multiscale Perspective on Chemistry, Structure, and Surface Chemistry

NIVEDHITHA VENKATRAMAN

Department of Chemistry and Chemical Engineering

Chalmers University of Technology

Abstract

This thesis addresses the question: how do chemical modification, drying history, pulp processing and thermal treatments reorganize cellulose fibers across length scales, from micrometer-scale fiber morphology and nanometer-scale fibrillar arrangement to the molecular composition of the fiber surface? To answer this, dialcohol cellulose (DALC) fibers with different degrees of modification serve as a model system for relating chemical modification to fiber wall structure and swelling, while Kraft handsheets and hot-pressed chemi-thermomechanical pulp (CTMP) sheets are used to study how processing changes the surface chemistry of industrially relevant fiber materials.

At the fiber wall scale, increasing DALC shifts the swelling behavior from mild bulging to pronounced balloon-collar morphology and, at the highest modification level to a coexistence of balloon-collar and uniformly swollen fibers. Small- and wide-angle X-ray scattering (SAXS/WAXS) shows that modification reduces crystalline order and increases the SAXS-derived characteristic length, an apparent length scale of the fibrillar arrangement in the fiber wall. This length depends on drying history: it is largest in never-dried fibers, decreases on drying, and is only partially restored upon rewetting. In never-dried fibers, the characteristic length increases together with the water retention value, indicating that macroscopic swelling capacity is related to the nanoscale arrangement of the fiber wall.

Having linked bulk chemistry to internal structure, the thesis then moves to the fiber surface, the interface that governs how these materials ultimately perform. A ToF-SIMS and multivariate workflow was developed to separate lignin- and polysaccharide-associated ions in softwood Kraft handsheets. Marker ions were first identified on compacted reference materials of cellulose, hemicelluloses and lignin, and were retained only if they were reproducible across replicate spectra and not dominated by contaminants, adducts or overlapping peaks, a conservative approach that minimizes false-positive assignments. Applied to bleached and unbleached handsheets, the selected ions captured the lignin removal caused by bleaching. Matrix effects make these comparisons semi-quantitative. Extending this workflow to industrially hot-pressed CTMP papers showed that temperature changes which components dominate the roll-contact surface: sterol- and fatty-acid-salt ions at 100 °C, and lignin-related and long-chain fatty-acid ions at 200 °C, consistent with temperature-driven redistribution of existing components. Together, these results deliver the thesis's central message: surface composition is not a passive reflection of bulk chemistry, but an actively reorganized, processing-dependent property.

Keywords

Dialcohol cellulose (DALC), degree of modification (DOM), fiber wall swelling, drying history, hornification, SAXS/WAXS, ToF-SIMS, chemometrics (PCA/OPLS-DA/SUS), hot-press, CTMP, softwood Kraft fibers

List of Publications and Presentations

This thesis is based on the following appended publications and manuscript:

I. **IMPACT OF DIALCOHOL CELLULOSE MODIFICATION ON THE STRUCTURAL MORPHOLOGY AND SWELLING BEHAVIOUR OF CELLULOSE FIBRES**
Nivedhitha Venkatraman, Katarina Jonasson, Giada Lo Re, Per A. Larsson, Anette Larsson
Cellulose (2025) 32:8101–8117

II. **MULTISCALE STRUCTURAL EVOLUTION IN DIALCOHOL CELLULOSE FIBERS: EFFECTS OF MODIFICATION AND DRYING HISTORY STUDIED BY SMALL- AND WIDE-ANGLE X-RAY SCATTERING TECHNIQUES**
Nivedhitha Venkatraman, Åsa Jerlhagen, Johanna Sjölund, Hampus Karlsson, Katarina Jonasson, Michal Strach, Giada Lo Re, Eva Malmström, Lars Evenäs, Per A. Larsson, Anette Larsson
To be submitted in Carbohydrate Polymers.

III. **SURFACE PROFILING OF CELLULOSE, HEMICELLULOSE, AND LIGNIN IN SOFTWOOD KRAFT HANDSHEETS BY REFERENCE-GUIDED TOF-SIMS**
Nivedhitha Venkatraman, Per A. Larsson, Anette Larsson, Per Malmberg
Carbohydrate Polymer Technologies and Applications 15 (2026) 101209

IV. **TEMPERATURE-DRIVEN SURFACE REORGANIZATION IN HOT-PRESSED CTMP SHEETS REVEALED BY TOF-SIMS AND CHEMOMETRICS**
Nivedhitha Venkatraman, Jutima Leksuntrakorn, Anders Brolin, Per Malmberg, Anette Larsson
Polymer Testing 161 (2026) 109301

Papers I, III and IV are published open access under a CC BY 4.0 license. Figures adapted from these papers are reproduced under the terms of that license.

Contribution Report

The author of this thesis has made the following contributions to the publications included:

Paper I: Main author. Developed the concept and experimental design in collaboration with supervisors. Performed most of the experimental work, excluding the chemical modification of fibers and titration. Wrote the first draft of the paper. Revised the paper in collaboration with co-authors.

Paper II: Main author. Developed the concept and experimental design in collaboration with all co-authors. Performed most of the experimental work, except for the molecular weight analysis and the dynamic nuclear polarization nuclear magnetic resonance characterization. Analyzed and interpreted results in collaboration with supervisors. Wrote the first draft of the paper. Revised the paper in collaboration with all co-authors.

Paper III: Main author. Developed the concept and experimental design in collaboration with supervisors. Prepared the compacted reference surfaces and performed all ToF-SIMS measurements, data processing and chemometric analysis. The handsheets and the softwood Kraft pulp lignin were provided by Åke Henrik-Klemens. Wrote the first draft of the paper. Revised the paper in collaboration with co-authors.

Paper IV: Main author. Developed the concept and chemometric work. Performed all the analysis except the experimental data acquisition. Wrote the first draft of the paper. Revised the paper in collaboration with co-authors.

Use of generative AI

Generative AI tools were used in the preparation of this thesis. ChatGPT (OpenAI) was used to create illustrative elements in **Figure 2.4.1- 2.4.3**, as stated in the figure captions. ChatGPT (OpenAI) and Claude (Anthropic) were used for language editing and to improve the clarity of the text. All research data were generated and analyzed by the author and co-authors; AI tools were not used to produce or process data. The author reviewed and edited all AI-assisted content and takes full responsibility for the content of this thesis.

Acknowledgments

This research was funded by the Bo Rydin Foundation and supported by Fiber – Design for circularity – Lignocellulose-based thermoplastics, a VINNOVA Competence Center. The first half of my PhD was carried out within the industrial graduate school Resource Smart Processes, funded by the strategic innovation program BioInnovation—a joint initiative of Vinnova, Formas, and the Swedish Energy Agency. I am deeply grateful for this support and for the research environments that made it possible to pursue this work with both scientific ambition and long-term continuity.

I would like to express my sincere gratitude to my supervisors Per Malmberg and Anette Larsson for their steady support, scientific guidance, and the many thoughtful discussions that helped shape this work. Their confidence in me, especially during the moments when the work felt complex or uncertain, made a genuine difference. I also thank my co-supervisor Per Larsson for sharing his expertise so generously and for strengthening this endeavor with clear scientific judgment, practical insight, and calm encouragement when it mattered most.

I would also like to thank Anna Ström (my manager), Christian Müller (my examiner), and the administrative team (Emma Andersson, Lotta Pettersson, and Anna Oskarsson), and all the staff scientists for their help and support throughout my doctoral studies, and for ensuring that the practical and administrative aspects ran smoothly. That support, often behind the scenes, is invaluable in enabling research to move forward.

I gratefully acknowledge Essity, SCA, AstraZeneca, Södra, and SciLifeLab for their support and collaboration, and for offering perspectives that strengthened the relevance and direction of this research. I also gratefully acknowledge Tetra Pak for the industrial supervision and for consistently bringing an application-relevant viewpoint that kept the research grounded in real-world challenges. I am thankful to my collaborators and co-authors for their contributions, stimulating discussions, and the shared commitment to doing careful, high-quality science.

My sincere thanks extend to Dr Elias Ranbari, Dr Katarina Logg, Dr Michal Strach (CMAL, Department of Physics), and Dr Shuichi Haraguchi and Dr Mats Hulander (Chemistry, Chalmers) for their guidance, generosity, and support in the

laboratory. I also acknowledge the Department of Chemistry and Chemical Engineering, for providing me with the infrastructure and the best research environment that enabled this work to be carried out with rigor and consistency.

On a personal level, it has been a real privilege to be surrounded by such wonderful colleagues: Caroline Lööf, Dr Aoife Clancy, Arvindh Seshadri, Luigi Galluccio, Giovanni Tizzanini, Dr Ratchawit Janewithayapun, Dr Jakob Ytterberg, Dr Ye Zar Ni Htwe, Dr Aloisia Elaine King, Dr Liam Mistry, Amina Shaji, Nasim Arabjazi, Savitha Srinivasan, Dr Åke Henrik-Klemens, Dr Roujin Ghaffari and Dr Robin Ström, as well as everyone else who has been part of this chapter of my life. Thank you for the warmth, laughter, encouragement, and everyday conversations that made the long days lighter and the demanding periods more manageable. I also thank all my colleagues, friends, and extended family who have been part of this journey for their continued support and encouragement throughout this work, and for the kindness that carried me through more than I can easily put into words. A special thanks to my lunch group: Dennis Raphael Winter, Dr Vinoth Edal Joseph Sundar Rajan, Dr Radhika Nambannor Kunnath and Dr Sriram KK—for the small daily moments of community that mattered more than you may realize.

I am especially grateful to Dr Sriram, my best friend, husband, the father of our son, my badminton mate and personal nutritionist: thank you for your constant moral support, your steady belief in me, and the quiet strength you brought to our everyday life throughout this journey. Finally, and most importantly, I thank my child, Ashwath, for making me a mother and for being my daily reminder of what truly matters. It is difficult to know whether I have taught enough about understanding the world, or whether I have learned more in return, but the latter feels undeniably true. This work would not have happened without that quiet, steadfast support.

Abbreviations

Abbreviation	Definition
BD	Bench-dried
BDDJ	Britt Dynamic Drainage Jar
BSK	Bleached softwood Kraft
CLSM	Confocal laser scanning microscopy
CTMP	Chemi-thermomechanical pulp
CV-ANOVA	Cross-validated analysis of variance
DALC	Dialcohol cellulose
DIC	Differential interference contrast
DOM	Degree of modification
ESAXS	Extremely small-angle X-ray scattering
EWAXS	Extended wide-angle X-ray scattering
FITC	Fluorescein isothiocyanate
FWHM	Full width at half maximum
GGM	Galactoglucomannan
HWFM	Half width full maxima
MAXS	Medium-angle X-ray scattering
MCC	Microcrystalline cellulose
MCP	Microchannel plate detector
ND	Never-dried
OPLS-DA	Orthogonal projections to latent structures discriminant analysis
PCA	Principal component analysis
PC1	Principal component 1
PDMS	Polydimethylsiloxane
RQ	Research question
RW	Rewetted
SAXS	Small-angle X-ray scattering
SKPL	Softwood Kraft pulp lignin
SUS	Shared and unique structures
TIC	Total ion count
TMP	Thermo mechanical pulp
ToF-SIMS	Time-of-flight secondary ion mass spectrometry
USK	Unbleached softwood Kraft
VIP	Variable importance in projection
WAXS	Wide-angle X-ray scattering
WRV	Water retention value

Sample identifiers in this thesis follow the nomenclature defined in **3.8 Sample nomenclature.**

Contents

List of Publications and Presentations ---------- III
Contribution Report ---------- V
Abbreviations ---------- IX
Contents ---------- X
1 Introduction ---------- 1
1.1 Central problem and knowledge gap ---------- 2
1.2 Primary research question ---------- 2
1.3 Secondary research questions ---------- 3
1.3.1 Modification-driven fiber morphology: 3
1.3.2 Modification-dependent nanostructure and swelling response: 3
1.3.3 Surface-chemical fingerprints in fiber-sheet systems: 3
1.3.4 Process-driven surface reorganization in fiber-sheet systems: 3
2 Background ---------- 5
2.1 Materials and Chemistry ---------- 5
2.1.1 Lignocellulosic fiber materials as hierarchical systems 5
2.1.2 Chemical composition and hierarchical structure of cellulose-rich softwood fibers 5
2.1.3 DALC cellulose as a targeted chemical modification platform..... 7
2.2 Structure and drying response ---------- 8
2.2.1 Water accessibility, swelling, and drying history in cellulose fiber walls 8
2.2.2 Nanoscale organization as a determinant of fiber wall swelling 8
2.3 Fiber surface composition ---------- 9
2.3.1 Fiber-network surfaces and interfacial function 9
2.3.2 Surface-sensitive chemical characterization of lignocellulosic materials 9
2.3.3 Surface treatment-induced reorganization in fiber sheets 10
2.4 Analytical framework for multiscale study ---------- 11

2.4.1 Optical microscopy 11
2.4.2 Small- and wide-angle X-ray scattering 13
2.4.3 Time-of-flight secondary ion mass spectrometry 15
2.4.4 Chemometric analysis of complex ToF-SIMS datasets 18
3 Materials and Methods ----- 21
3.1 Materials ----- 21
3.1.1 Reference polysaccharides and lignin 21
3.1.2 Kraft pulps for handsheets 21
3.1.3 CTMP paper 21
3.2 Sample preparation ----- 22
3.2.1 Fibers for DALC modification 22
3.2.2 Preparation of bench-dried and rewetted fibers 22
3.2.3 Kraft handsheet preparation 22
3.2.4 Preparation of compacted reference surfaces 22
3.2.5 CTMP paper hot-pressing samples and sampling 23
3.3 Gravimetric determination of fines ----- 23
3.4 Water retention value ----- 23
3.5 Light microscopy ----- 23
3.5.1 Optical microscopy and image analysis 23
3.5.2 Confocal laser scanning microscopy 24
3.6 X-ray scattering ----- 24
3.6.1 Determination of crystallinity index and crystal domain width from WAXS data 25
3.6.2 SAXS data analysis 26
3.7 ToF-SIMS surface analysis and chemometrics ----- 28
3.7.1 Instrument configuration 28
3.7.2 Charge compensation and acquisition control 29
3.7.3 Mass calibration and peak definition 29

3.7.4 Normalization and preprocessing 29
3.7.5 Chemometric workflow 30
3.7.6 Quality control strategy 30
3.8 Sample nomenclature ----- 30
4 Results and Discussion ----- 33
4.1 Morphological evolution of DALC fibers with increasing DOM ----- 33
4.1.1 Optical microscopy reveals DOM-dependent heterogeneous swelling 33
4.1.2 Balloon-collar morphology and transition toward uniform swelling 35
4.1.3 Lumen accessibility and internal water distribution from CLSM dual-labeling 37
4.1.4 Quantification of swelling by WRV and fiber width distributions ... 39
4.1.5 Effect of drying/rewetting: morphological 'memory' and inelastic deformation 40
4.1.6 Answer to RQ1 40
4.2 X-ray scattering: Ångström-to-nanometer structural response ----- 41
4.2.1 WAXS: Increasing DOM reduces crystallinity and apparent crystallite width 41
4.2.2 Model-independent Kratky analysis of characteristic nanoscale correlations 44
4.2.3 Peak fitting of SAXS data: Model-based approach 46
4.2.4 Linking WRV to nanoscale descriptors across modification levels and drying histories 50
4.2.5 Answer to RQ2 51
4.3 ToF-SIMS surface fingerprinting of Kraft fiber handsheets ----- 52
4.3.1 Workflow overview: compacted reference surfaces and pairwise PCA rationale 52
4.3.2 Reference vs handsheet spectra: effects of surface topography and achievable mass resolution 54

4.3.3 Interferences and matrix effects: contaminants, salt/adduct contributions, and conservative peak screening 55

4.3.4 Semi-quantitative comparison of bleached vs unbleached handsheets using validated marker ions 57

4.3.5 Spatial mapping by 2D ToF-SIMS: heterogeneity and marker-ion localization..... 59

4.3.6 Answer to RQ3 61

4.4 Surface reorganization of CTMP paper during hot-pressing ---------- 62

4.4.1 Dataset overview and modeling logic: separating temperature effects from front/back-side asymmetry..... 62

4.4.2 SUS-plot selection of temperature-specific marker ions independent of side effects (selection criteria and interpretation)..... 64

4.4.3 Semi-quantitative validation of temperature-responsive ions 66

4.4.4 Interpretation and implications: extractives/lignin mobility, fatty-acid salt enrichment, and process-relevant surface tuning..... 67

4.4.5 Answer to RQ4 68

5 Conclusion---------- 69

6 Scientific Reflections: Beyond the Thesis---------- 71

7 Bibliography---------- 75

1 Introduction

Lignocellulosic materials occupy a distinctive position among renewable material systems because they combine plant origin, structural hierarchy, and broad relevance, from paper production to biofuels and biomaterials [1-3]. Derived from plant cell walls, they are built from cellulose, hemicelluloses, and lignin arranged in a multiscale composite architecture in which chemical composition and structural organization act together to govern material behavior [3-5]. Their performance is therefore determined not only by polymer composition, but also by the spatial distribution of cellulose, hemicelluloses, and lignin, the interactions between these components, and fibrillar arrangements within the fiber wall [6-11]. Their structural hierarchy and chemical complexity make lignocellulosic materials particularly well suited for addressing how targeted chemical modifications are translated into structural reorganization, altered moisture response, and enrichment or depletion of specific chemical species at the fiber surface relative to the bulk.

Within this broader material class, cellulose is of particular interest because it forms the principal structural backbone of the plant cell wall and carries a high density of hydroxyl groups, of which those located at fibril surfaces and in less ordered regions are available for chemical reaction [12-14]. This combination of structural hierarchy and chemical accessibility makes cellulose well suited for modification. Fiber chemistry can be altered by targeted reactions at accessible hydroxyl groups, for example by periodate oxidation followed by reduction, with the degree of conversion adjusted through reaction conditions [15]. The resulting consequences for swelling, nanoscale organization, and interfacial composition can then be interpreted in the context of the fiber wall's hierarchical structure [12, 16]. Handsheets provide this next level of organization by translating fiber- and fiber wall-level characteristics into an assembled network that can be examined under controlled conditions.

This thesis comprises four studies on two material groups. In Papers I–II, dialcohol cellulose (DALC), a chemically modified cellulose, is characterized in terms of fiber morphology, swelling, and nanoscale structure. In Papers III–IV, unmodified Kraft and chemi-thermomechanical pulp (CTMP) handsheets are examined by ToF-SIMS and chemometrics, addressing surface chemistry in Kraft and temperature-driven

reorganization during hot-pressing in CTMP. Together, these studies link chemistry, structure, and surface behavior within a multiscale materials framework.

1.1 Central problem and knowledge gap

Cellulose-based fibers are central to the development of renewable materials, and their performance is governed by the interplay between chemical functionality, hierarchical structure, and surface composition. Chemical modification, pulping processes (Kraft or chemi-thermomechanical pulp, CTMP), and thermal treatment (hot-pressing) alter fiber wall organization and surface composition. In this thesis, these changes are examined across multiple length scales by combining light microscopy, small- and wide-angle X-ray scattering (SAXS/WAXS), and time-of-flight secondary ion mass spectrometry (ToF-SIMS) coupled with chemometrics. A multiscale approach is required because no single technique can simultaneously resolve fiber-level swelling changes, nanoscale fiber wall organization, and surface-chemical fingerprints on heterogeneous fibers. The integrated approach links chemistry-driven changes within the fiber wall to nanostructural evolution, macroscopic swelling, and surface chemical expression in paper-based systems subjected to thermo-mechanical processing.

1.2 Primary research question

How do chemical modification, drying history, pulp processing and thermal treatments reorganize cellulose fibers across length scales, from micrometer-scale fiber morphology and nanometer-scale fibrillar arrangement to the molecular composition of the fiber surface?

To address this primary research question, the thesis is structured around four secondary research questions that follow the material response across increasing length scales: from fiber wall swelling and morphology, to nanoscale fiber wall arrangement and its link to swelling, to surface-chemical fingerprints in fiber-sheet systems, and finally to processing-driven surface reorganization under thermo-mechanical treatment.

1.3 Secondary research questions

1.3.1 Modification-driven fiber morphology:

RQ1: How does increasing DALC modification affect fiber wall swelling, morphology, and water retention?

1.3.2 Modification-dependent nanostructure and swelling response:

RQ2: How do DALC modification and drying history alter nanoscale fiber wall arrangement, and how do these relate to macroscopic swelling?

1.3.3 Surface-chemical fingerprints in fiber-sheet systems:

RQ3: Can a reference-guided ToF-SIMS and chemometrics workflow distinguish lignin-associated from polysaccharide-associated surface-ion patterns in chemically and topographically complex handsheets?

1.3.4 Process-driven surface reorganization in fiber-sheet systems:

RQ4: How does hot-pressing temperature reshape the surface chemistry of papers, and can ToF-SIMS with supervised chemometrics resolve temperature-specific marker ions?

2 Background

2.1 Materials and Chemistry

2.1.1 Lignocellulosic fiber materials as hierarchical systems

Lignocellulosic materials are renewable structural systems in which chemical composition and hierarchical organization are inseparable [17, 18]. Their behavior is governed not only by the presence of cellulose, hemicelluloses, and lignin, but also by the distribution and spatial organization of these polymers across the fiber wall and fiber networks [17-19]. Mechanical response, moisture sensitivity, and interfacial behavior are governed by the interplay between chemistry and structure across several length scales [20-23].

This multiscale property is important when lignocellulosic materials are chemically modified or subjected to industrial processing. In such cases, a local molecular change may alter intermolecular interactions, reorganize the internal structure of the fiber wall, and alter water accessibility. [21, 24-28]. For cellulose-based materials, these linked responses are important because they influence both bulk properties and interfacial interactions, including fiber–fiber bonding, coating interactions, and contact with heated surfaces during processing and use [21, 24-26]. This thesis elucidates this perspective by following the consequences of modification and processing from the fiber wall to the fiber-network surface.

2.1.2 Chemical composition and hierarchical structure of cellulose-rich softwood fibers

The fiber walls in wood comprise several layers whose thicknesses vary with growth conditions, depending on whether the fiber originates from earlywood or latewood. Cell type, fiber geometry, and wall thickness also differ between softwood and hardwood. This thesis focuses on Scandinavian softwood fibers, which consist primarily of tracheids and are typically about 2–4 mm in length and 20–40 µm in width before pulping-related collapse and deformation [18, 29, 30].

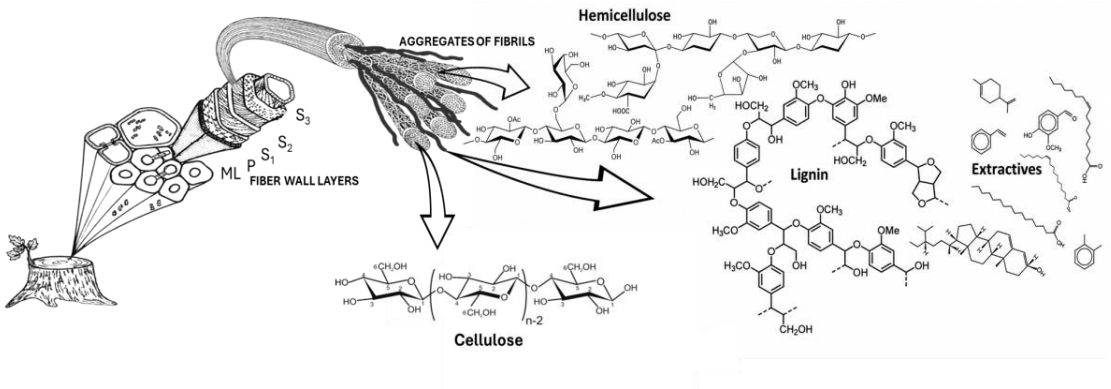


Figure 2.1.1: *Schematic representation of the hierarchical structure of softwood fibers, showing the organization from wood tissue and fiber wall layers to fibril aggregates, together with representative structures of the main chemical constituents: cellulose, hemicelluloses, lignin, and extractives. Credit: The tree-to-fiber-wall schematic is adapted from ref.* [31] *with permission. Copyright © 1989 American Chemical Society. The fibril-aggregate schematic is adapted from ref.* [32] *with permission from the Royal Society of Chemistry.*

The fiber wall consists of the primary wall and the three secondary wall layers S1, S2, and S3 (**Figure 2.1.1**). The primary wall is very thin, approximately 0.1 µm, and contains a comparatively disordered fibrillar arrangement. The S1 layer is typically about 0.2–0.3 µm thick, the S2 layer about 1–5 µm depending on whether the fiber originates from earlywood or latewood, and the S3 layer about 0.1 µm [18, 29, 33, 34]. These layers also differ in fibrillar orientation relative to the fiber axis: the S1 layer commonly shows angles of about 50–70°, the S2 layer about 5–30°, and the S3 layer about 50–90°. Because the S2 layer accounts for most of the wall thickness, it is the dominant structural layer and contributes most strongly to fiber mechanics, moisture-induced deformation, and wall swelling [34].

These wall layers are built from cellulose nanofibrils, which are embedded in a matrix of hemicelluloses and lignin and are arranged helically around the fiber axis as either S-helices (counterclockwise) or Z-helices (clockwise) [18, 29, 30]. Within the wall, the nanofibrils are further associated into larger fibrillar aggregates or bundles rather than existing only as isolated 3–5 nm units [35-37]. These bundles are typically discussed as being on the order of 10–20 nm across, although the reported size depends on the raw material, pulping procedure, drying history, analytical method, and structural definition used. The definition may or may not

include hemicellulose chains associated with the nanofibril aggregates [35, 38, 39]. The fiber wall should therefore not be regarded as a homogeneous cellulose phase, but rather as a layered and hierarchically organized assembly of fibrils and fibril aggregates embedded within the broader lignocellulosic matrix [18, 19]. As a result of this structural complexity, water, reagents, and other small molecules interact with a spatially constrained wall architecture rather than with an isotropic polymer solid. At the molecular level, these fibrils are built from linear cellulose chains composed of repeating anhydroglucose units linked by β-(1→4)-glycosidic bonds [40-42].

2.1.3 DALC cellulose as a targeted chemical modification platform

A modified cellulose material studied in this thesis is DALC, which is obtained by periodate oxidation of cellulose followed by borohydride reduction. Periodate cleaves the bond between C2 and C3 of the anhydroglucose unit and opens the ring, first forming dialdehyde intermediates (here with sodium metaperiodate, $NaIO_4$). Subsequent reduction with sodium borohydride converts these aldehyde groups into ring-opened dialcohol units [43-47]. The modification is partial, and the fibers keep their overall fibrous form under the conditions used; nevertheless, the fiber wall morphology and swelling response change markedly with increasing degree of modification [48-50].

Earlier studies on DALC have shown that partial modification can increase ductility [51, 52], hygroscopicity [53, 54], and thermo-mechanical processability relative to unmodified cellulose-rich fibers [55-61]. At the same time, the modification is not simply a chemical substitution superimposed on an otherwise unchanged substrate. DALC offers a systematic way to examine how altered cellulose chemistry affects intermolecular organization and fiber wall swelling [48] **(Papers I and II)**. The surface-chemical consequences of pulp processing and thermal treatments are addressed later in this thesis, in unmodified Kraft and CTMP fiber sheets [62, 63] **(Papers III and IV)**.

2.2 Structure and drying response

2.2.1 Water accessibility, swelling, and drying history in cellulose fiber walls

When cellulose-rich fibers are exposed to water, water penetrates accessible regions of the wall and interacts with hydroxyl-containing polysaccharides [18, 21]. Swelling can be described as a balance between contributions that drive it and contributions that oppose it [21, 64]. The driving contribution is the osmotic pressure arising from the mixing of water and polymer, hydration and, for charged fibers, counterions [64-66]. The opposing contribution is the elastic restraint of the fibrillar network, which depends on the packing of the fibrils, the proportion of ordered and less ordered regions [19, 64], and the layered structure of the wall [67]. The net swelling therefore depends on how much water can enter the wall, how strongly it is held, and how readily the network can deform. Swelling is thus a hierarchical response that reflects both chemistry and structure [21, 67].

In DALC fibers, ring opening cleaves the C2–C3 bond of the anhydroglucose unit. Such ring-opened units cannot adopt the ring conformation required for packing into the cellulose crystal lattice, and they are therefore expected to perturb ordered domains and raise the proportion of less ordered material in the fiber wall [16, 68-70]. As a result, the swelling response is not only a matter of total uptake, but also of how it is expressed structurally within an intact fiber [48]. Water retention value (WRV) is widely used as an empirical indicator of the fiber's swelling propensity [48, 59, 66, 71]. However, WRV alone does not reveal how swelling is distributed within the fiber wall or how fiber morphology changes during hydration. X-ray scattering and light microscopy therefore provide complementary information on swollen fibers. In this thesis, wide- and small-angle X-ray scattering are used to assess nanoscale structural changes, whereas polarized light microscopy, differential interference contrast microscopy, and CLSM are used to visualize fiber swelling, morphological heterogeneity, and wall deformation at the single-fiber level. This combination enables structural reorganization to be related to the observed swelling behavior across length scales.

2.2.2 Nanoscale organization as a determinant of fiber wall swelling

The swelling behavior of a cellulose fiber wall is constrained by its internal nanoscale organization of fibrils [35, 72, 73]. Parameters such as crystalline domain size

and the spacing between fibrillar structural units influence how readily the wall can accommodate water and undergo expansion [18, 19, 57, 74]. In unmodified cellulose-rich fibers, the coexistence of ordered and less ordered regions already creates a heterogeneous structural landscape. After DALC modification, this balance is expected to shift further, because ring opening of the repeating units is associated with reduced structural order and altered mechanical response of the material [16, 18, 19, 51, 57-59, 69, 70, 74]. In studies of cellulose fibers, small-angle X-ray scattering is commonly used to probe the characteristic distances on length scales of several to tens of nanometers, while wide-angle X-ray scattering provides information about lattice-related diffraction and the apparent dimensions of coherently diffracting domains at the Ångström level [35, 73, 75-77].

2.3 Fiber surface composition

2.3.1 Fiber-network surfaces and interfacial function

While chemical modification and drying history illustrate how cellulose-rich fiber walls can be reorganized internally, many application-relevant properties of fiber-based materials are controlled at the exposed surface, where chemical composition and molecular organization determine interfacial behavior. In paper and related fiber-sheet systems, interfacial phenomena such as fiber–fiber bonding, wettability, adhesion, and coating response depend more directly on the chemical composition of the exposed outer surface than on the bulk composition of the material [25, 26, 78-81]. For lignocellulosic fibers, this distinction is especially important because the outermost surface is chemically heterogeneous and may contain different relative contributions of cellulose, hemicelluloses, lignin, and extractives depending on pulping, bleaching, drying, and subsequent processing [25, 26, 82, 83]. Hence, the surface composition should not be regarded as a passive reflection of the bulk. Components such as lignin and extractives can be enriched or depleted at the surface depending on the pulp processing [83, 84].

2.3.2 Surface-sensitive chemical characterization of lignocellulosic materials

Conventional bulk methods do not resolve the outermost surface chemistry, making surface-sensitive analytical techniques necessary [25, 26, 83-85]. ToF-SIMS is particularly relevant in this context because it provides chemically resolved, label-free molecular information from the outermost surface region while also offering high lateral resolution and the possibility of chemical imaging [86-90]. For

lignocellulosic materials, this makes ToF-SIMS especially valuable for probing heterogeneous fiber and paper surfaces.

At the same time, chemically meaningful interpretation of ToF-SIMS data from lignocellulosic substrates is not straightforward. In ToF-SIMS, primary-ion impact generates secondary ions whose composition does not map directly onto the original molecular structure, since many ions form through cleavage and recombination within the collision cascade rather than as pre-existing pieces of the parent molecule (the underlying mechanism is detailed in **Section 2.4.3**); as a result, peak overlaps, matrix effects, contamination, and local surface heterogeneity can further complicate direct assignment [85, 91-93]. This is particularly relevant when differentiating carbohydrate-rich surfaces, where many of these secondary ions are not unique to a single polymer class [85, 88, 91]. For this reason, **Paper III** in this thesis treats ToF-SIMS not simply as a measurement tool, but as an analytical framework requiring conservative interpretation, reference-guided comparison, and structured chemometric analysis [91, 94, 95].

2.3.3 Surface treatment-induced reorganization in fiber sheets

Surface chemistry in fiber-based materials can change substantially during processing. During processing, chemically mobile components may redistribute, become enriched at interfaces, or be masked by other species, thereby altering the effective surface composition without necessarily changing the bulk composition to the same extent [96-98]. This is especially important under thermal and mechanical treatment, where changes in molecular mobility, local softening, and interface formation may drive a reorganization of lignin- and extractive-related species at the sheet surface. For cellulose-based materials, this means that processing history must be considered as more than a manufacturing detail.

The CTMP sheet system investigated in **Paper IV** shifts the focus from chemically induced structural changes in DALC fibers to processing-induced surface reorganization. CTMP sheets retain more lignin and extractives than bleached cellulose-rich fibers, and lignin is enriched at the fiber surface. Their surfaces are therefore chemically heterogeneous and well suited for studying thermally induced surface redistribution [90, 98, 99]. The central background issue is that thermal treatments may alter which components dominate the exposed surface and thus

modify interfacial behavior in ways that cannot be inferred reliably from bulk analysis alone [96, 100, 101].

2.4 Analytical framework for multiscale study

No single analytical technique can resolve the full pathway from molecular modification to interfacial function in cellulose-based materials. This thesis combines optical microscopy, SAXS/WAXS, and ToF-SIMS coupled with chemometrics to examine complementary length scales of the fiber hierarchy: fiber-scale swelling morphology (micrometers), nanoscale fiber wall arrangement and crystalline order (Ångström to tens of nanometers), and surface-chemical fingerprints of the outermost nanometers in fiber-sheet systems. This multiscale approach provides the basis for linking chemical modification, drying history, and thermo-mechanical processing to the structural and interfacial responses of cellulose-based materials. The following sections summarize the analytical principles, structural sensitivity, and thesis-specific roles of the main techniques used in this work.

2.4.1 Optical microscopy

Three different optical microscopy techniques are used to visualize fiber morphology and to assess how swelling and deformation are expressed at the single-fiber level. Figure 2.4.1 summarizes how polarized light microscopy, differential interference contrast (DIC) microscopy, and confocal laser scanning microscopy (CLSM) provide complementary information on fiber morphology, swelling heterogeneity, and spatially resolved wall deformation. Polarized light microscopy reveals birefringence and orientation-dependent optical contrast and is therefore useful for identifying changes in structural anisotropy within cellulose-rich fiber walls (**Figure 2.4.1a**). DIC microscopy enhances phase-gradient contrast between the specimen and its background and makes fiber contours, edges, and local wall deformations more clearly visible by creating a pseudo-3D effect (**Figure 2.4.1b**). CLSM adds optical sectioning and 3D reconstruction, allowing the spatial distribution of swollen or deformed regions to be examined in greater detail (**Figure 2.4.1c**).

These optical microscopy techniques are combined to show how chemical modification and hydration are translated into visible morphological responses. WRV measurements indicate the overall swelling capacity of a fiber population;

they do not capture the spatial heterogeneity of swelling at the single-fiber level. Optical microscopy complements this information by showing whether swelling is localized or uniformly distributed, whether deformation occurs in specific wall regions, and how the swelling response differs between fibers.

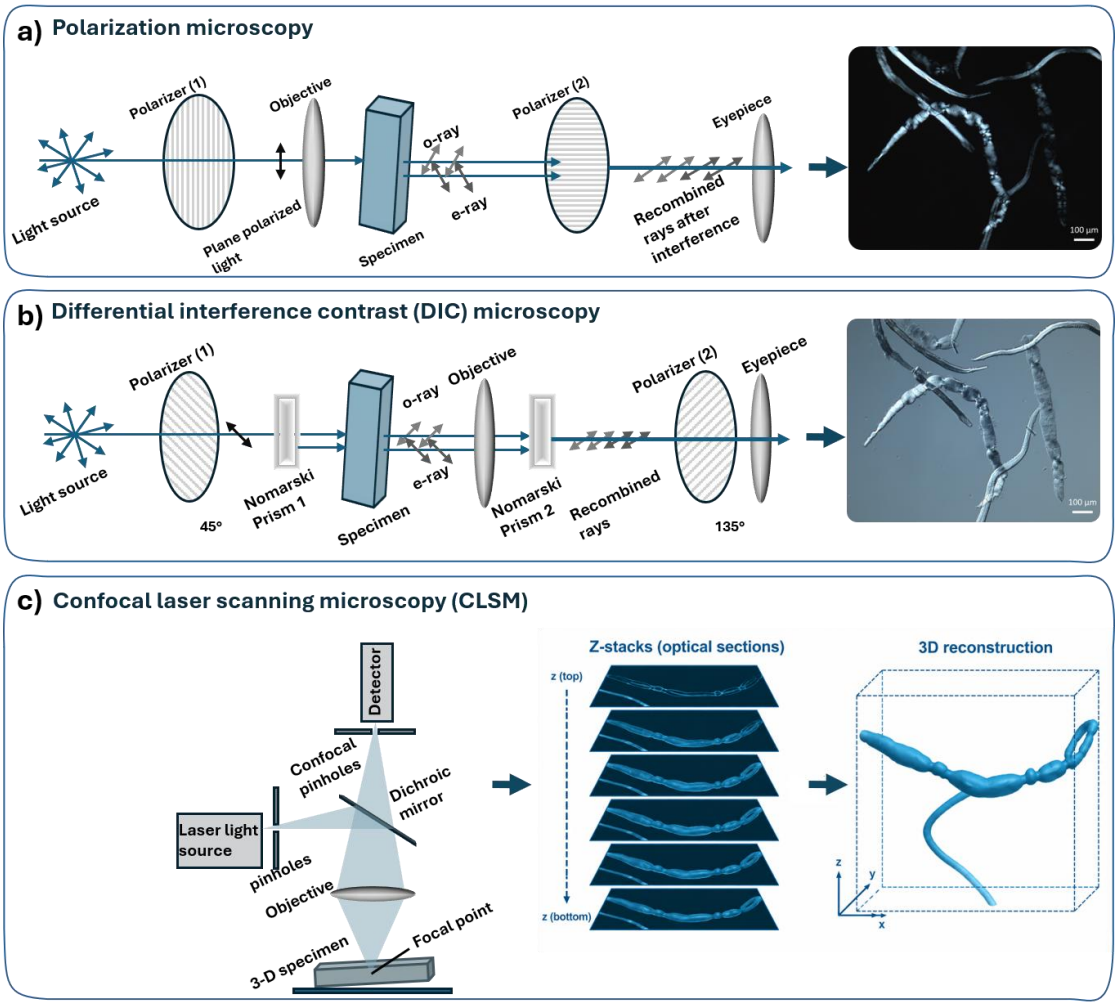


Figure 2.4.1: *Schematic representation of the principles and representative outputs of the optical microscopy techniques used for fiber-morphology analysis. (a) Polarized light microscopy visualizes birefringence and orientation-dependent optical contrast. (b) DIC microscopy enhances phase-gradient contrast and reveals local surface and wall deformation features with a pseudo-3D appearance. (c) CLSM provides optical sectioning, z-stack acquisition, and 3D reconstruction of fiber*

morphology. Polarization and DIC images are adapted from Paper I [48]. The CLSM z-stack and 3D reconstruction are illustrations generated with ChatGPT (OpenAI).

2.4.2 Small- and wide-angle X-ray scattering

Small- and wide-angle X-ray scattering (SAXS/WAXS) were used to examine how chemical modification and drying history influence fiber wall arrangement at the nanoscale. Unlike optical microscopy, which visualizes fiber morphology directly, X-ray scattering probes the internal structural arrangement within the fiber wall. SAXS is sensitive to electron-density variations on length scales of several to tens of nanometers, such as the spacing between fibrils and water- or air-filled voids, whereas WAXS probes the Ångström-scale periodicity of the crystal lattice and therefore provides information on crystalline order and the size of coherently diffracting domains.

For cellulose-based fibers, these structural features are important because swelling and drying depend not only on changes in external fiber dimensions but also on how the internal wall structure accommodates water and undergoes structural rearrangement. Changes in fibrillar arrangement, nanoscale spacing, and crystalline order can therefore help explain differences in swelling behavior, reversibility after drying, and sensitivity to chemical modification. In this thesis, SAXS and WAXS are used as complementary methods to connect visible fiber-level morphology to underlying wall-level structural changes (**Figure 2.1.1**). The SAXS/WAXS measurement principle and structural information accessible across different scattering regimes are summarized in **Figure 2.4.2.**

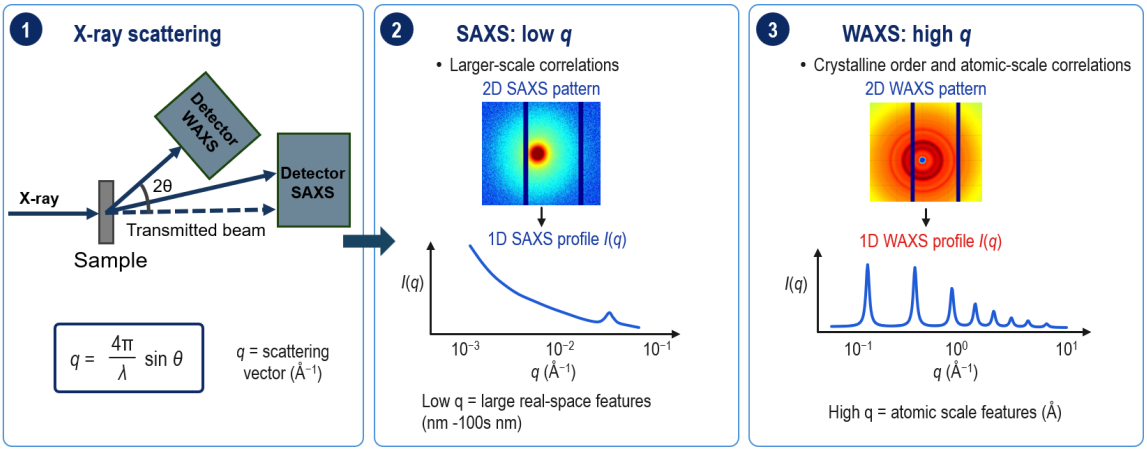


Figure 2.4.2: *Schematic overview of the SAXS/WAXS measurement principle and the type of structural information obtained across scattering regimes. The 2D*

scattering patterns are the author's own data (Paper II). The 1D curves are illustrations generated with ChatGPT (OpenAI) and do not represent measured data.

In SAXS, the measured intensity arises from both the scattering behavior of individual structural features and the spatial correlations between them. For heterogeneous fibrous materials, the scattering intensity can be expressed in the general form,

$$I(q) = AP(q)\,S(q) + B \qquad \textbf{Equation 1}$$

where the form factor P(q) describes single-object scattering (object size/shape and internal contrast profile), and the structure factor S(q) describes inter-object correlations arising from short-range positional order within the fiber wall. *A* is a scale factor capturing contrast, illuminated volume, and concentration terms, while *B* accounts for background scattering, including the Kapton window and, for wet samples, water-related contributions [102, 103]. For cellulose-rich fiber walls, SAXS profiles typically exhibit a broad mid-q feature rather than a sharp Bragg peak, indicating short-range nanoscale correlations rather than long-range crystalline order. Consequently, SAXS is particularly useful for probing characteristic length scales associated with fibrillar arrangement, interfibrillar spacing, and network structure.

In contrast, WAXS probes shorter length scales and provides information on the crystalline arrangement of cellulose. In this work, the apparent crystallite width along the cellulose Iβ (200) plane was estimated using the Scherrer equation.

$$\text{Apparent crystallite width}_{(200)} = \frac{2\pi K}{\Delta q} \qquad \textbf{Equation 2}$$

where K = 0.9 is the shape factor and Δq is the full width at half-maximum (FWHM) of the (200) diffraction peak, corrected for instrumental broadening (Δq = Δq_measured − Δq_instrumental). The instrumental broadening was determined

using a LaB_6 calibrant [104, 105]. The peak-fitting procedure used to obtain Δq for the (200) reflection is described in **Section 3.6.1**, **Equation 7-9**.

2.4.3 Time-of-flight secondary ion mass spectrometry

ToF-SIMS is a surface-sensitive mass spectrometric technique in which a pulsed primary ion beam, here typically Bi_3^+, bombards the outermost surface of the sample under high vacuum. The impact triggers a collision cascade within the near-surface region (1–3 nm). The collision cascade results in the emission of atoms, molecular species, clusters, and electrons, as shown in **Figure 2.4.3**. Most emitted atomic and molecular species are neutral, whereas a small fraction leaves the surface as positive or negative secondary ions; only these charged species are detected and retain chemically specific information from the uppermost molecular layers.

The intensity of a detected secondary ion is described by the basic SIMS equation:

$$I_i^{\pm} = I_p \,.\, Y \,.\, \alpha^{\pm} \,.\, C_i \,.\, \eta \qquad \textbf{Equation 3}$$

where $I_i^{\pm}$ is the measured secondary-ion current for *species i in charge* state ±, I_p is the primary-ion current, Y is the sputter yield, $\alpha^{\pm}$ is the ionization probability, C_i is the fractional surface concentration of species *i*, and η is the instrumental transmission efficiency.

Among these terms, the ionization probability $\alpha^{\pm}$ is the origin of the well-known matrix effect in SIMS: it depends strongly on the local chemical environment. For example, the presence of neighboring electronegative species such as oxygen can substantially enhance positive-ion yields. Hence, nominally identical chemical species can exhibit markedly different ion yields depending on their surrounding matrix. Consequently, secondary-ion intensities cannot generally be converted into absolute concentrations without matrix-matched reference standards, which is why this thesis's ToF-SIMS workflow relies on compacted reference materials for conservative, semi-quantitative marker-ion validation rather than direct quantification, consistent with **Equation 3**, (see **3.7 ToF-SIMS surface analysis and chemometrics**)

Only a small fraction of the sputtered species Y in **Equation 3** is emitted as secondary ions, but these ions retain chemically specific information from the

uppermost molecular layers. Immediately after emission, the secondary ions are accelerated by an extraction field, for which the kinetic energy is approximated by

$$\frac{1}{2}\mathbf{mv^2} = \mathbf{zeV} \qquad \textbf{Equation 4}$$

where *z* is the ion charge, e is the elementary charge equivalent to 1.602×10^{-19} C, and *V* is the accelerating voltage.

The ions then traverse a field-free flight tube and are separated according to their mass-to-charge ratio, since

$$t = L\sqrt{\frac{m}{2zeV}} \qquad \approx \qquad \frac{m}{z} \propto t^2 \qquad \textbf{Equation 5}$$

where t is the flight time, m the ion mass, and L the total flight path from the sample to the MCP (microchannel plate detector). Combining the ion velocity from **Equation 4** with the flight-time relation (**Equation 5**) gives the mass-to-charge dependence exploited for calibration. In the reflectron sketch shown in **Figure 2.4.3**, the ions traverse the drift region twice, and the reflectron corrects for the energy spread neglected in **Equation 4**, thereby improving mass resolution. After calibration, each arrival time is converted to a mass-to-charge value (*m/z*) via the relation in **Equation 5**; the resulting distribution of ion counts constitutes the mass spectrum [106, 107].

In practice, a ToF-SIMS instrument can be operated in two complementary acquisition modes that trade mass resolution against spatial resolution. In bunched mode, the primary-ion pulse is compressed in time to maximize time-of-flight separation, giving high mass resolution over a defined analysis area, but with the beam focused to a small spot size; this mode is used to acquire representative mass spectra for peak assignment and quantitative comparison. In burst-alignment mode, the beam is instead focused to a fine spot and rastered across the sample to build up spatially resolved ion images, at the cost of reduced mass resolution. The two modes therefore serve different purposes: bunched mode for chemically resolved, spectrum-level analysis, and burst-alignment mode for spatially resolved

surface mapping. Both modes are used in this thesis, as detailed in **3.7.1 Instrument configuration**.

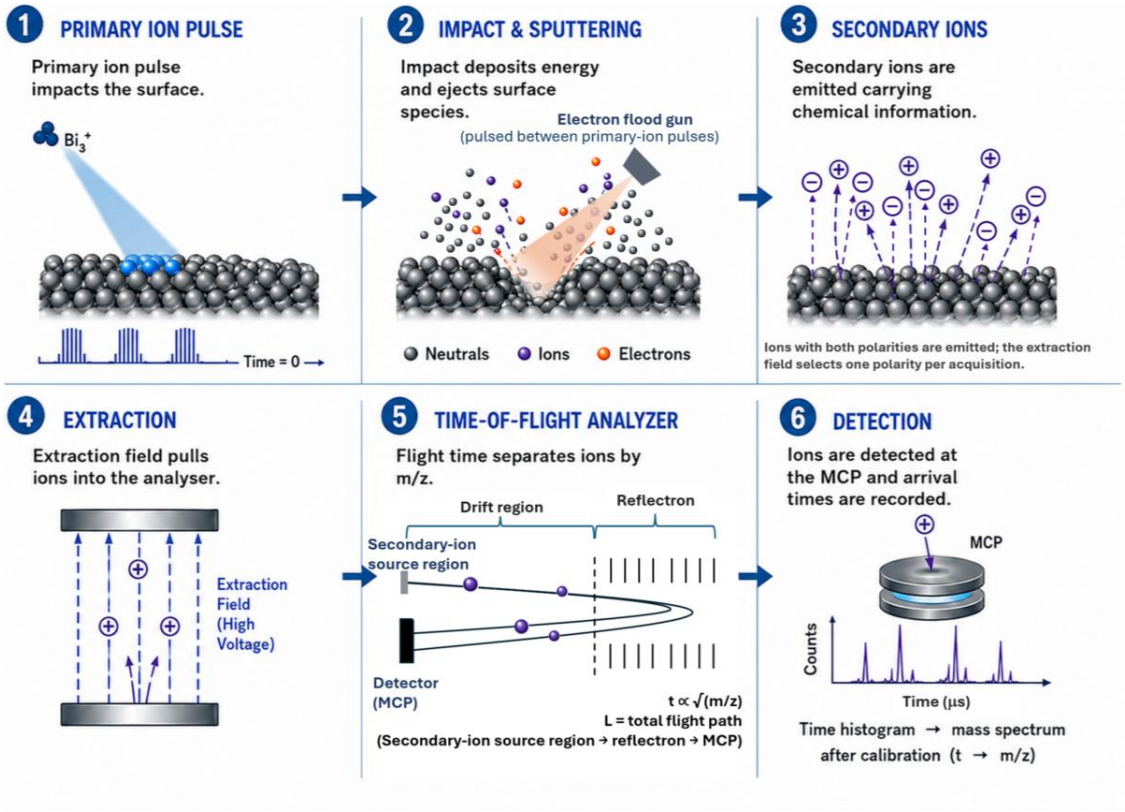


Figure 2.4.3: *Schematic representation of the ToF-SIMS operating principle, including primary-ion impact, secondary-ion generation, extraction, time-of-flight analysis, and detection. Schematic generated with ChatGPT (OpenAI) based on the author's prompts and was checked and edited by the author.*

To preserve surface specificity, ToF-SIMS measurements are typically performed within the static SIMS regime, in which the cumulative primary-ion dose is kept low enough (conventionally below ~10^{13} ions cm^{-2}) that, on average, each surface site is struck no more than once during acquisition. Operating within this regime ensures that the collision cascades sampled throughout the measurement originate from a largely undamaged surface, so that the resulting spectrum reflects the outermost molecular layers rather than progressively sputtered, sub-surface, or beam-damaged material. Exceeding the static limit causes cratering and mixing of near-surface layers, degrading depth resolution and biasing the measured chemistry toward bulk composition. The specific acquisition parameters used to

maintain static conditions in this work are discussed in **3.7.1 Instrument configuration**.

For insulating samples such as cellulose-rich fibers, primary-ion bombardment can produce positive surface charging, which distorts ion trajectories, shifts apparent *m/z* values, and reduces mass accuracy and signal stability. To minimize this, a low-energy electron flood gun is used between analysis pulses to neutralize excess charge and stabilize the surface potential.

2.4.4 Chemometric analysis of complex ToF-SIMS datasets

ToF-SIMS datasets are highly multivariate, with chemically meaningful differences often distributed across many ions rather than confined to a single peak. In cellulose-based materials, direct comparison of spectra is useful but often insufficient for identifying systematic class differences, correlated ion changes, or within-class heterogeneity. Chemometric methods are used in this thesis to extract interpretable patterns from these complex datasets. A range of multivariate analysis methods is available for handling such datasets; in this thesis, principal component analysis (PCA), orthogonal projections to latent structures discriminant analysis (OPLS-DA), and shared and unique structures (SUS) plots are the principal chemometric tools used for data interpretation. The workflow from multivariate ToF-SIMS spectra to PCA, OPLS-DA, and SUS-based data interpretation is schematically shown in **Figure 2.4.4**.

PCA is an unsupervised exploratory method that reduces data dimensionality and reveals the dominant sources of variance without using class information. It is useful for visualizing clustering, trends, and outliers. OPLS-DA is a supervised method that uses predefined class membership to isolate variation associated with a specific comparison while separating unrelated structured variation. It is therefore useful for identifying ions that discriminate between known sample classes, although careful validation is required because the method is supervised. SUS plots are used to compare two related OPLS-DA models and to distinguish variables that are shared between contrasts from those that are unique to one comparison.

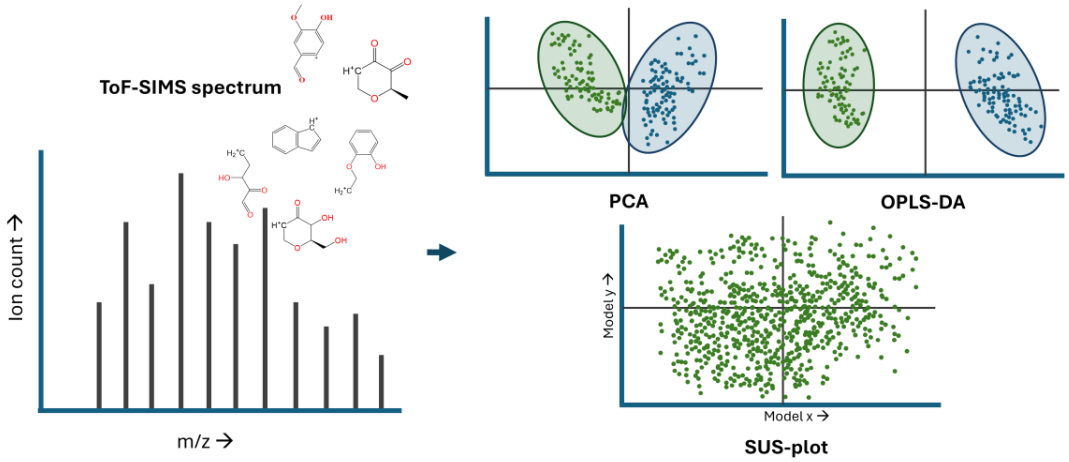


Figure 2.4.4: *Schematic illustration of the chemometrics workflow applied to ToF-SIMS data, from spectral peak intensities to multivariate score-plot interpretation.*

These methods provide complementary levels of interpretation: PCA gives an overview of the main variance structure, OPLS-DA focuses on class-discriminating variation, and SUS plots resolve whether discriminating variables are shared or unique across related comparisons. For complex ToF-SIMS datasets from lignocellulose-based materials, this chemometric framework provides a structured basis for linking multivariate spectral patterns to chemically interpretable differences in surface composition.

3 Materials and Methods

3.1 Materials

3.1.1 Reference polysaccharides and lignin

Microcrystalline cellulose (MCC; Sigma-Aldrich, cat. 435236; nominal particle size 51 µm) and beechwood xylan (Sigma-Aldrich, X4252; CAS 9014-63-5; ≥90% xylan) were used as received. Galactoglucomannan (GGM) was kindly provided by Stora Enso AB (Karlstad, Sweden) and produced as described elsewhere [108]. GGM was recovered from thermomechanical pulping process water, concentrated by membrane filtration, and precipitated with ethanol. Its approximate monosaccharide composition, expressed as galactose:glucose:mannose, was 0.8:1:4.1. The powder was stored in sealed containers under ambient conditions, with no additional drying before compaction. Softwood Kraft pulp lignin (SKPL) was prepared by Åke Henrik-Klemens and provided for this work; preparation details are reported elsewhere [109]. Briefly, SKPL was isolated from unbleached, never-dried softwood Kraft pulp by enzymatic hydrolysis of holocellulose followed by mild acidolysis in dioxane/water, according to protocols adapted from elsewhere [110, 111]. The sample contained 0.8 wt% ash, 0.9 wt% residual carbohydrate, and 4.7 wt% protein, estimated from CHN nitrogen using an 8×N factor, corresponding to a lignin purity of 93.6% after subtraction of ash and protein. Full compositional and inorganic analyses of the pulps are provided in the **supplementary table ST 1–3 of Paper III**.

3.1.2 Kraft pulps for handsheets

Never-dried, unbleached and bleached softwood Kraft pulps (USK and BSK; Stora Enso, Skoghall, Sweden; spruce/pine mix) were used to prepare handsheets for evaluating the reference-supported ToF-SIMS workflow. The pulps differed strongly in lignin content, with 13.0 wt% total lignin in USK and 1.1 wt% in BSK, providing a chemically relevant contrast between lignin-richer and carbohydrate-richer fiber surfaces.

3.1.3 CTMP paper

CTMP paper was supplied by Stora Enso (Sweden) as described previously [99]. The chemical composition of the unbleached softwood CTMP was determined on oven-dried material. Acetone extractives were quantified gravimetrically after

Soxhlet extraction (≥99.8% acetone, 4.5 h), and acid-insoluble (Klason) lignin by two-stage sulfuric acid hydrolysis (72 wt% H_2SO_4, 30 °C for 60 min, followed by dilution and autoclaving at 125 °C for 60 min). The CTMP contained 27.3 wt% Klason lignin and 0.63 wt% extractives, consistent with previously reported values for Stora Enso CTMP [112].

3.2 Sample preparation

3.2.1 Fibers for DALC modification

DALC fibers were kindly provided by Tetra Pak. They were prepared from bleached softwood Kraft pulp (Stora Enso) by periodate oxidation followed by borohydride reduction as described in **Paper I** [48]. The degree of modification (DOM) was determined by Tetra Pak by hydroxylamine hydrochloride titration [113] to be 3.1, 5.0 and 5.8 mmol g^{-1} fiber, corresponding, assuming pure cellulose, to DOM of 26%, 44% and 51% (DALC-26DOM, DALC-44DOM and DALC-51DOM). Never-dried, unmodified bleached softwood Kraft pulp (Kraft-0DOM) was used as the reference.

3.2.2 Preparation of bench-dried and rewetted fibers

Portions of the never-dried fibers were bench-dried at ambient temperature for 2–3 days. For rewetted samples, water was added depending on the characterization technique, and the fibers were equilibrated for 24 h prior to analysis.

3.2.3 Kraft handsheet preparation

Handsheets of never-dried bleached softwood Kraft (BSK) and unbleached softwood Kraft (USK) pulps were prepared by Åke Henrik-Klemens and provided for this work. They were prepared using a Rapid Köthen sheet former (Paper Testing Instruments, Laakirchen, Austria) and a sheet dryer (Lorentzen & Wettre, Sweden), according to ISO 5269-2:2004 and TAPPI/ANSI T 205 sp-18, as described in Paper III [63].

3.2.4 Preparation of compacted reference surfaces

To obtain flat and uniform reference surfaces for ToF-SIMS, MCC, GGM, xylan, and SKPL powders were compacted using flat punches with a diameter of 12 mm on an Ellipse manual press, model HA 03 - 451 TO101 02. Compaction was used to minimize topography-induced ion-yield variations and to avoid background contributions from mounting media (e.g., double-sided tape).

3.2.5 CTMP paper hot-pressing samples and sampling

Industrially hot-pressed CTMP paper sheets (100 and 200 °C) were supplied by Stora Enso. Pieces were cut from each sheet to allow ToF-SIMS analysis of both the front- and back-side surfaces. Six independent spectra were acquired per side and temperature, using identical sampling and mounting procedures for all specimens to enable comparison of side- and temperature-dependent surface chemistry.

3.3 Gravimetric determination of fines

Fines content in unmodified and DALC fibers was determined using a Britt Dynamic Drainage Jar (BDDJ) fitted with a 76 µm circular-hole screen. Samples corresponding to 0.5 g dry mass were dispersed in 1.5 L of water and screened at 800 rpm, with the impeller oriented toward the screen to reduce sedimentation. The retained fiber fraction was oven-dried and weighed.

3.4 Water retention value

Fiber swelling propensity was quantified using a mini WRV method. Fiber pads corresponding to 0.05 g dry mass were prepared in UFC40SV25 Ultrafree-CL centrifugal filter units (Sigma-Aldrich) and centrifuged for 30 min at 3000 ± 50 g. Pads were weighed after centrifugation, oven-dried at 105 °C overnight, and reweighed. WRV was reported as grams of water per gram of dry fiber. Centrifugation was performed at 23 ± 3 °C. All samples were measured in duplicate. Where relevant, BDDJ screening was performed prior to WRV measurements to reduce the influence of fines on the gravimetric swelling estimate.

3.5 Light microscopy

3.5.1 Optical microscopy and image analysis

Optical micrographs were acquired using a ZEISS microscope (Oberkochen, Germany) at 100x magnification in reflected-light mode. Cross-polarized images were collected with an exposure time of 300–330 ms, and differential interference contrast (DIC) images with an exposure time of 500 ms.

Wet and swollen fibers were imaged on a glass slide (76 mm x 26 mm x 1 mm; VWR) with a coverslip (60 mm x 26 mm; Menzel-Gläser). Coverslip edges were sealed with nail polish to limit evaporation during imaging. Fibers were imaged while suspended in excess water. Fiber widths were measured manually in ImageJ (Maryland, USA).

3.5.2 Confocal laser scanning microscopy

Confocal imaging was performed using a Leica SP2 CLSM (Leica Microsystems GmbH, Wetzlar, Germany) equipped with a 20x water-immersion objective (NA = 0.5). Images were acquired at 1x or 2x digital magnification. DIC images were acquired at 1920 x 1200 pixels (0.386 µm px^{-1}), and confocal images at 512 x 512 pixels (1.239 µm px^{-1}) at two images per second. The pinhole was set to 1 Airy unit.

A 100-mW argon laser was operated at 25% power. Calcofluor white and fluorescein isothiocyanate (FITC)-dextran (10 kDa) were used for fluorescence imaging. Calcofluor was excited at 350 nm, and emission was collected at 432 nm. FITC-dextran was excited at 490 nm, and emission was collected at 520 nm. FITC-dextran was added to fiber suspensions and allowed to diffuse overnight, whereas Calcofluor was added immediately prior to imaging. Three representative videos were collected per sample.

3.6 X-ray scattering

Small- and wide-angle X-ray scattering (SAXS/WAXS) measurements were performed on the Mat:Nordic instrument (SAXSLAB/Xenocs) using a Rigaku MicroMax-003+ microfocus Cu-Kα source (λ = 1.5406 Å) and Pilatus 300K/100K detectors. Measurements covered q = 0.003–3 $Å^{-1}$ using ESAXS, SAXS, MAXS, WAXS, and EWAXS configurations. Sample-to-detector distances were approximately 1534, 1084, 484, and 134 mm for ESAXS, SAXS, MAXS, and WAXS, respectively; for EWAXS, the distance was reduced to <25 mm using a 3D-printed extender to reach q values up to 3 $Å^{-1}$ and cover the onset of the water peak near q ~ 2 $Å^{-1}$. Beam diameters ranged from 0.2 to >0.9 mm depending on configuration. Measurements were conducted at 25 °C under a beam-path pressure of 1–2 mbar.

Because the instrument operates under vacuum, hydrated samples were mounted in hermetically sealed sandwich cells with Kapton windows, whereas bench-dried samples were mounted directly on the sample holder using tape. Bench-dried samples were exposed for 60 min, while never-dried and rewetted samples were exposed for 90 min to compensate for water attenuation. Background measurements included Kapton windows, empty cells/capillaries, and water, acquired using comparable exposure times.

Absolute intensity calibration was estimated by comparison with the direct-beam intensity. Data reduction was performed using SAXSGUI v2.27.03, followed by

thickness correction and background subtraction in Origin. Kapton contributions were removed using empty-window measurements, and the water contribution was obtained from capillary measurements after subtraction of the empty-capillary background. WAXS measurements were performed on two independent sample sets and SAXS measurements on three independent sample sets; reported profiles represent the corresponding averages.

3.6.1 Determination of crystallinity index and crystal domain width from WAXS data

For WAXS, the crystallinity index was estimated using the Segal peak height method [114]. I_200 is the intensity of the (200) peak at q around 1.59 $Å^{-1}$, and I_am is the intensity at q equal to 1.3 $Å^{-1}$.

$$\text{Crystallinity index}_{\text{(Segal Peak Height Method)}} = 100 \times \left(\frac{I_{(200)} - I_{am}}{I_{(200)}}\right) \qquad \textbf{Equation 6}$$

Peak fitting (also referred to as peak deconvolution) was used to determine the average domain width of the crystal. The Voigt function was used to fit the five peaks observed in the diffractogram of fibers, along with a broad Gaussian-like peak accounting for the non-crystalline region [115].

$$\boldsymbol{Voigt}\,(x, \sigma, \gamma) = \int_{-\infty}^{\infty} \boldsymbol{G}(x'; \sigma)\boldsymbol{L}(x - x'\gamma)dx' \qquad \textbf{Equation 7}$$

where G (x, σ) and L $_{(x,\ \gamma)}$ are the Gaussian and Lorentzian curve profiles, respectively, and are given by

$$\mathbf{G}_{(x;\sigma)} = \frac{1}{\sigma\sqrt{2\pi}} \exp\left(-\frac{x^2}{2\sigma^2}\right) \qquad \textbf{Equation 8}$$

$$\mathbf{L}_{(x;\gamma)} = \frac{\frac{\gamma}{\pi}}{x^2 + \gamma^2} \qquad \textbf{Equation 9}$$

where γ is the half-width at half-maximum (HWHM) of the Lorentzian profile and σ is the standard deviation of the Gaussian profile, related to its HWHM.

Using the fitting parameters obtained from **Equation 7 - 9**, the apparent crystallite width perpendicular to the (200) planes of cellulose Iβ was determined using the Scherrer equation (**Equation 2**), where K = 0.9 is the shape factor, and Δq is the instrument-corrected full width at half-maximum (FWHM) of the fitted (200) reflection in reciprocal space, obtained as $\Delta q = \Delta q_{measured} - \Delta q_{instrumental}$, with the instrumental broadening determined from a LaB_6 calibrant.

3.6.2 SAXS data analysis

Building on the general SAXS expression in **Equation 1**, the following model-fitting approaches represent two different ways of treating the form-factor and structure-factor contributions: WoodSAS provides a physically constrained description of nanofibrillar cylinder packing in the dry state, whereas the empirical network model provides a less geometry-specific description of correlation features in hydrated, disordered fiber wall networks.

3.6.2.a Kratky analysis

SAXS profiles of fiber walls show broad features. To compare samples, Kratky plots, $I(q)q^2$ versus q, were used. Multiplying the intensity by q^2 compensates for the steep decay of I(q) with increasing q, so that broad, weak scattering features appear as a distinct maximum whose position can be located. The position of this maximum, q*, was used to calculate a characteristic length, ℓ_k, as

$$\ell_k = \frac{2\pi}{q^*} \qquad \textbf{Equation 10}$$

This relation is commonly used in SAXS to convert the position of a broad scattering feature into a typical distance in the sample [103]. However, this method does not differentiate between the form- and structure-factor contributions encompassed in the SAXS data (**Equation 1**) in concentrated systems such as those investigated in this thesis. Hence, the Kratky method was used together with model-based fitting to understand and interpret the nanoscale structural arrangement in DALC fibers as follows.

3.6.2.b Empirical network model for wet samples

For wet-state samples, an empirical network model was used, since hydrated fibers are better represented as swollen and disordered nanofibrillar networks [116]. The model used is

$$\mathbf{I(q) = \frac{A}{q^n} + \frac{C}{1 + (\xi q)^m} + B} \qquad \textbf{Equation 11}$$

where the first term represents large-scale network scattering, with exponent n, the second term describes a correlation contribution with correlation length ξ, and B accounts for background scattering. In this expression, A, C, n, and m are empirical fitting parameters. This model does not separate P(q) and S(q) **Equation 1**. Thus, ξ is a characteristic network length, not an exact distance. A lower n means a more open network.

3.6.2.c WoodSAS model for dry samples

Bench-dried SAXS data were analyzed and model-fitted in SasView v6.1.0 (Zenodo DOI: 10.5281/zenodo.15775666) using the Levenberg–Marquardt fitting optimizer implemented in SasView. The WoodSAS model was applied via the SasView Model Marketplace plugin (woodsas.py) [75], to describe nanofibril packing and paracrystalline disorder in the fiber wall. The model treats the nanofibrils as infinitely long cylinders in hexagonal packing with a paracrystalline lattice distortion.

$$\mathbf{I(q) = A \cdot I_{cyl}\,(q, \bar{R}, \Delta R, a, \Delta a) + B \cdot \exp\frac{-q^2}{(2\sigma^2)} + C \cdot q^{-\alpha}} \qquad \textbf{Equation 12}$$

where the cylindrical scattering term I_{cyl} describes the combined form-factor and structure-factor contributions from cellulose nanofibrils treated as infinitely long cylinders arranged in distorted hexagonal packing. The mean nanofibril radius $\bar{R}$ and radius distribution ΔR primarily govern the form-factor contribution, whereas the interfibrillar spacing a and paracrystalline disorder Δa describe the structure-factor contribution (**Equation 1**). The Gaussian term accounts for a broad low-q contribution, and the power-law term describes larger-scale background scattering. In the present work, WoodSAS fitting was used to extract physically

meaningful descriptors of dry fiber wall organization and to evaluate how these descriptors change with dialcohol cellulose modification.

3.7 ToF-SIMS surface analysis and chemometrics

ToF-SIMS was used to characterize the outermost surface composition of cellulose-based fiber, handsheet, and paper samples. Two ToF-SIMS datasets are included in this thesis: (i) BSK and USK handsheets analyzed together with compacted reference samples, including MCC, GGM, xylan, and SKPL, to support marker-ion assignment, and (ii) CTMP paper hot-pressed at 100 and 200 °C and analyzed on both front/heated-nip and back surfaces.

3.7.1 Instrument configuration

ToF-SIMS measurements were performed using an IONTOF instrument (IONTOF GmbH, Münster, Germany) equipped with a bismuth liquid metal ion gun operated with a Bi_3^+ cluster primary beam.

For Kraft handsheets and compacted reference surfaces, the instrument was operated at 30 keV. Spectra were acquired in bunched mode over a 100 × 100 to 500 × 500 µm² area (primary ion current I_p, **Equation 3**, of 0.35–0.45 pA; cycle time of 100–125 µs; 20 scans), with the Bi_3^+ beam focused to a nominal spot size of ~1 µm. Under these conditions, the mass resolution (m/Δm, FWHM at m/z 200) was ≥2000 for the unbleached handsheet and ≥1700 for the bleached handsheet; mechanically compacted reference surfaces yielded m/Δm ≥6000.

Imaging was performed in burst-alignment mode over a 500 × 500 µm^2 field of view using a random raster with 256 × 256 pixels and 25 scans, with a primary ion current of 0.41 pA; the primary ion dose was kept within static SIMS conditions as discussed in **Equation 13**.

For hot-pressed CTMP papers, spectra were acquired in positive-ion mode using a pulsed Bi_3^+ beam (25 keV, 0.35 pA) over a 500 × 500 µm^2 raster with 15 scans per analysis position and a mass range of *m/z* 0–800.

Static SIMS conditions were maintained by keeping the primary ion dose < 1 × 10^{13} ions cm^{-2}, a commonly used limit below which, on average, each surface site is struck no more than once during acquisition. The dose (*D*) was estimated from the

primary-ion current (I_p) (**Equation 3**), acquisition time (t), and analyzed area (A) according to

$$\mathbf{D} = \frac{\boldsymbol{I_p}\mathbf{t}}{\mathbf{qA}} \qquad \textbf{Equation 13}$$

where q = e = 1.602 x 10^{-19} C.

3.7.2 Charge compensation and acquisition control

Charge compensation was applied during analysis of electrically insulating paper and fiber specimens to stabilize the surface potential and minimize mass-scale drift. For CTMP paper measurements, a low-energy electron flood gun was used for charge compensation.

Acquisition stability was monitored by tracking mass resolution and peak positions during measurement. Spectra exhibiting evidence of residual charging (e.g., peak shifts or broadened peaks) were excluded or reacquired where necessary.

3.7.3 Mass calibration and peak definition

Data acquisition and initial spectral evaluation were performed using SurfaceLab (IONTOF). For Kraft handsheets and compacted reference samples, SurfaceLab version 7.4 was used.

Mass calibration for the Kraft-handsheet dataset was performed separately for lignin-rich and polysaccharide-rich samples to improve mass assignment in the low-mass region. Polysaccharide-rich samples were calibrated using characteristic carbohydrate fragments (e.g., $C_2H_3^+$, $C_3H_5^+$, $C_2H_5O^+$, and $C_6H_{12}O_5^+$), whereas lignin-rich samples were calibrated using aromatic and benzylic ions (e.g., $C_6H_5^+$, $C_8H_9^+$, $C_9H_7^+$, and $C_9H_{11}O_3^+$). A common peak list was generated across all samples, and each peak was defined using a mass-interval tolerance of ±0.03 u. For subsequent analyses, the same interval list was applied to all spectra to ensure consistent peak integration and sample-to-sample comparability.

3.7.4 Normalization and preprocessing

To enable semi-quantitative comparison across specimens, since absolute values of C_i (**Equation 3**) are inaccessible without matrix-matched standards, all spectra and ion images were normalized to the total ion count (TIC). Peak areas were integrated using SurfaceLab software and exported for statistical analysis. For the

Kraft-handsheet dataset, a signal-to-noise ratio threshold of ≥10 was applied for peak detection.

3.7.5 Chemometric workflow

Unsupervised principal component analysis (PCA) was used for exploratory assessment of spectral variance and marker-ion validation. For the Kraft-handsheet dataset, PCA was performed in OriginPro 2023 using the Principal Component Analysis for Spectroscopy application (v1.42), and pairwise comparisons between handsheets and compacted reference samples were used to support conservative marker-ion assignment.

For hot-pressed CTMP papers, chemometric analysis was performed in SIMCA 18. Orthogonal projections to latent structures discriminant analysis (OPLS-DA) was used to distinguish side-dependent and temperature-dependent spectral variation. Shared and unique structures (SUS) plots based on model p(corr) loadings were then used to identify ions associated specifically with hot-pressing temperature. Model validity was assessed using cross-validated analysis of variance (CV-ANOVA; $p < 0.05$) and permutation testing. Marker ions were selected based on combined evidence from p(corr) values, variable importance in projection (VIP ≥ 1.0), and Welch's unequal-variance t-tests on TIC-normalized intensities ($p < 0.05$).

3.7.6 Quality control strategy

Replicate spectra were acquired from multiple surface locations to assess within-sample variability and the robustness of multivariate separation. For the Kraft-handsheet and CTMP paper datasets, six independent spectra were acquired per sample class, side, or treatment condition, as applicable. Quality control included systematic screening for contaminant ions and salt-derived adducts during peak-list curation and marker selection. Reported marker ions were required to be reproducible across replicates and chemically plausible within lignocellulosic fragmentation chemistry.

3.8 Sample nomenclature

To ensure clarity and traceability across the multiscale analyses presented in this thesis, a structured nomenclature was adopted to identify fibers according to their chemical modification and drying history. Sample identifiers follow the general format [Chemistry]–[DOM]_[Drying history], as summarized in the table below.

Table 1: *Sample nomenclature used in this thesis.*

Category	Code	Meaning	Applicability
Chemistry	Kraft-0DOM	Unmodified softwood Kraft pulp	Used as the unmodified reference sample
	DALC-26DOM	Dialcohol cellulose, 26% DOM	Modified cellulose sample; DOM determined by titration
	DALC-44DOM	Dialcohol cellulose, 44% DOM	Modified cellulose sample; DOM determined by titration
	DALC-51DOM	Dialcohol cellulose, 51% DOM	Modified cellulose sample; DOM determined by titration
Drying history	ND	Never-dried	Used for SAXS/WAXS
	BD	Bench-dried	Used for dried-state SAXS/WAXS
	RW	Rewetted after bench-drying	Used for reversibility comparisons in SAXS/WAXS and swelling-related analyses

4 Results and Discussion

4.1 Morphological evolution of DALC fibers with increasing DOM

This section addresses **RQ1** by examining how increasing DALC modification alters fiber wall swelling, morphology, and water retention.

Background: Native cellulose cannot be melt processed, but DALC fibers can [50, 69, 117]. Earlier DALC studies covered crystallinity and dry-state fiber structure [51, 69]. Balloon-collar swelling is well known when cellulose fibers dissolve [67, 118] and in highly charged fibers [119]. How the fiber wall and swelling morphology change with DOM was not known.

Hypothesis: DALC swells like fibers undergoing dissolution. Higher DOM disrupts the secondary wall layers. Swelling first appears as balloon-collar morphology, followed by a transition toward uniform swelling at higher DOM.

Approach: The hypothesis is tested on never-dried fibers at the single-fiber level. Swelling morphology is assessed by DIC and polarized light microscopy and by CLSM with dual fluorescent labeling. The extent of swelling is quantified by WRV and by fiber-width distributions from DIC images [48].

4.1.1 Optical microscopy reveals DOM-dependent heterogeneous swelling

DIC and polarized light microscopy were used to assess fiber-level morphological changes across the DALC series. As shown in **Figure 4.1.1,** increasing DOM progressively enhanced lateral fiber wall swelling in water. Kraft-0DOM fibers remained comparatively uniform, whereas DALC-26DOM showed mild periodic bulging, indicating the onset of heterogeneous swelling. This heterogeneous swelling includes balloon-collar morphology, in which locally swollen segments (balloons) alternate with less-expanded segments (collars) along the fiber (discussed in detail in **Section 4.1.2**).

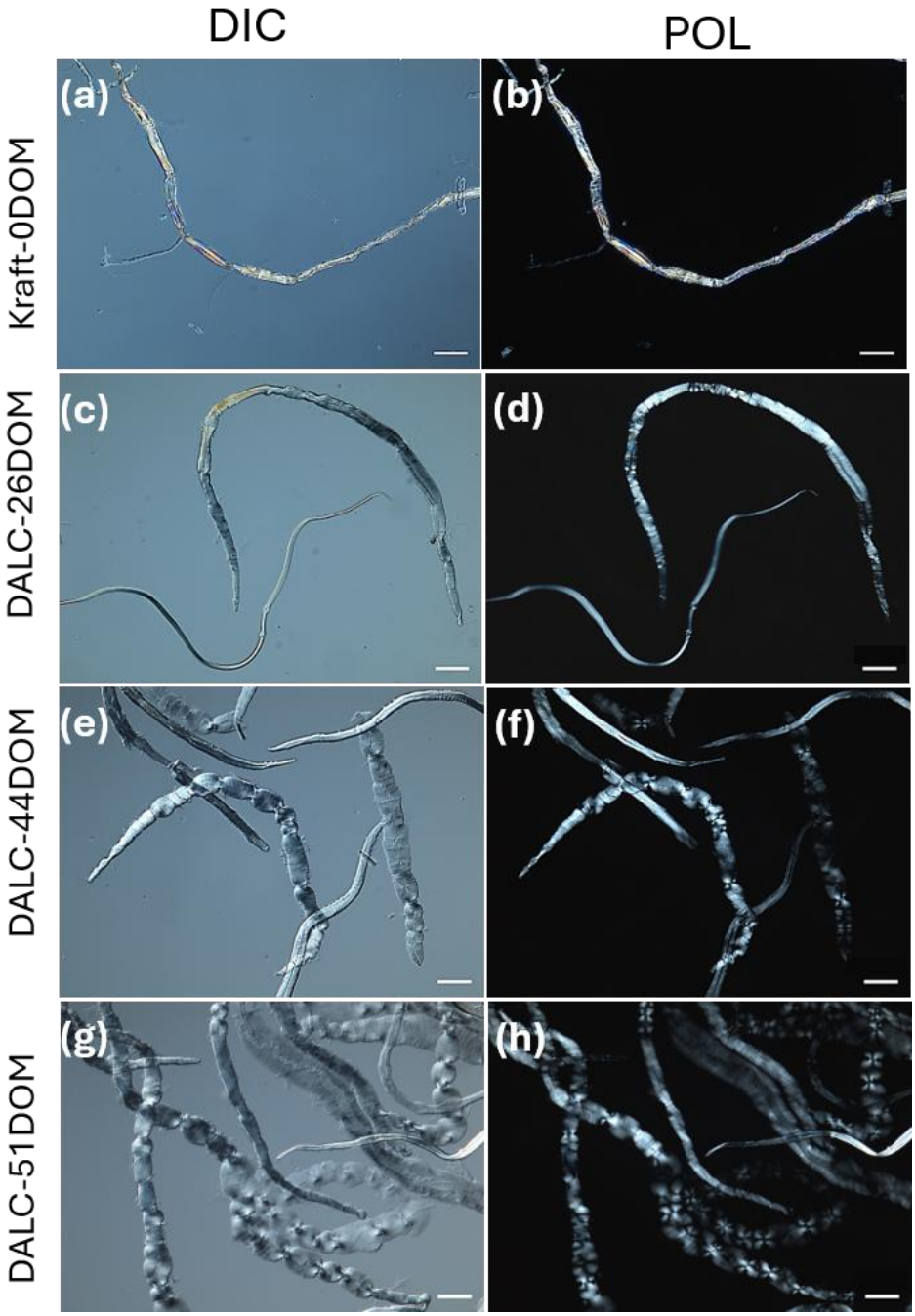


Figure 4.1.1: *Optical microscopy images in DIC mode (left column) and polarization mode (right column). Panels (a,b), (c,d), (e,f) and (g,h) show Kraft-0DOM, DALC-26DOM, DALC-44DOM and DALC-51DOM, respectively. Fibers of the same DOM were imaged in the same field of view in both modes. Scale bars correspond to 100 µm. All images are representative of the corresponding sample set. Adapted from Paper I* [48].

The paired DIC and polarized light images are complementary. DIC enhances topography and highlights fiber wall swelling, damage or external fibrillation, giving a pseudo-3D contrast against the background, whereas polarized light reveals optically anisotropic wall structures associated with nanofibril alignment and ordering (**Figure 4.1.1**). The local balloon-like expansions are consistent with heterogeneous swelling phenomena previously reported for cellulose fibers undergoing partial dissolution in specific solvent environments [18, 65, 67]. Polarized light microscopy is commonly used to reveal birefringent order (e.g., crystalline regions in starch granules and cellulose nanocrystal systems) [120], and birefringence in such systems can arise from repeating structural order (e.g., nematic liquid-crystalline phases) [121, 122]. The birefringence of Kraft-0DOM and DALC-26DOM fibers shows optical anisotropy, which decreases at higher DOM.

4.1.2 Balloon-collar morphology and transition toward uniform swelling

At higher DOM, particularly in DALC-44DOM and DALC-51DOM, ballooned regions frequently displayed Maltese-cross-like interference patterns under polarized light microscopy. This is illustrated in **Figure 4.1.2a**, where a heterogeneously swollen fiber (1) and a uniformly swollen fiber (2) are shown. In **Figure 4.1.2b**, a single balloon region shows a clear Maltese cross. These features indicate that hierarchical fibrillar arrangements were still present within the swollen wall. The schematic representations in **Figure 4.1.2c–d** summarize the corresponding fiber wall interpretation, showing the native layered fiber wall structure and the proposed balloon-collar morphology after heterogeneous swelling.

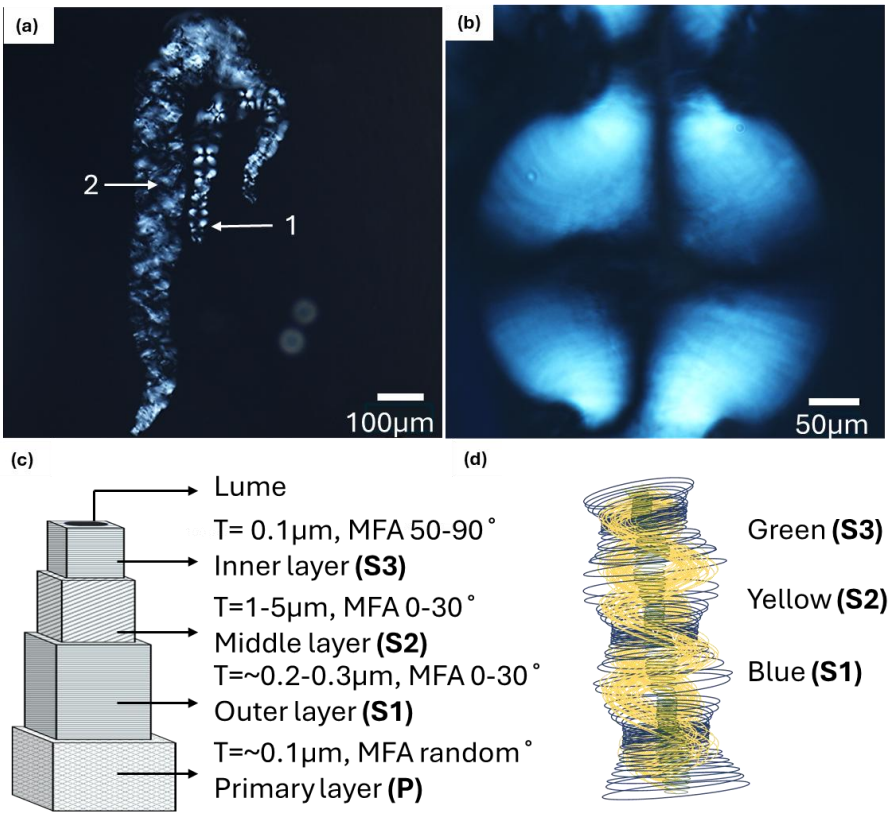


Figure 4.1.2: *(a) A heterogeneously swollen fiber (1) and a uniformly swollen fiber (2) in polarization mode; (b) High-magnification optical microscopy image of a single balloon in polarization mode; (c) A schematic illustration, not to scale, of the hierarchical structure of a native cellulose fiber; (d) A schematic of the lateral section image showing heterogeneous fiber swelling displaying balloon-collar structure. Adapted from Paper I* [48].

The balloon-collar morphology is consistent with previous descriptions of cellulose-rich fibers undergoing heterogeneous swelling or dissolution, where swelling of the thick S2 layer is constrained by the surrounding S1 layer [65, 67, 118]. It also fits the hierarchical fiber wall structure, where the thick S2 layer dominates swelling and mechanical response while the thinner S1 layer contributes to collar formation [18, 23, 29, 30].

These observations indicate that DALC modification amplifies heterogeneity at two levels: between fibers within a sample, and along individual fibers, where swollen balloons alternate with less-expanded collar regions. This heterogeneity may partly reflect the known natural variability in wood fiber structure, including earlywood/latewood differences, fiber wall thickness and microfibril angle [18, 123].

The fraction of imaged fiber area showing visible ballooning increased strongly with DOM, from approximately 10% in DALC-26DOM to approximately 55% in DALC-44DOM and 70% in DALC-51DOM. At the highest DOM, balloon-collar fibers coexisted with uniformly swollen fibers, suggesting a transition toward uniform swelling, plausibly as adjacent balloons expand and merge while collar regions swell, producing fibers that swell uniformly along their length. **Figure 4.1.2a** shows DALC-51DOM fibers with ballooning (1) and uniform swelling (2) in the same sample, supporting this transition. This interpretation is consistent with recent observations for highly modified DALC fibers and with earlier reports of ballooning in cellulose-rich fibers during solvent-induced swelling or dissolution or in highly charged cellulose fibers [33, 50, 118, 119, 124].

4.1.3 Lumen accessibility and internal water distribution from CLSM dual-labeling

CLSM with dual fluorescent labeling was used to visualize lumen changes that DIC and polarized light microscopy cannot resolve. Calcofluor (blue) labels the polysaccharide-rich cell wall. FITC-dextran (10 kDa, green) is a mobile water tracer. It fills the surrounding medium and any space inside the fiber that it can reach.

Figure 4.1.3 shows DIC images (a, d, g, j), the matching CLSM images (b, e, h, k), and the 3D z-stacks (c, f, i, l) of Kraft-0DOM, DALC-26DOM, DALC-44DOM, and DALC-51DOM fibers. In Kraft-0DOM fibers, the lumen shows a weak green signal (b). In DALC fibers, the green signal in the center of the fiber increases from DALC-26DOM to DALC-51DOM (e, h, k), as ballooning increases.

This suggests that dextran reaches the fiber interior more easily as DOM increases, so the lumen becomes more accessible in highly swollen DALC fibers. This DOM-dependent increase in FITC-dextran signal contrasts with the classical expectation that fiber wall swelling proceeds inward and reduces lumen size [20]. The CLSM results support ballooning-driven lumen expansion: swelling displaces S1 material to form collars and reduces S1 constraint across balloon regions, so the inner wall layers (S2/S3) may be pushed outward, expanding the lumen. The apparent lumen expansion at higher DOM is further discussed in **Paper I** as evidence that sufficient solvent is present within the lumen and that S3 contributes resistance under the swelling pressure.

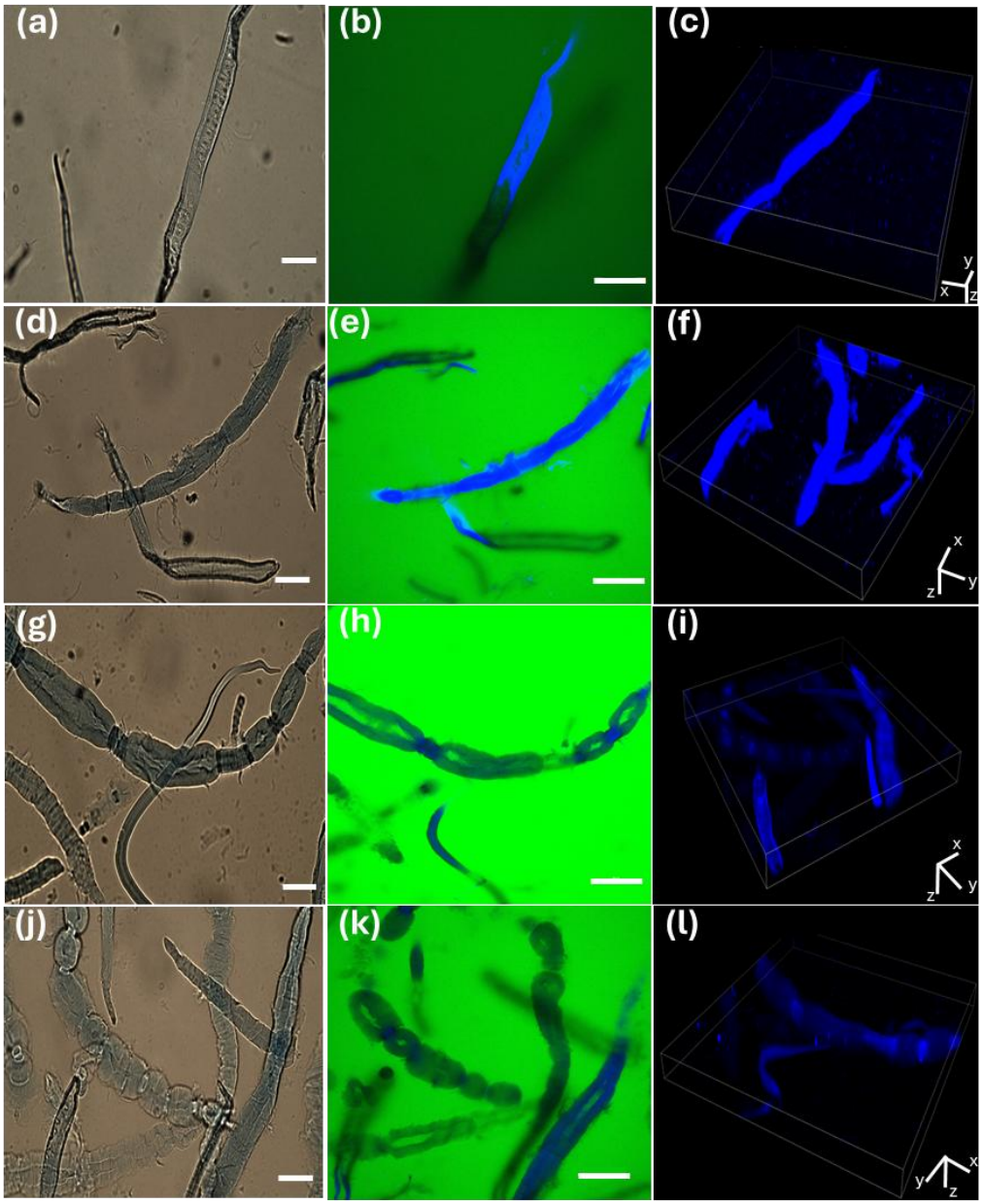


Figure 4.1.3: *DIC images of (a) Kraft-0DOM, (d) DALC-26DOM, (g) DALC-44DOM and (j) DALC-51DOM fibers. CLSM images of dual-fluorescent-labeled fibers are shown for (b) Kraft-0DOM, (e) DALC-26DOM, (h) DALC-44DOM and (k) DALC-51DOM. The corresponding CLSM 3D z-stacks are shown in (c), (f), (i) and (l), respectively. Calcofluor is shown in blue and FITC-dextran in green. Images within each row are shown in the same frame of reference for comparison. Scale bars correspond to 100 µm. Adapted from Paper I* [48].

4.1.4 Quantification of swelling by WRV and fiber width distributions

Swelling was quantified using WRV, reported as grams of water per gram of dry fiber (g/g), an indirect measure of fiber swelling propensity. Across the ND sample series, WRV increased monotonically with DOM, from ~1.7 g/g (Kraft-0DOM) to ~3.4 g/g (DALC-26DOM), ~4.9 g/g (DALC-44DOM), and ~6.3 g/g (DALC-51DOM) (**Figure 4.1.4a**).

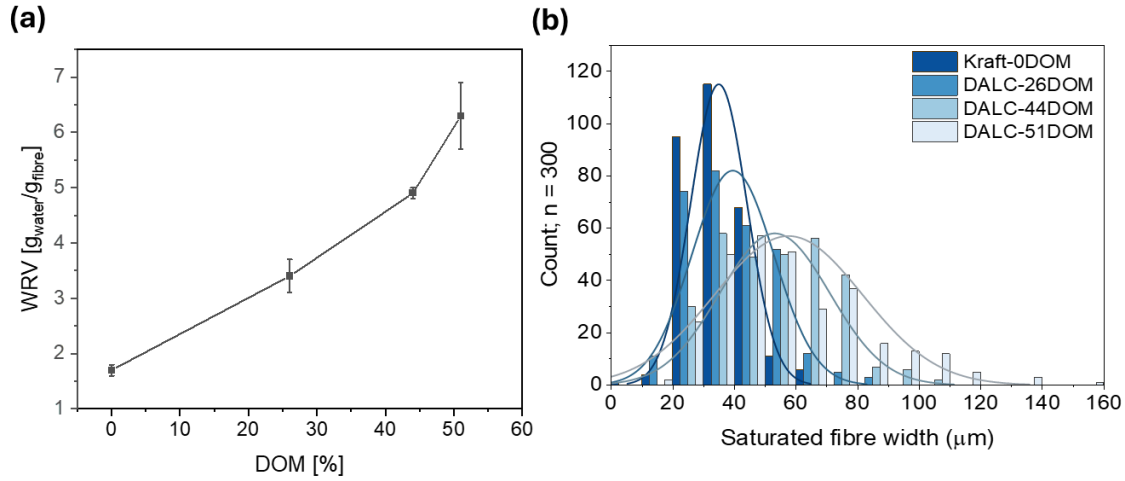


Figure 4.1.4: *(a) WRV values assessed for unmodified and modified fibers with DOM; (b) distribution of saturated fiber widths measured from DIC images of never-dried fibers (n = 300 measurements from 30 fibers per sample, including balloon and collar regions); solid lines are Gaussian fits. The WRV measurements were made in duplicate, and the error was calculated as (max–min)/2. Adapted from Paper I* [48].

The increase in WRV is consistent with earlier reports [119, 125], and the overall trend agrees with prior observations of increased WRV for DALC fibers [59]. Since WRV is sensitive to fines (smaller fragments of fibers), these fines were removed before analysis to improve comparability [126]. The monotonic WRV increase with DOM is consistent with increasing fiber wall swelling.

At the single-fiber level, width distributions broadened markedly with DOM. From DIC-based measurements (30 fibers; multiple points per fiber including balloons and collars), mean widths increased from 35 ± 9 µm (Kraft-0DOM) to 40 ± 14 µm (DALC-26DOM), 53 ± 18 µm (DALC-44DOM), and 58 ± 24 µm (DALC-51DOM) (**Figure 4.1.4b**). Importantly, the dominant effect is not only an increase in mean

width but a strong broadening of the width distribution, consistent with heterogeneous swelling along fibers and among fibers.

4.1.5 Effect of drying/rewetting: morphological 'memory' and inelastic deformation

Drying did not remove the balloon-collar shape of highly modified fibers (DALC-44DOM and DALC-51DOM, **Figure 4.1.5**). After rewetting, the balloons returned and the fibers appeared similar to the never-dried state at the microscopic level. Whether this recovery holds true at the nanoscale is addressed in **Section 4.2**. This behavior can be attributed to inelastic strain in the fiber wall, leaving a morphological "memory" of balloon-collar deformation.

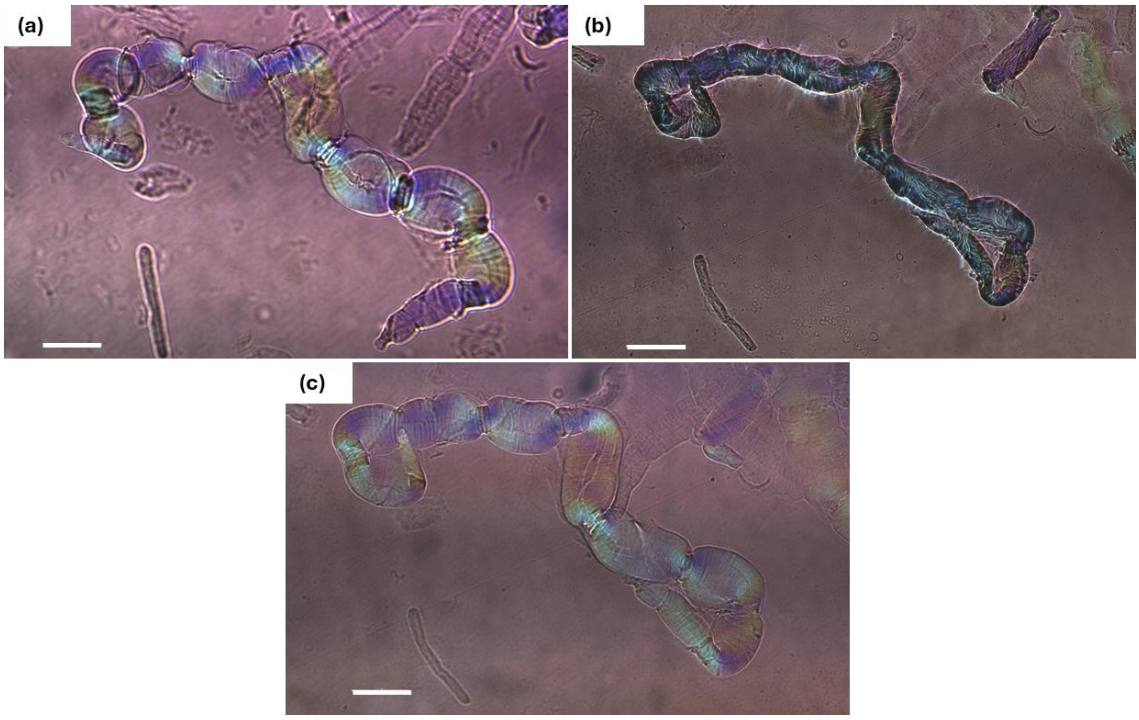


Figure 4.1.5: *DALC-51DOM fiber in the (a) ND, (b) BD and (c) RW states, imaged in the same field of view. Scale bar = 100 µm. Adapted from Paper I* [48].

4.1.6 Answer to RQ1

RQ1: How does increasing DALC modification affect fiber wall swelling, morphology, and water retention?

Increasing DALC modification increased fiber wall swelling. Water retention and fiber width both increased with DOM. Swelling first appeared as balloon-collar

morphology. At 51% DOM, balloon-collar and uniformly swollen fibers coexisted, indicating a transition toward uniform swelling. Light microscopy shows these morphological changes, but not the nanoscale fibrillar structure inside the fiber wall. Light microscopy shows the balloon-collar morphology returning after rewetting, but it cannot show whether the nanoscale fibrillar structure recovers as well. The next section therefore uses SAXS and WAXS to ask whether the recovery holds true at the nanoscale.

4.2 X-ray scattering: Ångström-to-nanometer structural response

This section addresses **RQ2** by examining how DALC modification and drying history change the fiber wall from Ångström-scale crystalline order to nanometer-scale fibrillar arrangement, and how these changes relate to macroscopic swelling.

Background: Earlier WAXS studies showed that crystallinity decreases as DOM increases [51, 58, 59, 69]. SAXS has been used to measure length scales in cellulose fibers [35, 127], and these length scales change with moisture [74]. Can SAXS detect the effect of DOM, drying history, and rewetting on DALC fibers at the nanoscale?

Hypothesis: Higher DOM was expected to lower crystallinity and increase the SAXS characteristic length. This length was expected to follow swelling, measured as WRV. Bench-dried fibers (BD) were expected to have a shorter characteristic length, while the rewetted fibers (RW) were expected to show a slightly smaller characteristic length than never-dried fibers (ND).

Approach: WAXS measured crystallinity and the (200) domain width. SAXS measured nanoscale arrangements in the fiber wall, using the Kratky-derived characteristic length, $\ell_k = 2\pi/q^*$, and the fitted correlation length, ξ, for wet samples. ℓ_k and ξ are compared across DOM and drying history and related to WRV.

4.2.1 WAXS: Increasing DOM reduces crystallinity and apparent crystallite width

Across all DOM, the WAXS patterns retain the cellulose Iβ scattering, indicating that DALC modification and drying and rewetting do not measurably change the underlying Iβ lattice; the changes appear primarily in relative peak intensities.

For the wet fibers (ND and RW), the water contribution produces a high background that complicates quantitative comparison of peak intensities. Therefore, crystallinity index and apparent crystallite width are evaluated from the bench-dried series.

In the bench-dried (BD) samples, the crystallinity index, calculated using the Segal peak-height method (**Equation 6**), decreased with increasing DOM (**Figure 4.2.1**). The crystallinity index decreased from 68% (Kraft-0DOM_BD) to 41% (DALC-51DOM_BD), with intermediate values for DALC-26DOM_BD (59%) and DALC-44DOM_BD (48%).

Peak deconvolution of the (200) peak with the Scherrer equation (**Equation 2**) showed a reduction in apparent crystallite width with increasing DOM (e.g., ~3.4 nm for Kraft-0DOM_BD and ~1.3 nm for DALC-51DOM_BD). These estimates are treated cautiously, since fitted widths can reflect peak overlap and disorder broadening as well as domain size; nonetheless, the monotonic decrease aligns with the crystallinity trend.

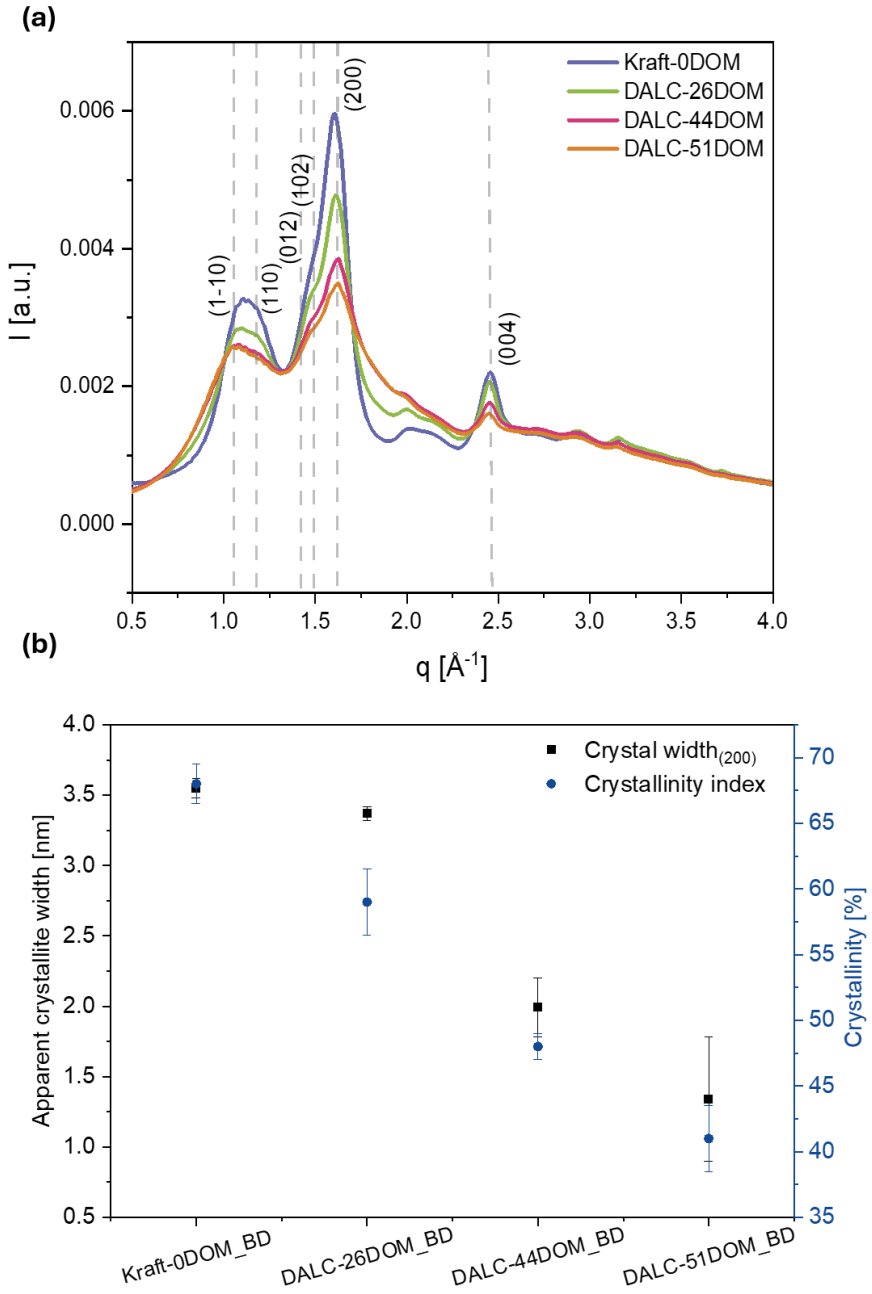


Figure 4.2.1: *(a) WAXS curves of BD fibers across the DOM series, showing the scattering intensity (normalized at q = 1.3 Å^{-1}) as a function of q; (b) average (200)-associated apparent crystallite width and average crystallinity estimated for the BD fibers. Error bars are half-ranges, (max − min)/2, from two independent sample preparations (n = 2). Replotted from data reported in Paper II.*

4.2.2 Model-independent Kratky analysis of characteristic nanoscale correlations

The Kratky-maximum position q* is extracted from the mid-SAXS regime (q* ≈ 0.03–0.18 $Å^{-1}$), corresponding to characteristic length scales of a few to about twenty nanometers (**Table 2**). The resulting characteristic length ℓ_k (**Equation 10**) is treated as a practical length scale for comparing samples, as it captures systematic changes in nanoscale arrangements in the fiber wall.

As the measured SAXS intensity still contains both form- and structure-factor contributions (**Equation 1**), the resulting length scale should be treated as an apparent characteristic length of the observed scattering feature. The SAXS curves for the ND, BD and RW fiber series are shown in **Figure 4.2.2**. These SAXS data are further plotted as Kratky plots of $I \cdot q^2$ versus q (**Supplementary Figures S11–S14 of Paper II**). The characteristic length, ℓ_k, is calculated from the position of the Kratky maximum (using **Equation 10**). ℓ_k was largest in ND fibers, slightly reduced in RW fibers as compared to ND fibers, and smallest in BD fibers (**Table 2**). This can be attributed to the drying-induced irreversibility that limits reopening of the aggregated nanostructure upon rewetting.

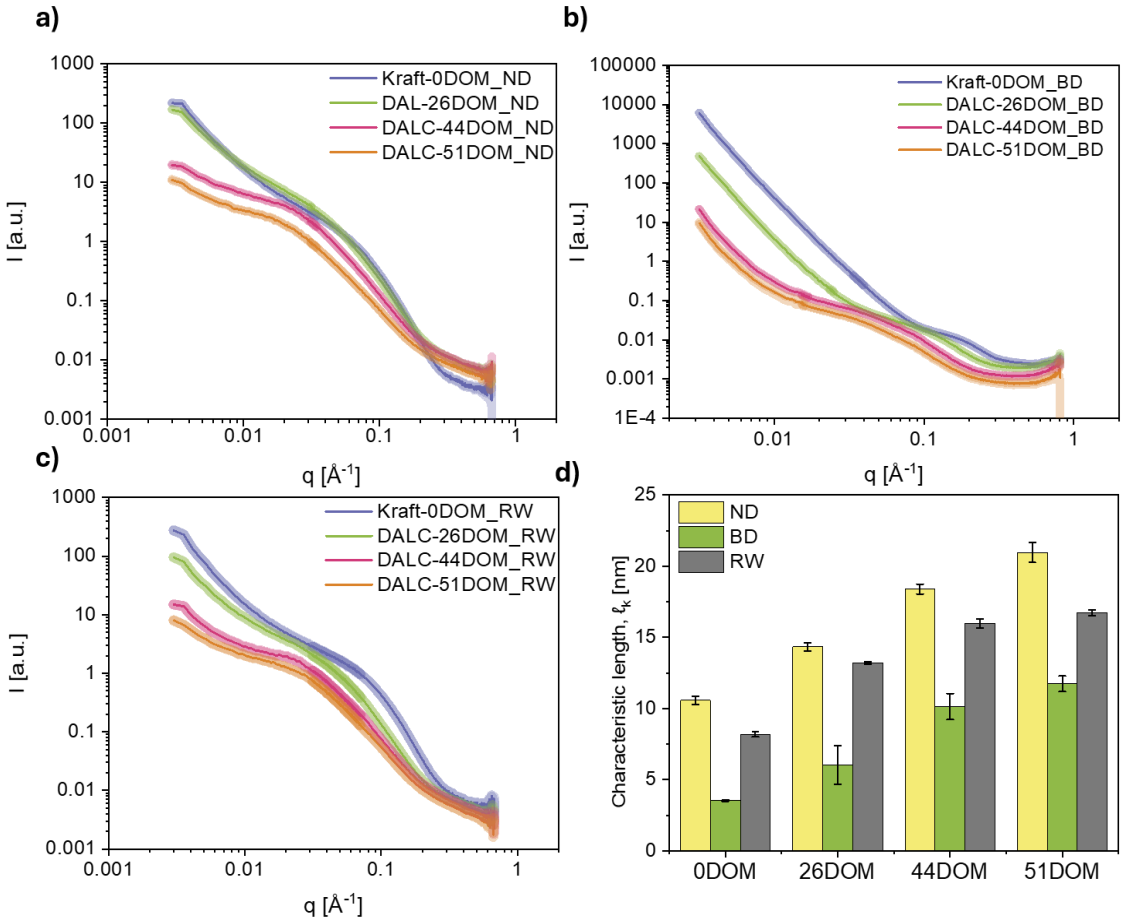


Figure 4.2.2: *SAXS curves showing the scattering intensity, I(q), as a function of q (logarithmic axes) for (a) ND fibers, (b) BD fibers, and (c) RW fibers across the Kraft-0DOM and DALC-xDOM (x = 26, 44, 51) series. The instrumental uncertainty d(I) is indicated by semi-transparent markers in the corresponding colors (hardly visible in the figures); (d) Kratky-derived characteristic length, ℓ_k, for the same fiber series and drying histories. Bars report mean values from three independently prepared measurements (n = 3); error bars represent the corresponding standard deviation. Adapted from Paper II.*

Table 2: *Kratky-derived characteristic length (ℓ_k) for ND, BD, and RW fiber samples. Values are mean ± standard deviation (n = 3 independently prepared samples).*

ND sample	q^* (Å^{-1})	ℓ_k (nm)	BD samples	q^* (Å^{-1})	ℓ_k (nm)	RW samples	q^* (Å^{-1})	ℓ_k (nm)
Kraft-0DOM_ND	0.0598 ± 0.0018	**10.6 ± 0.3**	Kraft-0DOM_BD	0.1780 ± 0.0021	**3.5 ± 0.1**	Kraft-0DOM_RW	0.0767 ± 0.0010	**8.2 ± 0.2**
DALC-26DOM_ND	0.0439 ± 0.0004	**14.3 ± 0.2**	DALC-26DOM_BD	0.1071 ± 0.0196	**6.0 ± 1.3**	DALC-26DOM_RW	0.0474 ± 0.0003	**13.2 ± 0.1**
DALC-44DOM_ND	0.0337 ± 0.0004	**18.4 ± 0.3**	DALC-44DOM_BD	0.0659 ± 0.0055	**10.1 ± 0.9**	DALC-44DOM_RW	0.0401 ± 0.0011	**15.9 ± 0.3**
DALC-51DOM_ND	0.0300 ± 0.0010	**21.0 ± 0.7**	DALC-51DOM_BD	0.0560 ± 0.0031	**11.7 ± 0.6**	DALC-51DOM_RW	0.0376 ± 0.0005	**16.7 ± 0.2**

The characteristic lengths ℓ_k from the Kratky maximum can be assumed to represent predominantly the structure factor S(q) when the form factor P(q) remains constant. However, the WAXS analyses indicate that the apparent crystallite size decreases with increasing DOM, which means the form factor is not constant across the modification series. The SAXS data were therefore also fitted with model-based approaches.

4.2.3 Peak fitting of SAXS data: Model-based approach

For the wet fiber conditions (ND and RW), an empirical network model was employed to describe the broad correlation feature of the swollen fibrillar network. For the BD condition, the WoodSAS model was applied to obtain physical descriptors of the nanostructure within the fiber wall.

4.2.3.a Empirical network model for wet samples

The empirical network model **(Equation 11**) closely represents the swollen and disordered nanofibrillar networks of the hydrated fibers 116. The model assumes that the hydrated fiber wall behaves like a disordered fibrillar network with a

dominant correlation length superimposed on large-scale power-law scattering. The fitted correlation length (ξ) is interpreted as a network length scale reflecting interfibrillar arrangements within the fiber wall. ξ follows the same trend as ℓ_k. A larger ξ suggests a more open network, and a smaller ξ indicates compact fibrillar arrangements. The empirical network-model fits are shown in **Figure 3 of Paper II**, supporting the use of the fitted ξ as a complementary model-dependent descriptor of DOM-dependent changes in the hydrated fibrillar network.

As shown in **Table 3**, ξ increased and n decreased with DOM in both series. In ND fibers, ξ increased from 1.66 ± 0.02 nm (Kraft-0DOM) to 4.15 ± 0.07 nm (DALC-51DOM), while n decreased from 2.59 to 1.98, indicating a more open, less dense fibrillar network.

RW fibers followed the same trend as ND fibers, with ξ increasing from 1.35 ± 0.01 nm (Kraft-0DOM) to 3.21 ± 0.04 nm (DALC-51DOM). However, the RW values stayed below the ND values, indicating that rewetting only partially restores the structural arrangements of nanofibrils, which is consistent with hornification.

Table 3: *Empirical-network-model fitting parameters for the SAXS profiles of wet ND and RW fibers.*

Sample	A ×10^{-4}	n	C (cm^{-1})	ξ (nm)	m	R²
Kraft-0DOM_ND	1.9 ± 0.4	**2.59 ± 0.04**	4.17 ± 0.14	**1.66 ± 0.02**	4.08 ± 0.06	0.991
DALC-26DOM_ND	1.3 ± 0.2	**2.46 ± 0.03**	3.83 ± 0.15	**2.44 ± 0.04**	3.59 ± 0.05	0.996
DALC-44DOM_ND	0.7 ± 0.2	**2.14 ± 0.06**	3.86 ± 0.11	**3.50 ± 0.04**	3.03 ± 0.03	0.998
DALC-51DOM_ND	0.9 ± 0.3	**1.98 ± 0.05**	2.45 ± 0.09	**4.15 ± 0.07**	2.72 ± 0.03	0.998
Kraft-0DOM_RW	0.85 ± 0.17	**2.61 ± 0.04**	1.73 ± 0.04	**1.349 ± 0.013**	4.31 ± 0.05	0.992
DALC-26DOM_RW	0.86 ± 0.13	**2.43 ± 0.03**	1.95 ± 0.06	**2.22 ± 0.03**	3.67 ± 0.04	0.996
DALC-44DOM_RW	2.24 ± 0.18	**1.922 ± 0.014**	1.44 ± 0.04	**2.73 ± 0.04**	3.30 ± 0.03	0.997
DALC-51DOM_RW	2.08 ± 0.17	**1.793 ± 0.014**	1.26 ± 0.03	**3.21 ± 0.04**	3.01 ± 0.03	0.998

Fit q range: 0.003–0.7 Å^{-1}; weighted by dI.

ξ and ℓ_k changed in the same direction. Their values differ because the two lengths are defined differently. However, both results show that higher DOM expands the hydrated fibrillar network. **Figure 4.2.3** shows a clear positive relationship between the model-based correlation length (ξ) and the Kratky-derived characteristic length (ℓ_k) for both ND and RW fibers, supporting the conclusion that the two independent descriptors capture the same DOM-dependent trend. Although ξ is systematically smaller than ℓ_k, this offset is expected, since ξ comes from a model-dependent fit of the network-correlation term whereas ℓ_k is an apparent length from the Kratky maximum.

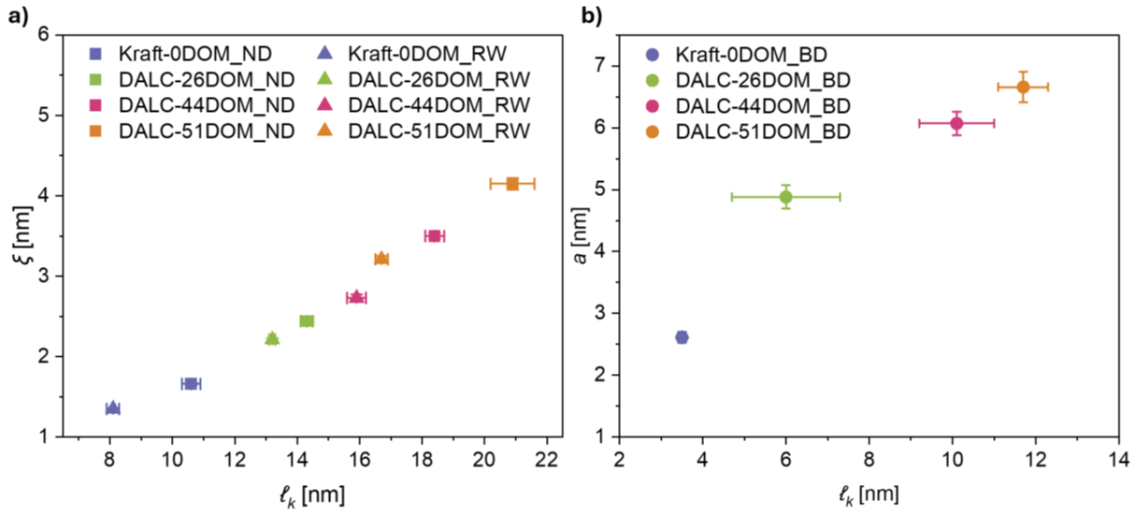


Figure 4.2.3: *Relationship between the empirical network-model correlation length, (ξ), and the Kratky-derived characteristic length, (ℓ_k), for wet-state ND and RW fiber samples. Both descriptors increase with DOM and show comparable drying-history-dependent trends, with RW samples remaining below the corresponding ND values. Adapted from Paper II.*

To estimate the form- and structure-factor contributions across the DOM series, the WoodSAS model was applied to the dry samples.

4.2.3.b WoodSAS model for dry samples

The WoodSAS model (**Equation 12**) was applied to the SAXS profiles to obtain physical descriptors of the fiber wall nanostructure for the BD fiber series. The model treats cellulose nanofibrils as infinitely long cylinders in laterally correlated, paracrystalline packing, decomposing the SAXS feature into nanofibril dimensions, interfibrillar spacing, and packing disorder.

WoodSAS model fits are given in **Supplementary Figure S17 of Paper II**. The fitting indicated a gradual increase in the apparent cylinder diameter, (2R), with increasing DOM (**Equation 12**). The fitted (2R) values increased from 2.19 ± 0.12 nm (Kraft-0DOM) to 2.75 ± 0.18 nm (DALC-51DOM) across the DOM series. A more pronounced change was observed for the fitted center-to-center packing distance, (a), which increased from 2.61 ± 0.09 nm in Kraft-0DOM to 6.7 ± 0.3 nm in DALC-51DOM. The largest increase occurred between Kraft-0DOM and DALC-26DOM, followed by a further but smaller increase at higher DOM. These results suggest that DALC modification primarily affected the spacing between nanofibril-associated scattering domains, while the apparent cylinder diameter changed less. This indicates that the structure factor S(q) dominates the SAXS curves of the DALC fibers, while the form factor P(q), although present, contributes less.

The increase in 2R contrasts with the decrease in the WAXS-derived apparent crystallite width (**Section 4.2.1**), but the two quantities describe different features. WAXS measures the width of the crystalline domain perpendicular to the (200) planes, whereas the WoodSAS diameter describes the cross-section of the scattering object, defined by electron-density contrast with the surrounding voids. That object may also include less-ordered fibril surfaces and associated ring-opened-material. Because the two rest on different contrast mechanisms and model assumptions, their absolute values are not directly comparable; for Kraft-0DOM, the WAXS width (~3.4 nm) even exceeds the fitted 2R (2.19 nm). The opposite trends are, however, qualitatively consistent with DALC modification acting preferentially at accessible fibril surfaces and less-ordered regions: ring opening reduces the ordered crystalline core while the overall scattering object remains similar in size or grows slightly. This interpretation should be treated with caution, since the change in 2R is small compared with the change in ‘a’ from **Equation 12**, and ΔR/R reached its fitting limit for DALC-44DOM and DALC-51DOM (**Table 4**).

Table 4: *WoodSAS-derived SAXS fitting parameters[a] for the bench-dried (BD) fibers.*

Sample	A	2R (nm)	ΔR/R	a (nm)	Δa/a	B	σ / 10^{-2} Å^{-1}	C	α	χ^2/N
Kraft-0DOM_BD	0.081 ± 0.010	**2.19 ± 0.12**	0.30 ± 0.05	**2.61 ± 0.09**	0.431 ± 0.014	0.339 ± 0.014	2.42 ± 0.03	(1.302 ± 0.018) × 10^{-6}	3.973 ± 0.003	3.83
DALC-26DOM_BD	0.040 ± 0.005	**2.31 ± 0.16**	0.30 ± 0.07	**4.88 ± 0.19**	0.53 ± 0.03	0.097 ± 0.005	4.61 ± 0.13	(1.75 ± 0.09) × 10^{-7}	3.762 ± 0.012	1.46
DALC-44DOM_BD	0.053 ± 0.013	**2.60 ± 0.02**	0.42[b]	**6.07 ± 0.19**	0.44 ± 0.02	0.312 ± 0.007	3.36 ± 0.06	(6 ± 2) × 10^{-7}	3[b]	1.77
DALC-51DOM_BD	0.036 ± 0.004	**2.75 ± 0.18**	0.43[b]	**6.7 ± 0.3**	0.61 ± 0.16	0.152 ± 0.006	3.14 ± 0.10	(7 ± 3) × 10^{-5}	1.97 ± 0.08	1.66

[a] Parameters as defined in **Equation 12**. Fit *q* range = 0.00142–0.335 Å^{-1}.

[b] Parameter reached its fitting limit; the associated uncertainty is not meaningful.

WoodSAS was also tested on the never-dried (ND) and rewetted (RW) samples, but the fits were not reliable. They gave a negative background for Kraft-0DOM_ND. For several samples, the uncertainty in Δa/a was larger than the fitted value. The fitted disorder was so high that no positional order remained. The RW packing distance also exceeded the ND value, which reverses the order from ℓ_k and ξ. These parameters are therefore not interpreted. WoodSAS assumes cylinders on a regular lattice. A swollen wet wall probably has no such lattice, but this was not tested here.

4.2.4 Linking WRV to nanoscale descriptors across modification levels and drying histories

Macroscopic swelling propensity of the fibers, quantified by WRV, increased monotonically with DOM (**Figure 4.2.4**). The same monotonic increase was observed for the Kratky-derived length (ℓ_k) and the network-model correlation length (ξ) in the ND fibers, indicating that increasing DALC modification is accompanied by progressive nanoscale expansion of the fiber wall.

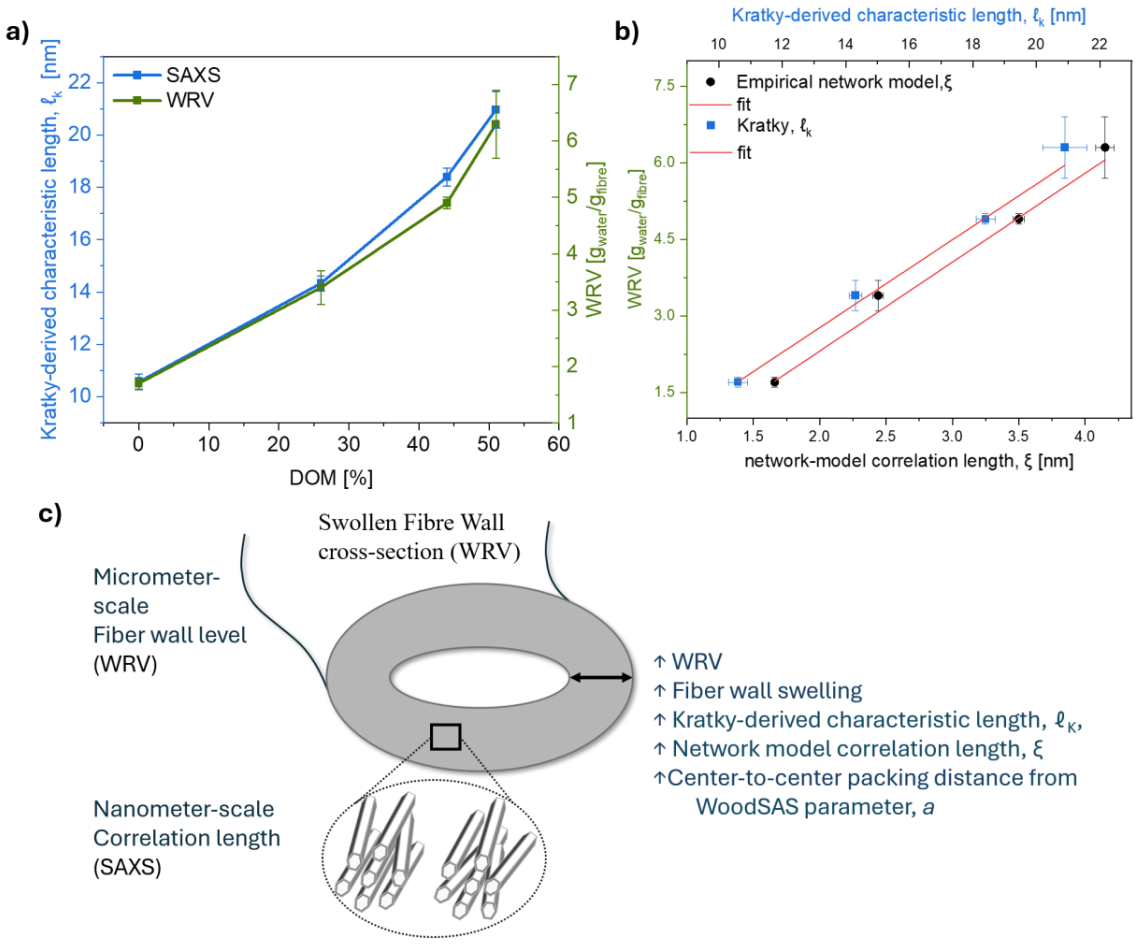


Figure 4.2.4: *(a) Variation in WRV and the Kratky-derived characteristic length, ℓ_k, as a function of increasing DOM for the ND fiber samples; (b) WRV plotted against ℓ_k (blue) and ξ (black); (c) Schematic illustrating swelling across length scales, linking fiber wall expansion (µm scale; WRV) to DOM-dependent changes in nanoscale arrangement captured by ℓ_k (nm scale), alongside the concurrent reduction in Å-scale crystalline order inferred from WAXS. Adapted from Paper II.*

4.2.5 Answer to RQ2

RQ2: How do DALC modification and drying history alter nanoscale fiber wall arrangement, and how do these relate to macroscopic swelling?

WAXS showed that the cellulose Iβ structure was retained, but crystallinity decreased with DALC modification. SAXS showed that ℓ_k increased with DOM. In wet fibers, ξ also increased and n decreased, indicating a less dense, more open fibrillar network. Drying reduced these lengths, and rewetting did not restore the swelling completely as ND fibers. This may be a sign of hornification. The

morphological recovery seen by light microscopy therefore does not fully hold at the nanoscale. In never-dried fibers, WRV increased together with ℓ_k and ξ, linking nanoscale arrangement to macroscopic swelling. Because WRV was measured only on never-dried fibers, this link is established for the never-dried state only.

Building on this nanoscale structural understanding, this section turns to fiber and sheet surfaces, examining how modification and pulp processing translate into surface-accessible chemical fingerprints using ToF-SIMS and multivariate analysis.

4.3 ToF-SIMS surface fingerprinting of Kraft fiber handsheets

This section addresses **RQ3** by developing a ToF-SIMS–chemometrics workflow for softwood Kraft fiber handsheets. The aim is to separate lignin- and polysaccharide-associated ion patterns. The workflow also handles fragment overlaps, matrix effects, adducts, and contaminants.

Background: Early ToF-SIMS work identified lignin ions using isolated and synthetic lignin [128-130]. Later studies extended this to wood and pulps [83, 85, 91]. Salt adducts [131] and isobaric overlap [91] are known to interfere with peak assignments. The primary aim was to establish a practical workflow for distinguishing polysaccharide- and lignin-associated ion patterns at chemically heterogeneous softwood Kraft handsheet surfaces.

Hypothesis: Compacted reference samples, pairwise PCA, and conservative peak screening can separate lignin- and polysaccharide-associated ions on Kraft handsheets.

Approach: The analysis combined compacted reference samples (MCC, GGM, xylan, SKPL), TIC-normalized spectra from six positions per sample, and pairwise PCA models, each isolating one chemical contrast. Marker ions were screened for isobaric overlap, salt adducts, and contaminants.

4.3.1 Workflow overview: compacted reference surfaces and pairwise PCA rationale

ToF-SIMS analysis of fiber handsheets is complicated by matrix- and topography-dependent ion yields on rough, chemically mixed fiber-network surfaces [83, 90, 91]. To provide stable chemical benchmarks, powdered reference samples such as MCC,

GGM, xylan, and SKPL were compacted into flat surfaces for a conservative screening approach to minimize false-positive assignments, whereas handsheets represented the realistic heterogeneous substrates to which the workflow was applied.

All spectra were TIC-normalized to mitigate differences in overall secondary-ion yield between measurements. Targeted two-class PCA models were used to link dominant variance to defined contrasts (e.g., lignin- vs carbohydrate-associated fragments; cellulose- vs hemicellulose-associated fragments), summarized in **Table 5**. The marker ions were retained only when reproducible across six replicate spectra, consistent with the reference-supported assignment, and after screening out peaks dominated by contaminants or salt/adduct contributions [91, 131].

Table 5: *Pairwise PCA models on different sample combinations and their chemical interpretation.*

PCA model	Sample comparison	Chemical interpretation from PCA separation
PCA1	Unbleached vs bleached handsheets	Used to assess whether bleaching altered the relative contributions of lignin-associated and carbohydrate-associated ions at handsheet surfaces.
PCA2	MCC vs SKPL	Used to assess the contrast between cellulose-associated and lignin-associated fragment ions using simplified reference samples.
PCA3	MCC vs GGM	Used to examine GGM-associated fragment ions relative to the dominant glucose-derived fragments of cellulose.
PCA4	MCC vs xylan	Used to examine fragment ions associated with pentose-rich xylan relative to cellulose.
PCA5	Unbleached handsheet vs SKPL	Used to assess which polysaccharide-associated fragment ions remain distinguishable in the unbleached handsheet despite the presence of residual lignin shared with SKPL.
PCA6	Bleached handsheet vs MCC	Used to assess which non-cellulosic fragment ions remain distinguishable at the bleached handsheet surface relative to cellulose-rich MCC.
PCA7	Bleached handsheet vs GGM	Used to examine hemicellulose-associated fragment ions within the predominantly cellulose-associated bleached handsheet surface.
PCA8	Unbleached handsheet vs GGM	Used to examine which hemicellulose-associated fragment ions remain detectable when GGM-related signals are embedded within the lignin-containing unbleached handsheet surface.

4.3.2 Reference vs handsheet spectra: effects of surface topography and achievable mass resolution

The main preparation-dependent difference was the surface presented to the ion beam: handsheets were rough, topographically non-uniform fiber networks, whereas the compacted references formed flat, continuous surfaces. This matters because topography affects ion extraction, spectral reproducibility and attainable mass resolution. The surface morphology of the compacted MCC, GGM, SKPL and xylan references together with the unbleached and bleached handsheets is shown in **Figure 1 of Paper III**. The comparison of mass resolution at *m/z* 163^+ for different sample topographies (powdered, compacted powdered and handsheets) is shown in **Supplementary Figure S2 of Paper III**. These topography-driven effects are reflected directly in the spectral quality and data interpretability. In spectroscopy mode, the compacted reference samples achieved substantially higher mass resolution ($m/\Delta m \geq 6000$ at *m/z* 200) than the handsheets ($m/\Delta m \geq 2000$ for the unbleached handsheet and ≥ 1700 for the bleached handsheet). Consequently, the reference spectra provide cleaner chemical benchmarks for evaluating candidate marker ions and assessing isobaric overlaps, while the handsheet spectra represent the more realistic, chemically mixed case.

Individual fragment peaks were generally less distinct in the fiber handsheets than in the compacted references, so direct interpretation of TIC-normalized peak heights is insufficient on its own. The subsequent analysis uses replicate-based statistics, reference-supported assignments, and pairwise PCA to avoid overinterpreting single-spectrum intensity differences. Representative spectra for each sample type are shown in **Figure 1 of Paper III and Supplementary Figure S3**.

4.3.3 Interferences and matrix effects: contaminants, salt/adduct contributions, and conservative peak screening

The PCA model comparing unbleached and bleached fiber handsheets showed tight replicate clustering and clear separation along PC1, which accounted for 78% of the variance (**Figure 4.3.1a**). The corresponding loading plot (**Figure 4.3.1b**) identified the ions contributing most strongly to this surface-chemical contrast. Guaiacyl lignin-associated fragments, *including m/z 137⁺ and 151⁺, were higher* in the unbleached handsheet, whereas carbohydrate-associated fragments, including *m/z* 85^+, 97^+, 127^+, 133^+ and 145^+, loaded with the bleached handsheet. The assignments of *m/z* 137^+ and 151^+ as guaiacyl lignin-associated ions are consistent with previous ToF-SIMS studies of lignocellulosic materials, while *m/z* 115^+ was treated cautiously because it can include both lignin- and carbohydrate-derived contributions [83, 85, 89, 128, 132, 133]. This pattern is consistent with a bleaching-related decrease in the relative contribution of lignin-associated surface chemistry, accompanied by an increased relative contribution of carbohydrate-associated ion signals, in agreement with earlier surface analyses of Kraft pulps showing reduced apparent surface lignin after bleaching [25, 26]. However, the same loading also contained contaminant and unresolved peaks, showing that high loading weight alone is not sufficient for marker assignment on chemically complex surfaces.

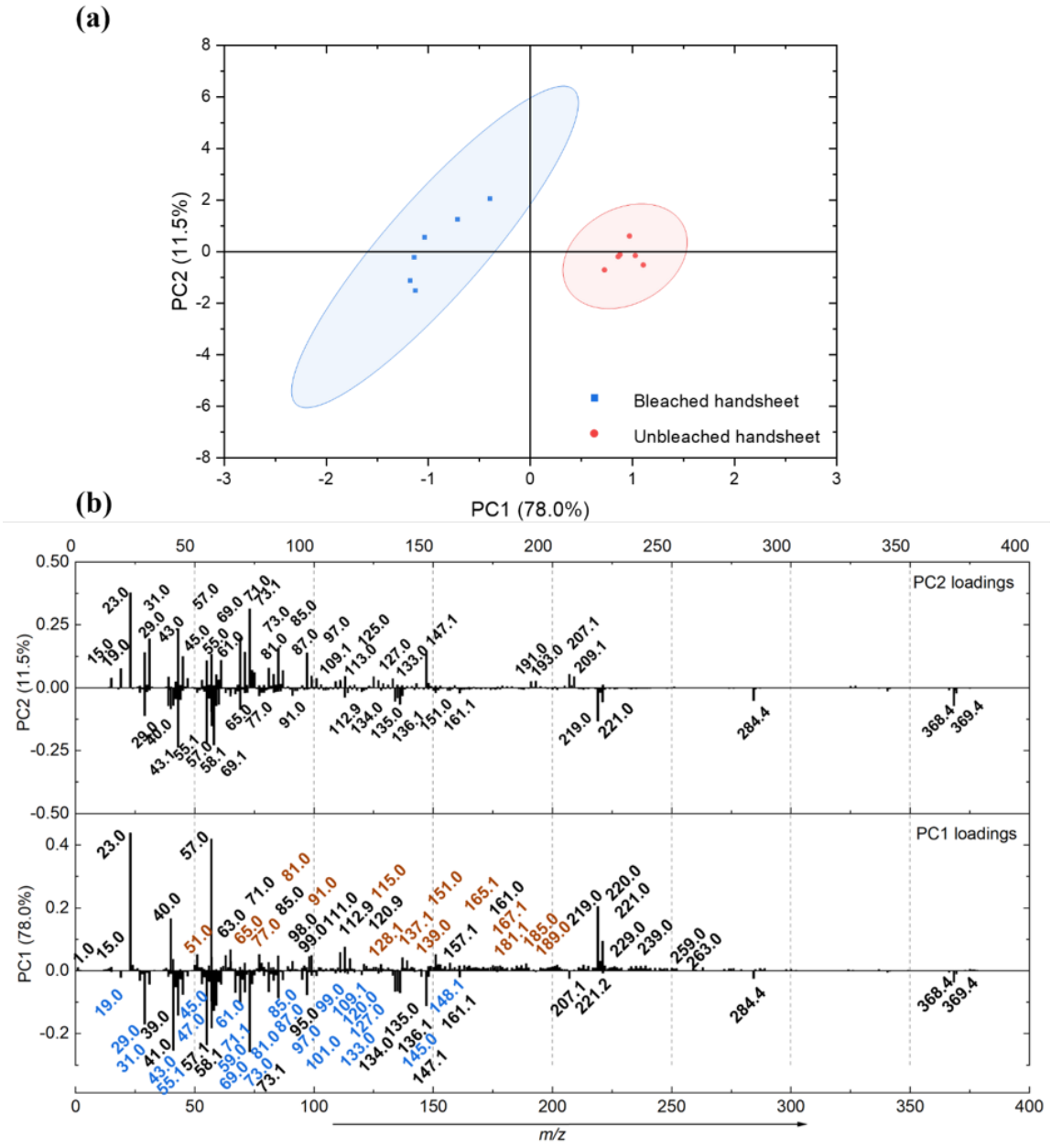


Figure 4.3.1: *(a) PCA score plot with 95% confidence ellipses for ToF-SIMS spectra from unbleached (red) and bleached (blue) softwood Kraft fiber handsheets; (b) corresponding PC1 loading plot, displayed up to m/z 400. Orange labels indicate lignin-associated fragments, blue labels indicate polysaccharide-associated fragments, and black labels indicate common contaminants or unresolved fragments. Adapted from Paper III* [63].

The marker-ion assignments should be interpreted within the known constraints of ToF-SIMS. Trace contamination, adduct formation and matrix-dependent ion

yields were considered explicitly because they can bias marker-ion interpretation in surface-sensitive ToF-SIMS analysis [91, 94]. This matrix dependence reflects the ionization-probability term '$\alpha^{\pm}$' in **Equation 3**. PDMS-related peaks, unresolved signals observed mainly in the bleached handsheets, inorganic ions such as Na^+ and Ca^+, and possible sodium- or phosphate-containing fragments were therefore treated cautiously and excluded from primary chemical interpretation when they lacked reference support or consistent PCA separation [82, 85, 86, 89, 130, 131, 134, 135]. To reduce overinterpretation, each peak was integrated within a narrow mass window (±0.03 u) and TIC-normalized, and only peaks with S/N ≥ 10 were kept. Marker ions also had to be consistent across six replicate measurements, agree with the compacted reference spectra, and contribute to the pairwise PCA models. Ambiguous ions, including known isobaric cases such as *m/z* 115^+, were excluded from the marker set or treated only as conditionally assigned. The final tentative assignments are given in **Table 3 of Paper III**.

4.3.4 Semi-quantitative comparison of bleached vs unbleached handsheets using validated marker ions

Following marker-ion validation through the pairwise PCA, the bleached and unbleached fiber handsheets were compared using TIC-normalized abundances of the retained lignin- and polysaccharide-associated fragments (n = 6). The resulting distributions are presented as violin plots (**Figure 4.3.2**), in which each marker ion is visualized as a reproducible contribution to the total detected ion population rather than as an isolated peak height from a single spectrum. Intensity differences between replicates show how the surface chemistry changes with delignification and bleaching. The comparison is semi-quantitative: matrix effects and fragment overlap can still change ion intensities, so the data show trends and not exact amounts [91, 94].

The most pronounced differences were observed for the lignin-associated ions *m/z* 137^+ and 151^+, which were approximately four times higher in the unbleached handsheets (unbleached/bleached ratios of 4.03 and 4.01, respectively; **Table 6**). This trend is consistent with greater exposure of guaiacyl lignin-associated chemistry before bleaching [83, 85, 128, 133, 136]. The cellulose-associated ions at *m/z* 127^+ and 145^+ showed ratios below unity (0.76 and 0.75), indicating a higher relative contribution of cellulose-associated fragments at the bleached fiber surface.

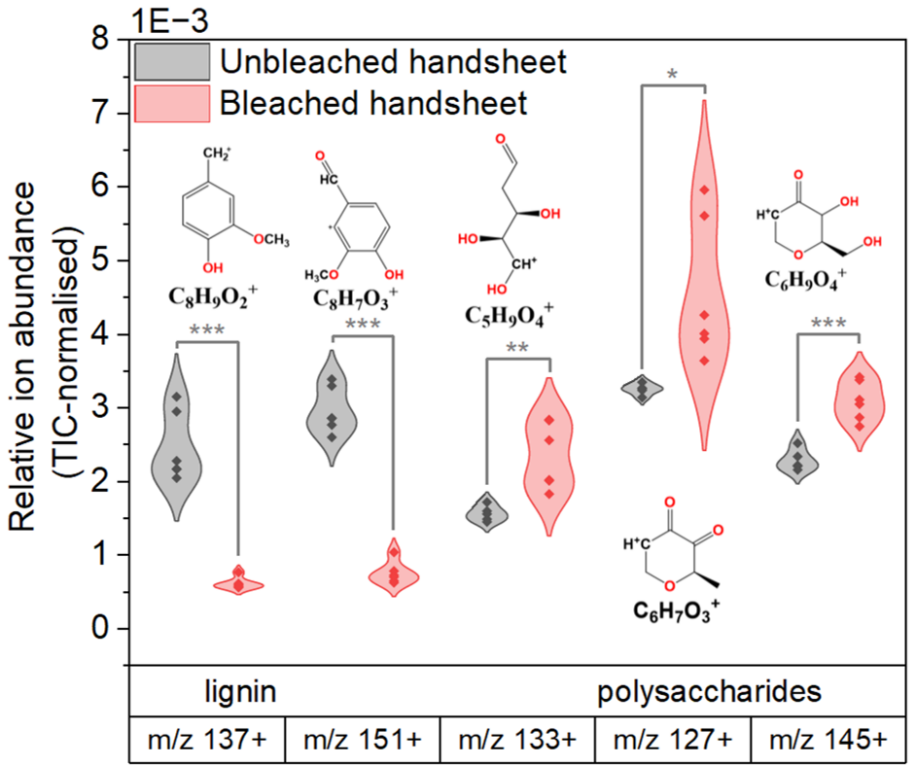


Figure 4.3.2: *Violin-box plot of the fragment ion abundance profiles in unbleached and bleached handsheets. (Statistical significance was determined using Welch's t-test (n = 6). Asterisks indicate significance levels: *** p < 0.001, ** p < 0.01, and * p < 0.05). Adapted from Paper III* [63].

Hemicellulose-associated signals required more careful interpretation. The isobaric ion *m/z* 115$^+$ can contain both lignin-derived $C_9H_7^+$ (115.0542 u) and polysaccharide-derived $C_5H_7O_3^+$ (115.0390 u) contributions [83, 85, 89, 132]. Their masses differ by 0.015 u, which is narrower than the peak width on the handsheets (m/Δm ≥ 2000), so the two cannot be separated. In contrast, *m/z* 133$^+$ (polysaccharide-derived contributions) showed a lower unbleached/bleached ratio (0.69), supporting increased relative exposure of hemicellulose-associated structures after lignin removal. This interpretation is consistent with earlier X-ray photoelectron spectroscopy/electron spectroscopy for chemical analysis (XPS/ESCA) studies reporting bleaching-related decreases in apparent surface lignin and a more carbohydrate-rich surface character in Kraft pulps, while the present ToF-SIMS data should be understood as relative fragment-ion trends rather than absolute surface coverages [25, 26].

Table 6: *Relative intensity ratios of validated marker ions for unbleached versus bleached handsheets.*

Peak (*m/z*)	Assignment	$Ratio = \frac{I_{unbleached\ handsheet}}{I_{Bleached\ handsheet}}$
137^+	Lignin	4.03 (1.03)
151^+	Lignin	4.01 (0.89)
133^+	Hemicellulose	0.69 (0.12)
127^+	Cellulose	0.76 (0.16)
145^+	Cellulose	0.75 (0.08)

Values in brackets are the standard error from 6 measurements.

4.3.5 Spatial mapping by 2D ToF-SIMS: heterogeneity and marker-ion localization

The 2D ToF-SIMS images provided spatial support for the trends observed in the spectra and PCA models. The lignin-associated ions *m/z* 137^+ ($C_8H_9O_2^+$) and *m/z* 151^+ ($C_8H_7O_3^+$) were stronger and more broadly distributed in the unbleached handsheet (**Figure 4.3.3**), consistent with residual lignin being present across the analyzed fiber surfaces rather than only in isolated spots.

The ion images agree with the spectral ratios (**Table 6**)**.** The lignin-associated ions *m/z* 137^+ and 151^+ were distributed across the unbleached handsheet but were weak in the bleached handsheet (**Figure 4.3.3b, c, e, f**). In the bleached handsheet, polysaccharide-associated ions were prominent, particularly the hemicellulose-associated ion *m/z* 133^+ (**Figure 4.3.3g, j**). The cellulose-associated ion *m/z* 127^+ was visible in both samples, while *m/z* 145^+ was less visible, which may reflect matrix-dependent suppression of oxygen-rich carbohydrate fragments in lignin-richer regions. Lignin forms stable aromatic positive ions, such as *m/z* 137^+ and 151^+, which may compete for charge during ionization and lower the yield of carbohydrate fragments nearby. Bright spots that appear at the same position in several ion images are likely due to topography or local particles rather than chemistry. The total-ion image was interpreted cautiously, because PDMS-related contamination added to the total counts, so the interpretation relies on the marker-ion images. The images are qualitative and show one representative area per sample.

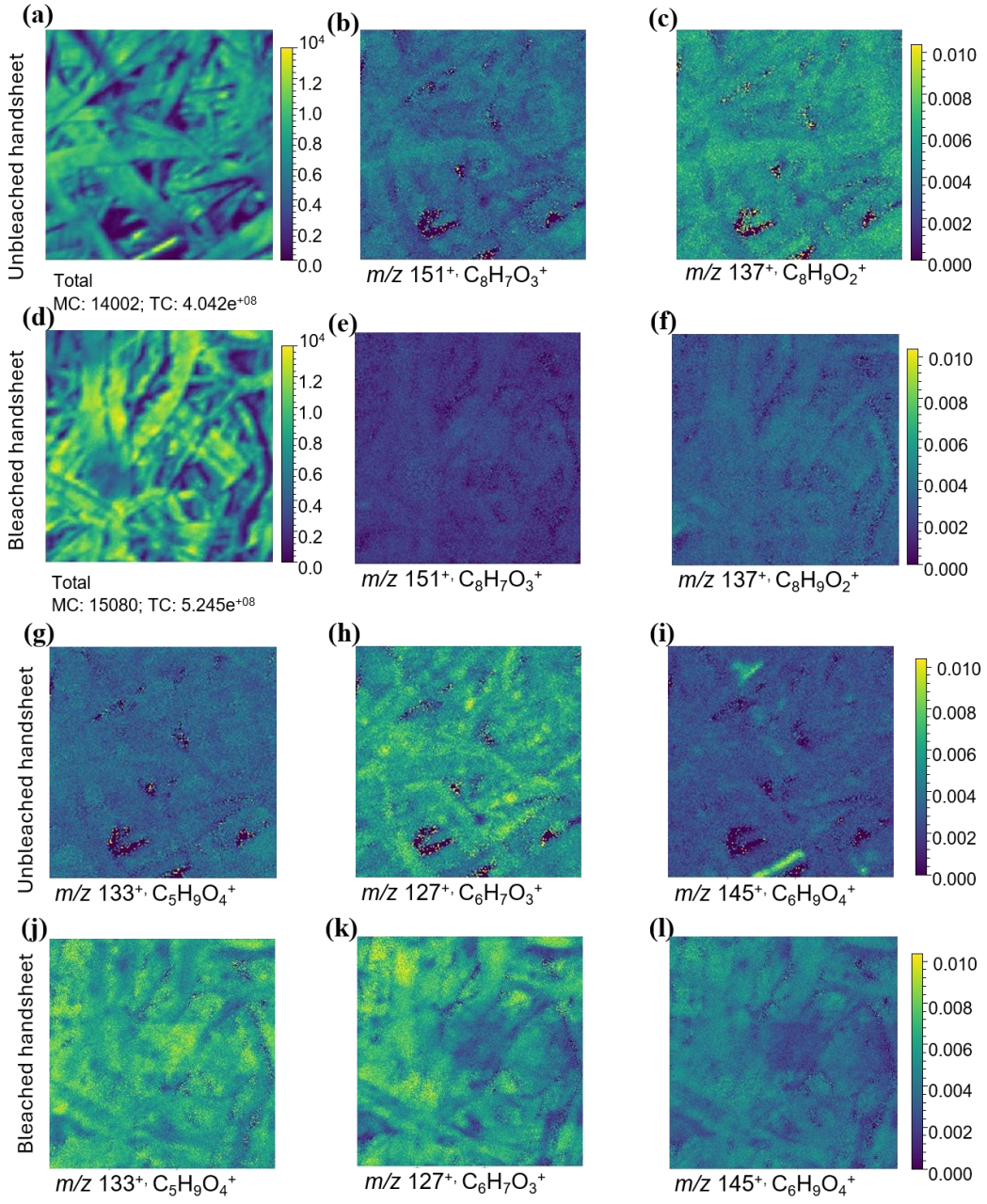


Figure 4.3.3: *Representative ToF-SIMS ion images of USK and BSK handsheet surfaces illustrating the spatial distributions of selected lignin- and polysaccharide-associated marker ions. The first and second rows show unbleached and bleached handsheets, respectively. Images a and d show total-ion-count images; b, c, e and f show lignin-associated ions; and g–i and j–l show carbohydrate-associated ions. Field of view: 500 × 500 µm². MC is the maximum count per pixel, and TC is the total count summed across all pixels for the specified m/z. Adapted from Paper III [63].*

4.3.6 Answer to RQ3

RQ3: Can a reference-guided ToF-SIMS and chemometrics workflow distinguish lignin-associated from polysaccharide-associated surface-ion patterns in chemically and topographically complex handsheets?

The workflow separated lignin-associated from polysaccharide-associated ions on Kraft handsheets. Ions such as *m/z* 137^+ and 151^+ marked lignin. Ions such as *m/z* 127^+, 133^+ and 145^+ marked polysaccharides [85, 89, 132]. Compacted reference samples were essential for improving mass resolution; however, handsheet surfaces remain subject to topography-driven extraction-field distortions and matrix-dependent ion yields. The resulting comparisons should therefore be treated as semi-quantitative rather than absolute [91, 94]. Some ions are ambiguous; for example, *m/z* 115^+ can come from both lignin and polysaccharides. In addition, PDMS-related fragments and unresolved peaks associated with bleaching highlight that exogenous surface species can dominate TIC and can enter the loading space unless explicitly screened [86, 131, 135]. Consequently, a marker set cannot be assumed to transfer directly to other measurements or surfaces. Its transfer depends on the acquisition conditions and on the chemical environment of the substrate. Cross-validation against suitable references and replicate-consistent multivariate separation make the transfer more reliable.

The next study tests this approach in a case where an external process variable changes the surface chemistry. It examines hot-pressed CTMP sheets. ToF-SIMS is combined with supervised chemometrics (OPLS-DA and SUS) to find temperature-dependent surface fingerprints and the molecular classes enriched at the surface.

4.4 Surface reorganization of CTMP paper during hot-pressing

This section addresses **RQ4** by examining how hot-pressing temperature reshapes the surface chemistry of CTMP papers, and whether ToF-SIMS with supervised chemometrics can resolve temperature-specific marker ions.

Background: Hot-pressing raises paper strength, which is attributed to lignin softening and interdiffusion, where softened lignin chains move across fiber–fiber contacts and form stronger bonds [97, 137]. Lignin and hemicellulose soften with heat and moisture [138, 139]. Heat can also move extractives to the surface of wood [96]. However, which chemical components reach the surface of a hot-pressed sheet, and how this depends on temperature, was not known.

Hypothesis: Hot-pressing promotes redistribution of mobile molecular components, producing temperature-discriminating ToF-SIMS fingerprints.

Approach: ToF-SIMS was combined with OPLS-DA and SUS plots to separate temperature effects from front/back-side chemical asymmetry and within-class variation on industrially hot-pressed CTMP sheets.

4.4.1 Dataset overview and modeling logic: separating temperature effects from front/back-side asymmetry

CTMP papers hot-pressed at 100 and 200 °C were analyzed on both the roll-contact (front-side) and opposite (back-side) surfaces (n = 6 positions per surface and temperature; 24 spectra total) [99]. Temperature is the main variable, and the front and back-sides serve as a control, so ions that change with temperature can be separated from those that differ between the two sides.

The CTMP surfaces vary in chemistry and differ between the two sides; the models were built in steps to isolate the effect of temperature. First, a PCA model of all spectra from the four surfaces (100 and 200 °C, front and back, M3) showed clear grouping by both temperature and side (**Figure 4.4.1a**). An OPLS-DA model of the same four classes, M4, confirmed that the groups could be reliably separated (**Figure 4.4.1b**). Two pairwise models were then built. One compared the front and back-sides at 100 °C (the side model, M5). The other compared 100 and 200 °C on the front-side (the temperature model, M6). The side model showed clear front/back differences at 100 °C, so side effects had to be considered when interpreting temperature effects. The temperature model gave the clearest

separation, indicating that hot-pressing temperature was the main driver of the front-side surface chemistry.

Two additional pairwise models, front against back at 200 °C (M7) and 100 against 200 °C on the back-side (M8), were evaluated to check whether new temperature-specific information emerged away from the roll-contact surface during hot-pressing. These models did not reveal additional temperature-driven marker ions beyond those already captured by M5 and M6, supporting the focus on the front-side temperature contrast. Model statistics are given in **Paper IV (Supplementary Figures S1–S9)**, where the models are numbered M3–M8.

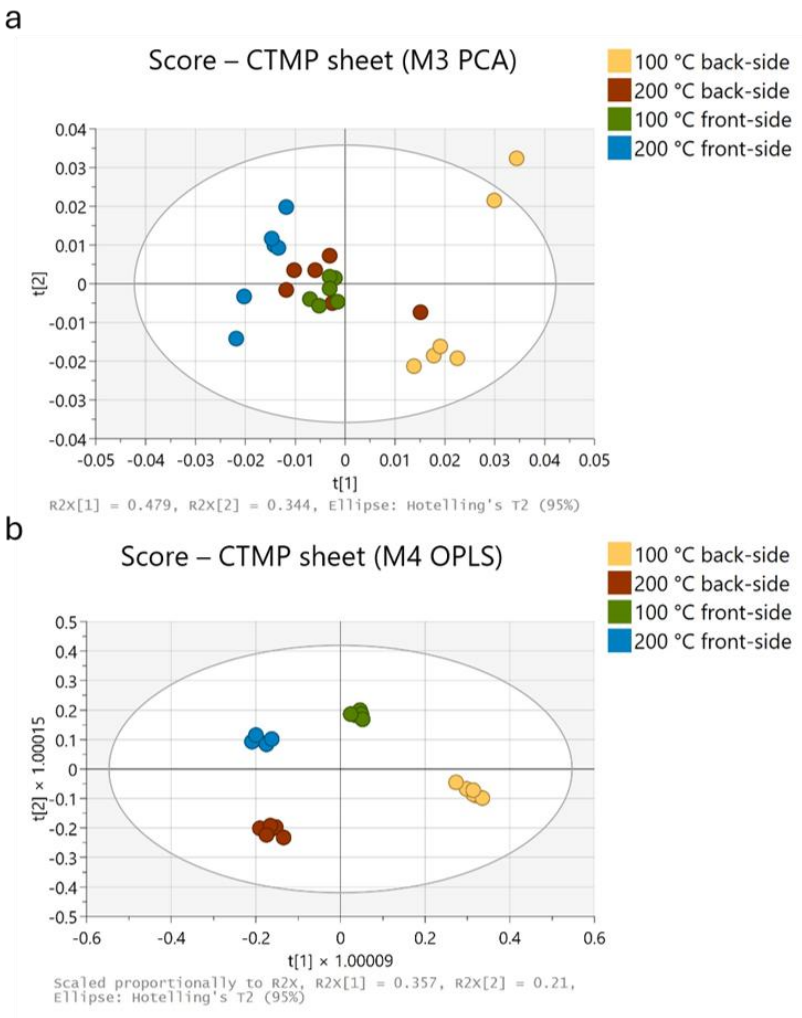


Figure 4.4.1: *Score plots of (a) model M3 and (b) model M4. Adapted from Paper IV* [62].

4.4.2 SUS-plot selection of temperature-specific marker ions independent of side effects (selection criteria and interpretation)

The temperature model (M6) shows which ions differ between 100 and 200 °C, but some of these ions may also differ between the front and back-sides. The side model (M5) shows which ions differ between front and back at 100 °C, but says nothing about temperature. Looking at each model separately therefore cannot show which ions respond only to temperature. A SUS plot solves this by plotting, for every ion, its loading in the side model against its loading in the temperature model [140-142]. Ions that are strong in the temperature model but weak in the side model respond to temperature alone and were selected as markers.

Each ion falls into one of four regions of the SUS plot (**Figure 4.4.2**). Each ion's position is given by its p(corr) value in the two models. p(corr) is a correlation coefficient, a number between −1 and +1 that shows how closely two variables move together. Here, it shows how closely an ion's intensity follows the difference between the two classes in each model (i.e., 100 °C and 200 °C in the temperature model, and front and back-sides in the side model). In the temperature model, a value near +1 means the ion is consistently higher at 200 °C, and a value near −1 means it is consistently higher at 100 °C. In the side model, the sign shows whether the ion is higher on the front or the back-side. A value near 0 means there is no clear link to either class.

In the SUS plot in **Figure 4.4.2**, the upper blue region contains ions enriched at 200 °C, and the lower blue region contains ions enriched at 100 °C. Ions in the green regions are side-specific: they are strong in the side model but weak in the temperature model. Ions in the orange regions are strong in both models, so their temperature and side effects cannot be separated. Ions near the origin are not important in either model. Only the temperature-specific ions in the blue regions were kept as markers (shown as yellow stars in **Figure 4.4.2**). These were used for the comparisons in **Figure 4.4.3** and the assignments in **Table 7.**

Table 7: *Temperature-enriched marker ions with tentative assignments.*

Temperature	Main enriched ion classes	Representative *m/z*
100 °C	Carbohydrate/aromatic fragments; sterol-related ions; medium-chain fatty-acid salt/adduct ions	63^+, 87^+, 109^+, 411^+, 413^+, 415^+, 523^+
200 °C	Lignin-related aromatic fragments; long-chain fatty-acid features; Ca-containing metal-carboxylate ions	128^+, 165^+, 268^+, 296^+, 355^+, 369^+, 383^+

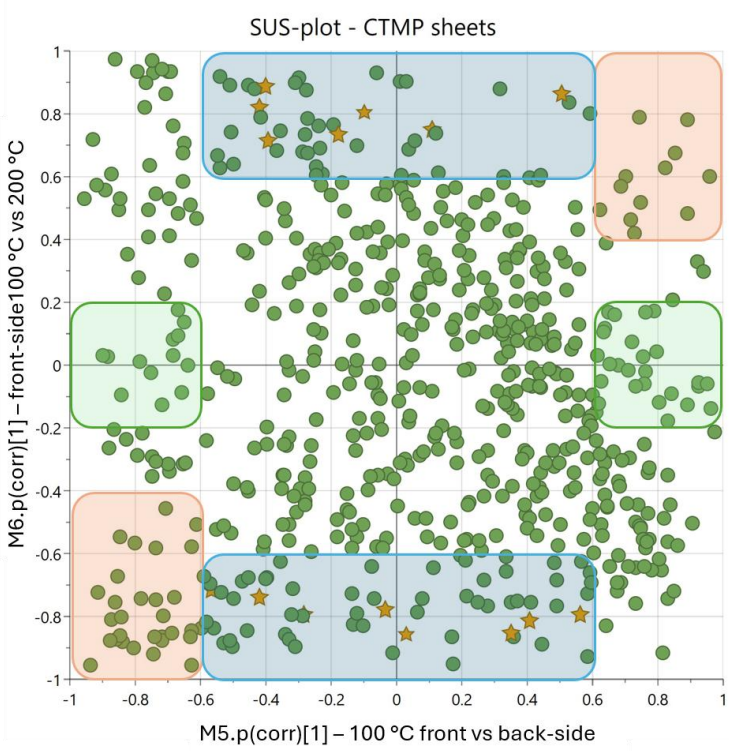


Figure 4.4.2: *SUS plot comparing the 100 °C front-side versus back-side model (M5) with the 100 °C versus 200 °C front-side model (M6) for hot-pressed CTMP paper. Yellow stars mark selected temperature-specific marker ions, defined by |M6.p(corr)| ≥ 0.6 and |M5.p(corr)| < 0.6. Blue boxes indicate ions enriched at the front-side after 100 °C or 200 °C hot-pressing, with minimal contribution from side effects. Orange boxes indicate ions contributing to both temperature and*

front/back-side contrasts, while green boxes indicate ions predominantly associated with front/back-side differences at 100 °C. Adapted from Paper IV [62].

4.4.3 Semi-quantitative validation of temperature-responsive ions

The temperature markers selected from the SUS plot were confirmed by comparing their TIC-normalized intensities between classes (n = 6 positions per class). **Figure 4.4.3** shows these intensities as violin plots, which show the spread of the six positions.

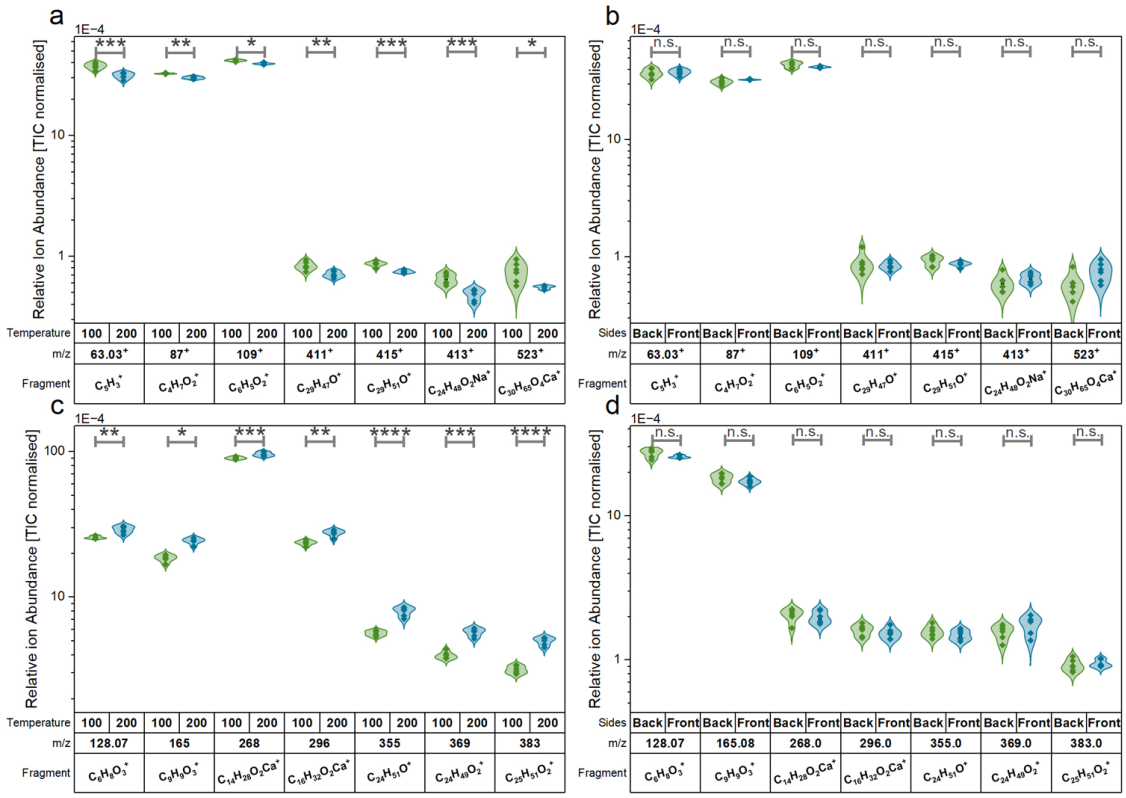


Figure 4.4.3: *TIC-normalized abundances of selected temperature-responsive ions on hot-pressed CTMP surfaces: (a) front-side comparison at 100 and 200 °C for ions enriched at 100 °C; (b) corresponding front/back-side control at 100 °C; (c) front-side comparison at 100 and 200 °C for ions enriched at 200 °C; and (d) corresponding front/back-side control at 200 °C. Statistical significance was assessed using Welch's t-test; *p < 0.05, **p < 0.01, ***p < 0.001 and ****p < 0.0001; n.s., not significant. Adapted from Paper IV [62].*

For ions enriched at 100 °C, the front-side showed higher relative abundances at 100 °C than at 200 °C of small lignin- and carbohydrate-related fragments (*m/z* 63^+, 87^+ and 109^+), sterol-related ions (*m/z* 411^+ and 415^+), and fatty-acid salt/adduct signals (*m/z* 413^+ and 523^+) (**Figure 4.4.3a**). The corresponding 100 °C front/back-side control showed no systematic side-dependent differences for these same ions (**Figure 4.4.3b**), supporting their interpretation as temperature-responsive rather than side-specific markers. The tentative assignments are consistent with earlier ToF-SIMS studies of lignocellulosic fragment ions and pulp extractives [83, 85, 143, 144].

The ions enriched at 200 °C (**Figure 4.4.3c**) included lignin-associated fragments (*m/z* 128^+ and 165^+), together with fatty-acid and metal-carboxylate-related features, including *m/z* 268^+, 296^+, 355^+, 369^+ and 383^+. These assignments are consistent with lignin-derived fragments, fatty-acid-related ions, and calcium-containing adducts reported previously for lignocellulosic and pulp-fiber surfaces [83, 85, 90, 145, 146]. The Ca-containing adducts may originate from calcium-containing water or process streams during pulp washing or sheet preparation. The corresponding 200 °C front/back-side control showed no systematic side dependence for these same ions (**Figure 4.4.3d**), indicating that the observed differences are primarily associated with temperature treatment rather than inherent paper-side asymmetry.

4.4.4 Interpretation and implications: extractives/lignin mobility, fatty-acid salt enrichment, and process-relevant surface tuning

The marker ions suggest that hot-pressing not only densifies CTMP paper but also changes which components are present at the surface, depending on temperature. At 100 °C, the front-side showed more small carbohydrate- and lignin-related fragments, sterols and fatty-acid salt adducts. At 200 °C, it showed more lignin-related aromatic fragments, C24–C25 fatty-acid fragments and Ca-carboxylate species. These contrasts are consistent with moisture-assisted thermal softening during hot-pressing. Residual moisture likely plasticizes the amorphous lignin- and hemicellulose-rich domains before it evaporates, increasing polymer-segment mobility under heat and pressure and thereby facilitating redistribution of lignin-rich and hydrophobic extractive-related species toward the roll-contact surface [97, 98, 137-139]. Given the short residence time in the heated nip, the differences may be interpreted as surface reorganization of existing components rather than as extensive thermal degradation [143, 147].

From an application perspective, this change from sterol- and fatty-acid-salt signatures at 100 °C to lignin and Ca–fatty-acid signatures at 200 °C implies a systematic change in surface chemistry and interfacial behavior. Such changes are expected to influence wettability, surface energy, coating and ink interactions and adhesion, and may also affect barrier behavior through increased hydrophobic surface coverage [100, 101]. This small set of marker ions can be used to follow surface-chemical changes when choosing hot-pressing conditions, so that surface chemistry can be tuned along with smoothness and gloss of the paper surfaces.

4.4.5 Answer to RQ4

RQ4: How does hot-pressing temperature reshape the surface chemistry of papers, and can ToF-SIMS with supervised chemometrics resolve temperature-specific marker ions?

ToF-SIMS showed reproducible, temperature-dependent changes in the outermost surface of hot-pressed CTMP sheets. OPLS-DA with SUS-plot filtering separated temperature-responsive ions from front/back-side differences. A At 100 °C, the front-side had more sterol, fatty-acid-salt and small carbohydrate-related ions. At 200 °C, it had more lignin-related, long-chain fatty-acid and Ca–fatty-acid ions. This is consistent with redistribution of components already in the sheet toward the heated surface. Nip temperature may therefore be a way to tune surface composition, which could matter for coating, printing and barrier performance.

5 Conclusion

This thesis asked how chemical modification, drying history, pulp processing and thermal treatments reorganize cellulose fibers across length scales, and how these changes relate to fiber behavior. It follows two lines. The first studies dialcohol cellulose (DALC), from fiber swelling to nanoscale structure. The second studies fiber and sheet surfaces after pulping and hot-pressing. They share one aim: to link a treatment to structure and then to function.

In DALC, higher modification increased heterogeneous swelling, first as balloon-collar morphology. At 51% DOM, uniformly swollen fibers appeared alongside balloon-collar fibers, so swelling remained heterogeneous between and along fibers. X-ray scattering showed lower crystallinity and an increased SAXS-derived characteristic length, an apparent length scale of the fibrillar arrangement in the fiber wall. In never-dried fibers, these length scales increased together with water retention. Drying lowered the characteristic length, and rewetting did not restore them completely to never-dried levels.

At the surface, ToF-SIMS with chemometrics separated lignin-associated from polysaccharide-associated ions on Kraft handsheets. Because surface topography and matrix effects alter ion yields, these comparisons are relative rather than absolute. In hot-pressed CTMP, temperature changed which components dominate the surface: sterol- and fatty-acid-salt ions at 100 °C, and lignin-related, long-chain fatty-acid and Ca–fatty-acid ions at 200 °C. This is consistent with temperature-driven redistribution of native lignin and extractive components at the heated surface.

This thesis provides a multiscale framework that links chemistry, structure and surface. It also provides a validated ToF-SIMS and chemometrics workflow for surface fingerprinting of complex lignocellulosic surfaces.

6 Scientific Reflections: Beyond the Thesis

Looking back over the past four years, the greatest learning from this research is not that cellulose fibers are more complex than I imagined, but that they are far more dynamic. I viewed chemistry, structure, and surface composition as separate characteristics, and investigated them independently with different techniques. As my studies progressed, it became clear that they are different manifestations of the same hierarchical system: chemical modification alters the fiber wall, structural organization responds across length scales, and these changes ultimately determine the chemistry expressed at the surface. Pulp processing and thermal treatments on the fibers add a further dimension by continuously reorganizing this system.

This realization transformed my perspective on cellulose fibers. Instead of asking what changes, I found myself asking how, when, and, more importantly, why. Each completed study answered one question while opening several new questions that may ultimately be as important as the findings themselves.

One of my first reflections concerns time. Throughout this thesis, fibers were characterized before and after chemical modification, drying, or thermal treatments, yet the transformations occurring between these states remain largely invisible. This naturally leads me to wonder:

How does fiber wall reorganization evolve in real time during chemical modification, swelling, drying, and thermal treatments?

Are morphology, nanostructure, and surface chemistry reorganized simultaneously, or do they evolve sequentially, one level of hierarchy initiating changes in another? Answering this would move cellulose science from observing static states toward understanding dynamic structural evolution.

The hot-pressing study further challenged my understanding of cellulose surfaces. The temperature-dependent redistribution of extractives and fatty acids suggested that the fiber surface is far more dynamic than often assumed, evolving continuously as molecular mobility increases. This immediately raises a question:

How do lignin, hemicellulose, and extractives such as fatty acids and resin acids interact during this redistribution process?

This question extends beyond analytical chemistry, sitting at the interface between cellulose chemistry, polymer physics, and industrial processing, where molecular mobility remains one of the least understood aspects of lignocellulosic materials.

Perhaps the most intriguing question emerging from this work concerns whether cellulose fibers possess a form of processing memory. This study compared independently processed samples at different temperatures, but an equally interesting experiment would ask whether the pathway itself influences the final surface state—comparing sequential hot-pressing of the same specimen (Reference → 100 °C → 200 °C) with specimens processed directly at each temperature. Such an experiment would answer a fundamental question:

Does the surface chemistry of lignocellulosic materials depend only on the final processing temperature, or does it retain a cumulative thermal memory of previous processing history?

If different pathways produce different surface chemistries despite reaching the same final temperature, this suggests that surface reorganization is fundamentally path-dependent, offering new insight into the kinetics, reversibility, and memory effects associated with polymer mobility, extractive migration, and surface reconstruction.

Another reflection arises from the relationship established between nanoscale structure and swelling. In never-dried DALC fibers, SAXS-derived nanostructural descriptors and macroscopic swelling (WRV) increased monotonically with DOM, prompting a broader question:

Could universal structural descriptors exist that predict swelling behavior across fundamentally different lignocellulosic materials?

If parameters describing fibrillar arrangement prove transferable beyond dialcohol cellulose to Kraft fibers, CTMP, TMP, regenerated cellulose, nanocellulose, or other bio-based fiber systems, they could form the basis of a universal framework linking molecular organization to macroscopic performance.

The cross-scale link between nanostructure and swelling also left me with a caveat I could not fully resolve. The clean, approximately linear relationship between WRV

and ℓ_k was established specifically in never-dried fibers, and whether it survives a full drying and rewetting cycle remains open:

Does the WRV–nanostructure relationship survive drying history, or is it a never-dried-only phenomenon?

The test would be to measure WRV on rewetted fibers: if it recovers in step with ℓ_k, the relationship holds beyond the never-dried state; if not, SAXS descriptors could not serve as a general proxy for WRV. This distinction matters for anyone seeking to use nanoscale descriptors to predict swelling in processed, rather than never-dried, pulps, where drying history is unavoidable.

The microscopy studies also exposed a limitation in how these observations were made. Even fibers under identical modification responded differently: some showed localized balloon-collar swelling, others remarkably uniform expansion. Yet the SAXS, WAXS, and ToF-SIMS measurements in this thesis are inherently population-averaged: each spectrum represents a bulk signal from many fibers, not a resolved comparison between the ballooned and collar regions visibly distinguishable within a single fiber under the microscope. This leaves a gap between what is seen and what is measured, leading me to wonder:

Do the nanoscale correlation length and crystallinity, or the surface chemistry, differ systematically between a balloon and its adjacent collar within the same fiber?

Answering this would require moving beyond population-averaged techniques toward spatially resolved, correlative measurements, for example, directing micro-focused SAXS or ToF-SIMS imaging to balloon and collar regions already identified by microscopy on the same fiber. Such an approach would reveal whether the heterogeneity observed visually is mirrored at the nanoscale and surface-chemical level, or whether balloon and collar regions are structurally and chemically more similar than their swelling behavior alone suggests.

Reflecting on all four studies together, perhaps the greatest opportunity lies not in developing individual techniques but in combining them. Light microscopy, SAXS/WAXS, ToF-SIMS, and advanced chemometrics each provide only one perspective on an exceptionally complex material. Future developments in machine learning offer the possibility of integrating these complementary datasets

into predictive frameworks rather than treating them as independent observations. This naturally leads to the question:

Can multiscale experimental datasets be integrated to predict fiber behavior before experiments are performed?

Such predictive capability would be an important step toward data-driven materials design, where experiments and computation continuously inform one another, representing a transition from descriptive characterization toward predictive materials science, and enabling cellulose fibers to be engineered with targeted structures, surface chemistry, and functional properties before they are ever produced.

Looking back, the most significant outcome of this research is not the individual findings of each study, but the recognition that chemistry, structure, surface, and processing cannot be understood in isolation. They are inseparable, and cellulose fibers reveal their behavior only when these dimensions are read together across length scales.

7 Bibliography

(1) Segers, B.; Nimmegeers, P.; Spiller, M.; Tofani, G.; Jasiukaitytė-Grojzdek, E.; Dace, E.; Kikas, T.; Marchetti, J. M.; Rajić, M.; Yildiz, G.; et al. Lignocellulosic biomass valorisation: a review of feedstocks, processes and potential value chains and their implications for the decision-making process. *RSC Sustainability* **2024**, *2* (12), 3730-3749. DOI: https://doi.org/10.1039/D4SU00342J.

(2) Cosgrove, D. J. Building an extensible cell wall. *Plant Physiology* **2022**, *189* (3), 1246-1277. DOI: https://doi.org/10.1093/plphys/kiac184.

(3) Kang, X.; Kirui, A.; Dickwella Widanage, M. C.; Mentink-Vigier, F.; Cosgrove, D. J.; Wang, T. Lignin-polysaccharide interactions in plant secondary cell walls revealed by solid-state NMR. *Nature Communications* **2019**, *10* (1), 347. DOI: https://doi.org/10.1038/s41467-018-08252-0.

(4) Kirui, A.; Zhao, W.; Deligey, F.; Yang, H.; Kang, X.; Mentink-Vigier, F.; Wang, T. Carbohydrate-aromatic interface and molecular architecture of lignocellulose. *Nature Communications* **2022**, *13* (1), 538. DOI: https://doi.org/10.1038/s41467-022-28165-3.

(5) Terrett, O. M.; Lyczakowski, J. J.; Yu, L.; Iuga, D.; Franks, W. T.; Brown, S. P.; Dupree, R.; Dupree, P. Molecular architecture of softwood revealed by solid-state NMR. *Nature Communications* **2019**, *10* (1), 4978. DOI: https://doi.org/10.1038/s41467-019-12979-9.

(6) Simmons, T. J.; Mortimer, J. C.; Bernardinelli, O. D.; Pöppler, A.-C.; Brown, S. P.; deAzevedo, E. R.; Dupree, R.; Dupree, P. Folding of xylan onto cellulose fibrils in plant cell walls revealed by solid-state NMR. *Nature Communications* **2016**, *7* (1), 13902. DOI: https://doi.org/10.1038/ncomms13902.

(7) Goutianos, S.; Mao, R.; Peijs, T. Effect of inter-fibre bonding on the fracture of fibrous networks with strong interactions. *International Journal of Solids and Structures* **2018**, *136-137*, 271-278. DOI: https://doi.org/10.1016/j.ijsolstr.2017.12.020.

(8) Salmén, L.; Olsson, A.-M.; Stevanic, J.; Simonovic Radosavljevic, J.; Radotić, K. Structural organisation of the wood polymers in the wood fibre structure. *BioResources* **2012**, *7*, 521-532.

(9) Lindner, M. Factors affecting the hygroexpansion of paper. *Journal of Materials Science* **2018**, *53* (1), 1-26. DOI: https://doi.org/10.1007/s10853-017-1358-1.

(10) Zhang, B.; Gao, Y.; Zhang, L.; Zhou, Y. The plant cell wall: Biosynthesis, construction, and functions. *Journal of Integrative Plant Biology* **2021**, *63* (1), 251-272. DOI: https://doi.org/10.1111/jipb.13055.

(11) Hirn, U.; Schennach, R. Comprehensive analysis of individual pulp fiber bonds quantifies the mechanisms of fiber bonding in paper. *Scientific Reports* **2015**, *5* (1), 10503. DOI: https://doi.org/10.1038/srep10503.

(12) Klemm, D.; Heublein, B.; Fink, H. P.; Bohn, A. Cellulose: fascinating biopolymer and sustainable raw material. *Angewandte chemie international edition* **2005**, *44* (22), 3358-3393. DOI: https://doi.org/10.1002/anie.200460587.

(13) Somerville, C.; Bauer, S.; Brininstool, G.; Facette, M.; Hamann, T.; Milne, J.; Osborne, E.; Paredez, A.; Persson, S.; Raab, T.; et al. Toward a Systems Approach to Understanding Plant Cell Walls. *Science* **2004**, *306* (5705), 2206-2211. DOI: https://doi.org/10.1126/science.1102765.

(14) Aziz, T.; Haq, F.; Farid, A.; Kiran, M.; Faisal, S.; Ullah, A.; Ullah, N.; Bokhari, A.; Mubashir, M.; Chuah, L. F.; et al. Challenges associated with cellulose composite material: Facet engineering and prospective. *Environmental Research* **2023**, *223*, 115429. DOI: https://doi.org/10.1016/j.envres.2023.115429.

(15) Zeronian, S. H.; Hudson, F. L.; Peters, R. H. The mechanical properties of paper made from periodate oxycellulose pulp and from the same pulp after reduction with borohydride. *Tappi* **1964**, *47* (9), 557-564.

(16) Heise, K.; Koso, T.; King, A. W. T.; Nypelö, T.; Penttilä, P.; Tardy, B. L.; Beaumont, M. Spatioselective surface chemistry for the production of functional and chemically anisotropic nanocellulose colloids. *Journal of Materials Chemistry A* **2022**, *10* (44), 23413-23432. DOI: https://doi.org/10.1039/d2ta05277f.
(17) Zhang, L.; Larsson, A.; Moldin, A.; Edlund, U. Comparison of lignin distribution, structure, and morphology in wheat straw and wood. *Industrial Crops and Products* **2022**, *187*, 115432. DOI: https://doi.org/10.1016/j.indcrop.2022.115432.
(18) Sjöström, E. Chapter 1 - The Structure of Wood. In *Wood Chemistry (Second Edition)*, Sjöström, E. Ed.; Academic Press, 1993; pp 1-20.
(19) Nishiyama, Y. Structure and properties of the cellulose microfibril. *Journal of Wood Science* **2009**, *55* (4), 241-249. DOI: https://doi.org/10.1007/s10086-009-1029-1.
(20) Stone, J. E. The Effect of Component Removal Upon the Porous Structure of the Cell Wall of Wood. *Pulp and Paper Magazine of Canada* **1968**, 69-74.
(21) Hubbe, M.; Sjöstrand, B.; Lestelius, M.; Håkansson, H.; Swerin, A.; Henriksson, G. Swelling of cellulosic fibers in aqueous systems: A Review of chemical and mechanistic factors. *BioResources* **2024**, *19*, 6859-6945. DOI: https://doi.org/10.15376/biores.19.3.Hubbe.
(22) Wardrop, A. B.; Dadswell, H. E. The Swelling Behaviour of Conifer Tracheids and the Concept of Skin Substance. In *Appita Proceedings*, 1950; pp 198-221.
(23) Cave, I. D. Modelling the structure of the softwood cell wall for computation of mechanical properties. *Wood Science and Technology* **1976**, *10* (1), 19-28. DOI: https://doi.org/10.1007/BF00376381.
(24) Hubbe, M.; Ferrer, A.; Tyagi, P.; Yin, Y.; Salas, C.; Pal, L.; Rojas, O. Nanocellulose in Thin Films, Coatings, and Plies for Packaging Applications: A Review. *BioResources* **2017**, *12*, 2143-2233. DOI: https://doi.org/10.15376/biores.12.1.2143-2233.
(25) Laine, J.; Stenius, P.; Carlsson, G.; Ström, G. The effect of ECF and TCF bleaching on the surface chemical composition of kraft pulp as determined by ESCA. *Nordic Pulp & Paper Research Journal* **1996**, *11*, 201-210.
(26) Laine, J.; Stenius, P.; Carlsson, G.; Ström, G. Surface characterization of unbleached kraft pulps by means of ESCA. *Cellulose* **1994**, *1* (2), 145-160. DOI: https://doi.org/10.1007/BF00819664.
(27) Li, J.; Kasal, B. Review on the Structure–Property Relationship of Lignocellulosic Materials Measured by Atomic Force Microscopy. *Biomacromolecules* **2025**, *26* (3), 1404-1418. DOI: https://doi.org/10.1021/acs.biomac.4c01278.
(28) Hubbe, M.; Rojas, O.; Lucia, L. Green Modification of Surface Characteristics of Cellulosic Materials at the Molecular or Nano Scale: A Review. *BioResources* **2015**, *10* (3), 6095–6206. DOI: https://doi.org/10.15376/biores.10.3.Hubbe.
(29) Cave, I. D.; Walker, J. C. F. Stiffness of wood in fast-grown plantation softwoods: the influence of microfibril angle. *Forest Products Journal* **1994**, *44*, 43-48.
(30) Tabet, T. A.; Abdul Aziz, F. Cellulose Microfibril Angle in Wood and Its Dynamic Mechanical Significance. In *Cellulose – Fundamental Aspects*, van de Ven, T. G. M., Godbout, L. Eds.; InTech, 2013; pp 113-142.
(31) Hoffmann, P.; Jones, M. A. Structure and Degradation Process for Waterlogged Archaeological Wood. In *Archaeological Wood*, Advances in Chemistry, Vol. 225; American Chemical Society, 1989; pp 35-65.
(32) Wang, H.-M.; Yuan, T.-Q.; Song, G.-Y.; Sun, R.-C. Advanced and versatile lignin-derived biodegradable composite film materials toward a sustainable world. *Green Chemistry* **2021**, *23* (11), 3790-3817. DOI: https://doi.org/10.1039/D1GC00790D.

(33) Reza, M.; Bertinetto, C.; Ruokolainen, J.; Vuorinen, T. Cellulose Elementary Fibrils Assemble into Helical Bundles in S1 Layer of Spruce Tracheid Wall. *Biomacromolecules* **2017**, *18* (2), 374-378. DOI: https://doi.org/10.1021/acs.biomac.6b01396.
(34) Rafsanjani, A.; Stiefel, M.; Jefimovs, K.; Mokso, R.; Derome, D.; Carmeliet, J. Hygroscopic swelling and shrinkage of latewood cell wall micropillars reveal ultrastructural anisotropy. *Journal of the Royal Society Interface* **2014**, *11* (95), 20140126. DOI: https://doi.org/10.1098/rsif.2014.0126.
(35) Larsson, P. T.; Stevanic-Srndovic, J.; Roth, S. V.; Söderberg, D. Interpreting SAXS data recorded on cellulose rich pulps. *Cellulose* **2022**, *29* (1), 117-131. DOI: https://doi.org/10.1007/s10570-021-04291-x.
(36) Kotov, N.; Larsson, P. A.; Jain, K.; Abitbol, T.; Cernescu, A.; Wågberg, L.; Johnson, C. M. Elucidating the fine-scale structural morphology of nanocellulose by nano infrared spectroscopy. *Carbohydrate Polymers* **2023**, *302*, 120320. DOI: https://doi.org/10.1016/j.carbpol.2022.120320.
(37) Isogai, A.; Saito, T.; Fukuzumi, H. TEMPO-oxidized cellulose nanofibers. *Nanoscale* **2011**, *3* (1), 71-85. DOI: https://doi.org/10.1039/C0NR00583E.
(38) Moon, R. J.; Martini, A.; Nairn, J.; Simonsen, J.; Youngblood, J. Cellulose nanomaterials review: structure, properties and nanocomposites. *Chemical Society Reviews* **2011**, *40* (7), 3941-3994. DOI: https://doi.org/10.1039/C0CS00108B.
(39) Lavoine, N.; Desloges, I.; Dufresne, A.; Bras, J. Microfibrillated cellulose - its barrier properties and applications in cellulosic materials: a review. *Carbohydrate Polymers* **2012**, *90* (2), 735-764. DOI: https://doi.org/10.1016/j.carbpol.2012.05.026.
(40) Zhou, J.; Fang, Z.; Chen, K.; Cui, J.; Yang, D.; Qiu, X. Improving the degree of polymerization of cellulose nanofibers by largely preserving native structure of wood fibers. *Carbohydrate Polymers* **2022**, *296*, 119919. DOI: https://doi.org/10.1016/j.carbpol.2022.119919.
(41) Mihranyan, A.; Llagostera, A. P.; Karmhag, R.; Strømme, M.; Ek, R. Moisture sorption by cellulose powders of varying crystallinity. *International Journal of Pharmaceutics* **2004**, *269* (2), 433-442. DOI: https://doi.org/10.1016/j.ijpharm.2003.09.030.
(42) Elfaleh, I.; Abbassi, F.; Habibi, M.; Ahmad, F.; Guedri, M.; Nasri, M.; Garnier, C. A comprehensive review of natural fibers and their composites: An eco-friendly alternative to conventional materials. *Results in Engineering* **2023**, *19*, 101271. DOI: https://doi.org/10.1016/j.rineng.2023.101271.
(43) Sjöstedt, A. Preparation and characterization of nanoporous cellulose fibres and their use in new material concepts. Doctoral thesis, KTH Royal Institute of Technology, Stockholm, Sweden, 2014.
(44) Palasingh, C.; Nakayama, K.; Abik, F.; Mikkonen, K. S.; Evenäs, L.; Ström, A.; Nypelö, T. Modification of xylan via an oxidation–reduction reaction. *Carbohydrate Polymers* **2022**, *292*, 119660. DOI: https://doi.org/10.1016/j.carbpol.2022.119660.
(45) Nypelö, T.; Berke, B.; Spirk, S.; Sirviö, J. A. Review: Periodate oxidation of wood polysaccharides-Modulation of hierarchies. *Carbohydrate Polymers* **2021**, *252*, 117105. DOI: https://doi.org/10.1016/j.carbpol.2020.117105.
(46) Kristiansen, K. A.; Potthast, A.; Christensen, B. E. Periodate oxidation of polysaccharides for modification of chemical and physical properties. *Carbohydrate Research* **2010**, *345* (10), 1264-1271. DOI: https://doi.org/10.1016/j.carres.2010.02.011.
(47) Börjesson, M.; Larsson, A.; Westman, G.; Ström, A. Periodate oxidation of xylan-based hemicelluloses and its effect on their thermal properties. *Carbohydrate Polymers* **2018**, *202*, 280-287. DOI: https://doi.org/10.1016/j.carbpol.2018.08.110.

(48) Venkatraman, N.; Jonasson, K.; Lo Re, G.; Larsson, P. A.; Larsson, A. Impact of dialcohol cellulose modification on the structural morphology and swelling behaviour of cellulose fibres. *Cellulose* **2025**, *32* (14), 8101-8117. DOI: https://doi.org/10.1007/s10570-025-06729-y.
(49) Mehandzhiyski, A. Y.; Engel, E.; Larsson, P. A.; Lo Re, G.; Zozoulenko, I. V. Microscopic Insight into the Structure-Processing-Property Relationships of Core-Shell Structured Dialcohol Cellulose Nanoparticles. *ACS Applied Bio Materials* **2022**, *5* (10), 4793-4802. DOI: https://doi.org/10.1021/acsabm.2c00505.
(50) Engel, E. R.; Lo Re, G.; Larsson, P. A. Melt processing of chemically modified cellulosic fibres with only water as plasticiser: Effects of moisture content and processing temperature. *Carbohydrate Polymers* **2025**, *348*, 122891. DOI: https://doi.org/10.1016/j.carbpol.2024.122891.
(51) Larsson, P. A.; Berglund, L. A.; Wågberg, L. Highly ductile fibres and sheets by core-shell structuring of the cellulose nanofibrils. *Cellulose* **2013**, *21* (1), 323-333. DOI: https://doi.org/10.1007/s10570-013-0099-9.
(52) Larsson, P. A.; Berglund, L. A.; Wågberg, L. Ductile all-cellulose nanocomposite films fabricated from core-shell structured cellulose nanofibrils. *Biomacromolecules* **2014**, *15* (6), 2218-2223. DOI: https://doi.org/10.1021/bm500360c.
(53) Larsson, P. A.; Gimåker, M.; Wågberg, L. The influence of periodate oxidation on the moisture sorptivity and dimensional stability of paper. *Cellulose* **2008**, *15* (6), 837-847. DOI: https://doi.org/10.1007/s10570-008-9243-3.
(54) Larsson, P. A.; Kochumalayil, J. J.; Wågberg, L. Oxygen and water vapour barrier films with low moisture sensitivity fabricated from self-crosslinking fibrillated cellulose. In Fundamental Research Symposium, Cambridge, UK; September, 2013.
(55) Kim, U.-J.; Kuga, S.; Wada, M.; Okano, T.; Kondo, T. Periodate Oxidation of Crystalline Cellulose. *Biomacromolecules* **2000**, *1* (3), 488-492. DOI: https://doi.org/10.1021/bm0000337.
(56) Karlsson, H.; Svenningsson, L.; Storm, R.; Chaiyupatham, P.; Brolin, A.; Larsson, A.; Pinon, A. C.; Schantz, S.; Karlson, L.; Larsson, P. A.; et al. Dynamic nuclear polarization solid-state NMR spectroscopy as a tool to rapidly determine degree of modification in dialcohol cellulose. *Cellulose* **2024**, *31* (18), 10727-10744. DOI: https://doi.org/10.1007/s10570-024-06234-8.
(57) Elf, P.; Larsson, P. A.; Larsson, A.; Wågberg, L.; Hedenqvist, M. S.; Nilsson, F. Effects of Ring Opening and Chemical Modification on the Properties of Dry and Moist Cellulose–Predictions with Molecular Dynamics Simulations. *Biomacromolecules* **2024**, *25* (12), 7581-7593. DOI: https://doi.org/10.1021/acs.biomac.4c00735.
(58) López Durán, V.; Larsson, P. A.; Wågberg, L. On the relationship between fibre composition and material properties following periodate oxidation and borohydride reduction of lignocellulosic fibres. *Cellulose* **2016**, *23* (6), 3495-3510. DOI: https://doi.org/10.1007/s10570-016-1061-4.
(59) López Durán, V.; Larsson, P. A.; Wågberg, L. Chemical modification of cellulose-rich fibres to clarify the influence of the chemical structure on the physical and mechanical properties of cellulose fibres and thereof made sheets. *Carbohydrate Polymers* **2018**, *182*, 1-7. DOI: https://doi.org/10.1016/j.carbpol.2017.11.006.
(60) Linvill, E.; Larsson, P. A.; Östlund, S. Advanced three-dimensional paper structures: Mechanical characterization and forming of sheets made from modified cellulose fibers. *Materials & Design* **2017**, *128*, 231-240. DOI: https://doi.org/10.1016/j.matdes.2017.05.002.
(61) Linvill, E.; Larsson, P. A.; Östlund, S. Dynamic Mechanical Thermal Analysis Data of Sheets Made from Wood-Based Cellulose Fibers Partially Converted to Dialcohol Cellulose. *Data in Brief* **2017**, *14*, 504-506. DOI: https://doi.org/10.1016/j.dib.2017.07.014.

(62) Venkatraman, N.; Leksuntrakorn, J.; Brolin, A.; Malmberg, P.; Larsson, A. Temperature-driven surface reorganization in hot-pressed CTMP sheets revealed by ToF-SIMS and chemometrics. *Polymer Testing* **2026**, *161*, 109301. DOI: https://doi.org/10.1016/j.polymertesting.2026.109301.
(63) Venkatraman, N.; Larsson, P. A.; Larsson, A.; Malmberg, P. Surface profiling of cellulose, hemicellulose, and lignin in softwood Kraft handsheets by reference-guided ToF-SIMS. *Carbohydrate Polymer Technologies and Applications* **2026**, *15*, 101209. DOI: https://doi.org/10.1016/j.carpta.2026.101209.
(64) Karlsson, R.-M. P.; Larsson, P. T.; Pettersson, T.; Wågberg, L. Swelling of Cellulose-Based Fibrillar and Polymeric Networks Driven by Ion-Induced Osmotic Pressure. *Langmuir* **2020**, *36* (41), 12261-12271. DOI: https://doi.org/10.1021/acs.langmuir.0c02051.
(65) Sim, G.; Alam, M. N.; Godbout, L.; van de Ven, T. G. M. Structure of swollen carboxylated cellulose fibers. *Cellulose* **2014**, *21* (6), 4595-4606. DOI: https://doi.org/10.1007/s10570-014-0425-x.
(66) Grignon, J.; Scallan, A. M. Effect of pH and neutral salts upon the swelling of cellulose gels. *Journal of Applied Polymer Science* **1980**, *25* (12), 2829-2843. DOI: https://doi.org/10.1002/app.1980.070251215.
(67) Navard, P.; Cuissinat, C. Cellulose swelling and dissolution as a tool to study the fiber structure. In Alternative Cellulose : Manufacturing, Forming, Properties, 2006.
(68) Simon, J.; Fliri, L.; Fröhlich, F.; Sapkota, J.; Ristolainen, M.; Hummel, M.; Rosenau, T.; Potthast, A. Insights into the borohydride reduction of dialdehyde cellulose: the dilemma of competing reduction and β-elimination reactions. *Cellulose* **2023**, *30* (13), 8205-8220. DOI: https://doi.org/10.1007/s10570-023-05350-1.
(69) Larsson, P. A.; Wågberg, L. Towards natural-fibre-based thermoplastic films produced by conventional papermaking. *Green Chemistry* **2016**, *18* (11), 3324-3333. DOI: https://doi.org/10.1039/c5gc03068d.
(70) Azzam, F.; Galliot, M.; Putaux, J.-L.; Heux, L.; Jean, B. Surface peeling of cellulose nanocrystals resulting from periodate oxidation and reductive amination with water-soluble polymers. *Cellulose* **2015**, *22* (6), 3701-3714. DOI: https://doi.org/10.1007/s10570-015-0785-x.
(71) Mayr, M.; Eckhart, R.; Winter, H.; Bauer, W. A novel approach to determining the contribution of the fiber and fines fraction to the water retention value (WRV) of chemical and mechanical pulps. *Cellulose* **2017**, *24* (7), 3029-3036. DOI: https://doi.org/10.1007/s10570-017-1298-6.
(72) Penttilä, P. A.; Paajanen, A.; Ketoja, J. A. Combining scattering analysis and atomistic simulation of wood-water interactions. *Carbohydrate Polymers* **2021**, *251*, 117064. DOI: https://doi.org/10.1016/j.carbpol.2020.117064.
(73) Paajanen, A.; Zitting, A.; Rautkari, L.; Ketoja, J. A.; Penttilä, P. A. Nanoscale Mechanism of Moisture-Induced Swelling in Wood Microfibril Bundles. *Nano Letters* **2022**, *22* (13), 5143-5150. DOI: https://doi.org/10.1021/acs.nanolett.2c00822.
(74) Penttilä, P. A.; Altgen, M.; Carl, N.; Van Der Linden, P.; Morfin, I.; Österberg, M.; Schweins, R.; Rautkari, L. Moisture-related changes in the nanostructure of woods studied with X-ray and neutron scattering. *Cellulose* **2020**, *27* (1), 71-87. DOI: https://doi.org/10.1007/s10570-019-02781-7.
(75) Penttilä, P. A.; Rautkari, L.; Österberg, M.; Schweins, R. Small-angle scattering model for efficient characterization of wood nanostructure and moisture behaviour. *Journal of Applied Crystallography* **2019**, *52* (2), 369-377. DOI: https://doi.org/10.1107/s1600576719002012.
(76) Garvey, C.; Parker, I.; Simon, G. On the Interpretation of X-Ray Diffraction Powder Patterns in Terms of the Nanostructure of Cellulose I Fibres. *Macromolecular Chemistry and Physics* **2005**, *206*, 1568-1575. DOI: https://doi.org/10.1002/macp.200500008.

(77) French, A. D. Increment in evolution of cellulose crystallinity analysis. *Cellulose* **2020**, *27* (10), 5445-5448. DOI: https://doi.org/10.1007/s10570-020-03172-z.
(78) Wålinder, M. E. P.; Ström, G. Measurement of Wood Wettability by the Wilhelmy Method. Part 2. Determination of Apparent Contact Angles. *Holzforschung* **2001**, *55* (1), 33-41. DOI: https://doi.org/10.1515/HF.2001.006.
(79) Koljonen, K.; Österberg, M.; Kleen, M.; Fuhrmann, A.; Stenius, P. Precipitation of lignin and extractives on kraft pulp: Effect on surface chemistry, surface morphology and paper strength. *Cellulose* **2004**, *11*, 209-224. DOI: https://doi.org/10.1023/B:CELL.0000025424.90845.c3.
(80) Jin, H.; Kose, R.; Akada, N.; Okayama, T. Relationship between wettability of pulp fibers and tensile strength of paper during recycling. *Scientific Reports* **2022**, *12* (1), 1560. DOI: https://doi.org/10.1038/s41598-022-05514-2.
(81) Forsström, J.; Torgnysdotter, A.; Wågberg, L. Influence of fibre/fibre joint strength and fibre flexibility on the strength of papers from unbleached kraft fibres. *Nordic Pulp & Paper Research Journal* **2005**, *20* (2), 186-191.
(82) Koljonen, K. Effect of Surface Properties of Fibres on Some Paper Properties of Mechanical and Chemical Pulp. Doctoral thesis, Helsinki University of Technology, Espoo, Finland, 2004.
(83) Fardim, P.; Durán, N. Modification of fibre surfaces during pulping and refining as analysed by SEM, XPS and ToF-SIMS. *Colloids and Surfaces A: Physicochemical and Engineering Aspects* **2003**, *223* (1), 263-276. DOI: https://doi.org/10.1016/S0927-7757(03)00149-3.
(84) Fardim, P.; Holmbom, B. ToF-SIMS imaging: a valuable chemical microscopy technique for paper and paper coatings. *Applied Surface Science* **2005**, *249* (1), 393-407. DOI: https://doi.org/10.1016/j.apsusc.2004.12.041.
(85) Goacher, R. E.; Jeremic, D.; Master, E. R. Expanding the Library of Secondary Ions That Distinguish Lignin and Polysaccharides in Time-of-Flight Secondary Ion Mass Spectrometry Analysis of Wood. *Analytical Chemistry* **2011**, *83* (3), 804-812. DOI: https://doi.org/10.1021/ac1023028.
(86) Vickerman, J. C.; Briggs, D. *ToF-SIMS: Materials Analysis by Mass Spectrometry*; IM Publications, 2013.
(87) Tolbert, A.; Ragauskas, A. J. Advances in understanding the surface chemistry of lignocellulosic biomass via time-of-flight secondary ion mass spectrometry. *Energy Science & Engineering* **2016**, *5* (1), 5-20. DOI: https://doi.org/10.1002/ese3.144.
(88) Tokareva, E. N.; Pranovich, A. V.; Holmbom, B. R. Characteristic fragment ions from lignin and polysaccharides in ToF–SIMS. *Wood Science and Technology* **2011**, *45* (4), 767-785. DOI: https://doi.org/10.1007/s00226-010-0392-9.
(89) Mou, H. Y.; Wu, S.; Fardim, P. Applications of ToF-SIMS in surface chemistry analysis of lignocellulosic biomass: A review. *BioResources* **2016**, *11*, 5581-5599. DOI: https://doi.org/10.15376/biores.11.2.Mou.
(90) Fardim, P.; Gustafsson, J.; von Schoultz, S.; Peltonen, J.; Holmbom, B. Extractives on fiber surfaces investigated by XPS, ToF-SIMS and AFM. *Colloids and Surfaces A: Physicochemical and Engineering Aspects* **2005**, *255* (1), 91-103. DOI: https://doi.org/10.1016/j.colsurfa.2004.12.027.
(91) Watts, J.; Goacher, R. A guide for the meaningful surface analysis of wood by XPS and ToF-SIMS. *Surface and Interface Analysis* **2021**, *54* (4), 389-404. DOI: https://doi.org/10.1002/sia.7057.
(92) Goacher, R. E.; Tsai, A. Y.-L.; Master, E. R. Towards practical time-of-flight secondary ion mass spectrometry lignocellulolytic enzyme assays. *Biotechnology for Biofuels* **2013**, *6* (1), 132. DOI: https://doi.org/10.1186/1754-6834-6-132.
(93) Goacher, R. E.; Michienzi, C. L. How does soaking wood in various pH buffers impact ToF-SIMS spectra? *Surface and Interface Analysis* **2018**, *50* (2), 163-170. DOI: https://doi.org/10.1002/sia.6354.

(94) Lee, J. L. S.; Gilmore, I. S.; Seah, M. P. Quantification and methodology issues in multivariate analysis of ToF-SIMS data for mixed organic systems. *Surface and Interface Analysis* **2008**, *40* (1), 1-14. DOI: https://doi.org/10.1002/sia.2713.
(95) Graham, D. J.; Gamble, L. J. Back to the basics of time-of-flight secondary ion mass spectrometry of bio-related samples. I. Instrumentation and data collection. *Biointerphases* **2023**, *18* (2), 021201. DOI: https://doi.org/10.1116/6.0002477.
(96) Nuopponen, M.; Vuorinen, T.; Jämsä, S.; Viitaniemi, P. The effects of a heat treatment on the behaviour of extractives in softwood studied by FTIR spectroscopic methods. *Wood Science and Technology* **2003**, *37* (2), 109-115. DOI: https://doi.org/10.1007/s00226-003-0178-4.
(97) Mattsson, A.; Joelsson, T.; Miettinen, A.; Ketoja, J. A.; Pettersson, G.; Engstrand, P. Lignin Inter-Diffusion Underlying Improved Mechanical Performance of Hot-Pressed Paper Webs. *Polymers* **2021**, *13* (15), 2485. DOI: https://doi.org/10.3390/polym13152485.
(98) Joelsson, T. The influence of Pulp Type and Hot-pressing Conditions on Paper Strength Development. Doctoral thesis, Mid Sweden University, Sundsvall, Sweden, 2021.
(99) Pettersson, G.; Norgren, S.; Höglund, H. Strong paper from spruce CTMP - Part I. *Nordic Pulp & Paper Research Journal* **2017**, *32* (1), 54-58. DOI: https://doi.org/10.3183/npprj-2017-32-01-p054-058.
(100) Vernhes, P.; Bloch, J.-F.; Blayo, A.; Pineaux, B. Effect of calendering on paper surface micro-structure: A multi-scale analysis. *Journal of Materials Processing Technology* **2009**, *209*, 5204-5210. DOI: https://doi.org/10.1016/j.jmatprotec.2009.03.005.
(101) Nussbaum, R.; Sterley, M. The effect of wood extractive content on glue adhesion and surface wettability of wood. *Wood and Fiber Science* **2002**, *34*, 57-71.
(102) Guinier, A.; Fournet, G.; Walker, C. B.; Yudowitch, K. L. *Small-angle Scattering of X-rays*; Wiley: New York, 1955.
(103) Gommes, C. J.; Jaksch, S.; Frielinghaus, H. Small-angle scattering for beginners. *Journal of Applied Crystallography* **2021**, *54* (6), 1832-1843. DOI: https://doi.org/10.1107/s1600576721010293.
(104) Scherrer, P. Bestimmung der Größe und der inneren Struktur von Kolloidteilchen mittels Röntgenstrahlen. *Nachrichten von der Gesellschaft der Wissenschaften zu Göttingen, Mathematisch-Physikalische Klasse* **1918**, 98-100.
(105) Patterson, A. L. The Scherrer Formula for X-Ray Particle Size Determination. *Physical Review* **1939**, *56* (10), 978-982. DOI: https://doi.org/10.1103/PhysRev.56.978.
(106) Wiley, W. C.; McLaren, I. H. Time-of-Flight Mass Spectrometer with Improved Resolution. *Review of Scientific Instruments* **1955**, *26* (12), 1150-1157. DOI: https://doi.org/10.1063/1.1715212.
(107) Cotter, R. J. Time-of-Flight Mass Spectrometry. In *Time-of-Flight Mass Spectrometry*, ACS Symposium Series, Vol. 549; American Chemical Society, 1993; pp 16-48.
(108) Oinonen, P. A biomimicking approach for hemicellulose processing. Doctoral thesis, KTH Royal Institute of Technology, Stockholm, Sweden, 2014.
(109) Henrik-Klemens, Å.; Caputo, F.; Ghaffari, R.; Westman, G.; Edlund, U.; Olsson, L.; Larsson, A. The glass transition temperature of isolated native, residual, and technical lignin. *Holzforschung* **2024**, *78* (4), 216-230. DOI: https://doi.org/10.1515/hf-2023-0111.
(110) Jääskeläinen, A. S.; Sun, Y.; Argyropoulos, D. S.; Tamminen, T.; Hortling, B. The effect of isolation method on the chemical structure of residual lignin. *Wood Science and Technology* **2003**, *37* (2), 91-102. DOI: https://doi.org/10.1007/s00226-003-0163-y.
(111) Guerra, A.; Gaspar, A. R.; Contreras, S.; Lucia, L. A.; Crestini, C.; Argyropoulos, D. S. On the propensity of lignin to associate: A size exclusion chromatography study with lignin derivatives

isolated from different plant species. *Phytochemistry* **2007**, *68* (20), 2570-2583. DOI: https://doi.org/10.1016/j.phytochem.2007.05.026.
(112) Börås, L.; Gatenholm, P. Surface Composition and Morphology of CTMP Fibers. *Holzforschung* **1999**, *53* (2), 188-194. DOI: https://doi.org/10.1515/HF.1999.031.
(113) Zhao, H.; Heindel, N. D. Determination of Degree of Substitution of Formyl Groups in Polyaldehyde Dextran by the Hydroxylamine Hydrochloride Method. *Pharmaceutical Research* **1991**, *8* (3), 400-402. DOI: https://doi.org/10.1023/A:1015866104055.
(114) Segal, L.; Creely, J. J.; Martin, A. E.; Conrad, C. M. An Empirical Method for Estimating the Degree of Crystallinity of Native Cellulose Using the X-Ray Diffractometer. *Textile Research Journal* **1959**, *29*, 786-794. DOI: https://doi.org/10.1177/004051755902901003.
(115) Balzar, D.; Ledbetter, H. Voigt-function modeling in Fourier analysis of size- and strain-broadened X-ray diffraction peaks. *Journal of Applied Crystallography* **1993**, *26* (1), 97-103. DOI: https://doi.org/10.1107/S0021889892008987.
(116) Penttilä, P. A.; Várnai, A.; Fernández, M.; Kontro, I.; Liljeström, V.; Lindner, P.; Siika-aho, M.; Viikari, L.; Serimaa, R. Small-angle scattering study of structural changes in the microfibril network of nanocellulose during enzymatic hydrolysis. *Cellulose* **2013**, *20* (3), 1031-1040. DOI: https://doi.org/10.1007/s10570-013-9899-1.
(117) Lo Re, G.; Engel, E. R.; Björn, L.; Sicairos, M. G.; Liebi, M.; Wahlberg, J.; Jonasson, K.; Larsson, P. A. Melt processable cellulose fibres engineered for replacing oil-based thermoplastics. *Chemical Engineering Journal* **2023**, *458*, 141372. DOI: https://doi.org/10.1016/j.cej.2023.141372.
(118) Zhang, S. Swelling and dissolution of cellulose in NaOH aqueous solvent systems. *Cellulose Chemistry and Technology* **2013**, *47* (9-10), 671-679.
(119) Sjöstedt, A.; Wohlert, J.; Larsson, P. T.; Wågberg, L. Structural changes during swelling of highly charged cellulose fibres. *Cellulose* **2015**, *22* (5), 2943-2953. DOI: https://doi.org/10.1007/s10570-015-0701-4.
(120) Viet, D.; Beck-Candanedo, S.; Gray, D. G. Dispersion of cellulose nanocrystals in polar organic solvents. *Cellulose* **2007**, *14* (2), 109-113. DOI: https://doi.org/10.1007/s10570-006-9093-9.
(121) Kádár, R.; Spirk, S.; Nypelö, T. Cellulose Nanocrystal Liquid Crystal Phases: Progress and Challenges in Characterization Using Rheology Coupled to Optics, Scattering, and Spectroscopy. *ACS Nano* **2021**, *15* (5), 7931-7945. DOI: https://doi.org/10.1021/acsnano.0c09829.
(122) Richely, E.; Zarei, A.; Melelli, A.; Rajan, D. K.; Govilas, J.; Gabrion, X.; Clévy, C.; Legland, D.; Perez, J.; Guessasma, S.; et al. Measurement of microfibril angle in plant fibres: Comparison between X-ray diffraction, second harmonic generation and transmission ellipsometry microscopies. *Composites Part C: Open Access* **2023**, *11*, 100355. DOI: https://doi.org/10.1016/j.jcomc.2023.100355.
(123) Gorišek, Ž.; Torelli, N. Microfibril Angle in Juvenile, Adult and Compression Wood of Spruce and Silver Fir. *Phyton* **1999**, *39* (3), 129-132.
(124) Naserifar, S.; Swensson, B.; Bernin, D.; Hasani, M. Aqueous N,N-dimethylmorpholinium hydroxide as a novel solvent for cellulose. *European Polymer Journal* **2021**, *161*, 110822. DOI: https://doi.org/10.1016/j.eurpolymj.2021.110822.
(125) Sjöstrand, B.; Barbier, C.; Ullsten, H.; Nilsson, L. Dewatering of Softwood Kraft Pulp with Additives of Microfibrillated Cellulose and Dialcohol Cellulose. *BioResources* **2019**, *14* (3), 6370-6383. DOI: https://doi.org/10.15376/biores.14.3.6370-6383.
(126) Forsström, J.; Andreasson, B.; Wågberg, L. Influence of pore structure and water retaining ability of fibres on the strength of papers from unbleached kraft fibres. *Nordic Pulp & Paper Research Journal* **2005**, *20* (2), 176-185. DOI: https://doi.org/10.3183/npprj-2005-20-02-p176-185.

(127) Brännvall, E.; Larsson, P. T.; Stevanic, J. S. Changes in the cellulose fiber wall supramolecular structure during the initial stages of chemical treatments of wood evaluated by NMR and X-ray scattering. *Cellulose* **2021**, *28* (7), 3951-3965. DOI: https://doi.org/10.1007/s10570-021-03790-1.
(128) Saito, K.; Kato, T.; Tsuji, Y.; Fukushima, K. Identifying the Characteristic Secondary Ions of Lignin Polymer Using ToF−SIMS. *Biomacromolecules* **2005**, *6* (2), 678-683. DOI: https://doi.org/10.1021/bm049521v.
(129) Saito, K.; Kato, T.; Takamori, H.; Kishimoto, T.; Yamamoto, A.; Fukushima, K. A new analysis of the depolymerized fragments of lignin polymer in the plant cell walls using ToF-SIMS. *Applied Surface Science* **2006**, *252* (19), 6734-6737. DOI: https://doi.org/10.1016/j.apsusc.2006.02.163.
(130) Kleen, M. Surface lignin and extractives on hardwood RDH kraft pulp chemically characterized by ToF-SIMS. *Holzforschung* **2005**, *59* (5), 481-487. DOI: https://doi.org/10.1515/HF.2005.080.
(131) Braham, E. J.; Goacher, R. E. Identifying and minimizing buffer interferences in ToF-SIMS analyses of lignocellulose. *Surface and Interface Analysis* **2015**, *47* (1), 120-126. DOI: https://doi.org/10.1002/sia.5683.
(132) Zhou, C.; Li, Q.; Chiang, V. L.; Lucia, L. A.; Griffis, D. P. Chemical and Spatial Differentiation of Syringyl and Guaiacyl Lignins in Poplar Wood via Time-of-Flight Secondary Ion Mass Spectrometry. *Analytical Chemistry* **2011**, *83* (18), 7020-7026. DOI: https://doi.org/10.1021/ac200903y.
(133) Morreel, K.; Kim, H.; Lu, F.; Dima, O.; Akiyama, T.; Vanholme, R.; Niculaes, C.; Goeminne, G.; Inzé, D.; Messens, E.; et al. Mass Spectrometry-Based Fragmentation as an Identification Tool in Lignomics. *Analytical Chemistry* **2010**, *82* (19), 8095-8105. DOI: https://doi.org/10.1021/ac100968g.
(134) Lucia, L. A.; Mancosky, D. G. Use of TOF-SIMS for the analysis of surface metals in H2O2-bleached lignocellulosic fibers. *Pure and Applied Chemistry* **2001**, *73* (12), 2047-2058. DOI: https://doi.org/10.1351/pac200173122047.
(135) Bertrand, P.; Lu-Tao, W. Time-of-Flight Secondary Ion Mass Spectrometry (ToF-SIMS). In *Microbeam and Nanobeam Analysis*, 1996; Benoit, D., Bresse, J.-F., Van't dack, L., Werner, H., Wernisch, J., Eds.; Springer: Vienna, pp 167-182.
(136) Morreel, K.; Dima, O.; Kim, H.; Lu, F.; Niculaes, C.; Vanholme, R.; Dauwe, R.; Goeminne, G.; Inzé, D.; Messens, E.; et al. Mass Spectrometry-Based Sequencing of Lignin Oligomers. *Plant Physiology* **2010**, *153* (4), 1464-1478. DOI: https://doi.org/10.1104/pp.110.156489.
(137) Elf, P.; Mattsson, A.; Paajanen, A.; Ketoja, J. A.; Pettersson, G.; Sanchez-Salvador, J. L.; Blanco, A.; Negro, C.; Engstrand, P.; Hedenqvist, M. S.; et al. Role of Lignin in Hot-Pressing of Paper: Insights from Molecular Simulations and Experiments. *Biomacromolecules* **2025**, *26* (9), 5965-5978. DOI: https://doi.org/10.1021/acs.biomac.5c00872.
(138) Goring, D. A. I. Thermal softening of lignin, hemicellulose and cellulose. *Pulp and Paper Magazine of Canada* **1963**, *64* (12).
(139) Back, E.; Salmén, L. Glass transitions of wood components hold implications for molding and pulping processes. *Tappi Journal* **1982**, *65*, 107-110.
(140) Wheelock, Å. M.; Wheelock, C. E. Trials and tribulations of 'omics data analysis: assessing quality of SIMCA-based multivariate models using examples from pulmonary medicine. *Molecular BioSystems* **2013**, *9* (11), 2589-2596. DOI: https://doi.org/10.1039/C3MB70194H.
(141) Trygg, J.; Wold, S. Orthogonal projections to latent structures (O-PLS). *Journal of Chemometrics* **2002**, *16* (3), 119-128. DOI: https://doi.org/10.1002/cem.695.
(142) Kirwan, G. M.; Johansson, E.; Kleemann, R.; Verheij, E. R.; Wheelock, Å. M.; Goto, S.; Trygg, J.; Wheelock, C. E. Building multivariate systems biology models. *Analytical Chemistry* **2012**, *84* (16), 7064-7071. DOI: https://doi.org/10.1021/ac301269r.

(143) Jusner, P.; Barbini, S.; Schiehser, S.; Bacher, M.; Schwaiger, E.; Potthast, A.; Rosenau, T. Impact of residual extractives on the thermal stability of softwood Kraft pulp. *Cellulose* **2022**, *29* (16), 8797-8810. DOI: https://doi.org/10.1007/s10570-022-04807-z.
(144) Freire, C.; Pinto, P.; Santiago, A.; Silvestre, A.; Evtuguin, D.; Neto, C. Comparative study of lipophilic extractives of hardwoods and corresponding ECF bleached kraft pulps. *BioResources* **2006**, *1*, 3-17. DOI: https://doi.org/10.15376/biores.1.1.3-17.
(145) Jansson, M.; Wadsborn, R. Calculation of the influence of carbonate concentration on the formation of fatty acid calcium soaps in pulp washing. *Nordic Pulp & Paper Research Journal* **2007**, *22*, 35-41.
(146) Björklund Jansson, M.; Back, E. L.; Tufvesson, M. I. A Review of Kraft Pulp Deresination and Pitch Problems. In *Papermaking Raw Materials: Transactions of the 8th Fundamental Research Symposium*, Oxford, UK, 1985; Mechanical Engineering Publications: London, 1985; Vol. 2, p 729. DOI: https://doi.org/10.15376/frc.1985.2.729.
(147) Ghonjizade-Samani, F.; Haurie, L.; Malet, R.; Realinho, V. The Components' Roles in Thermal Stability and Flammability of Cork Powder. *Materials* **2023**, *16* (10), 3829. DOI: https://doi.org/10.3390/ma16103829.